Copyright

by

Palash Vadiraj Acharya

2021

The Dissertation Committee for Palash Vadiraj Acharya Certifies that this is the approved version of the following Dissertation:

Investigating thermodynamics and kinetics of hydrate phase change phenomena using experimental and machine learning tools

Committee:

Vaibhav Bahadur, Supervisor

Ofodike Ezekoye

Li Shi

Roger Bonnecaze

Investigating thermodynamics and kinetics of hydrate phase change phenomena using experimental and machine learning tools

by

Palash Vadiraj Acharya

Dissertation

Presented to the Faculty of the Graduate School of

The University of Texas at Austin

in Partial Fulfillment

of the Requirements

for the Degree of

Doctor of Philosophy

The University of Texas at Austin

December 2021

Dedicated to my Sadhguru Shirdi Saibaba

Acknowledgements

Words fail to express my gratitude to Sadhguru Shirdi Saibaba, who has been my unwavering companion and guide through all the highs and lows of my life. I remain in his eternal debt for the infinite grace and love that he has bestowed upon me.

I am grateful to my amma, appa and akka for all their sacrifices and support throughout. Amma has always been the embodiment of courage, determination and motivation and I am infinitely lucky to have her in my life. None of this would have been possible if not for my billudi, who has enriched my life with love and support during my time at UT Austin.

I would like to sincerely thank my advisor, Dr. Vaibhav Bahadur for providing me with the freedom and opportunities to explore and present my ideas. Your scientific intuition, valuable insights, practical & structured approach to problems and communication skills have been traits that I have always tried to look up to and incorporate in my life. Thank you very much for all your time and support.

I would like to thank my dissertation committee Prof. Ofodike Ezekoye, Prof. Li Shi and Prof. Roger Bonnecaze for their time in reviewing my work and for the opportunity to attend some of the most interesting and enjoyable classes at UT Austin. I would specially like to thank Dr. Ezekoye for always welcoming me with a smile whenever I have approached his office door and for all the interesting discussions and guidance. I would like to acknowledge Exxon Mobil for their funding and particularly Ashish Mhadeshwar, Pradeep Venkataraman, Tim Barckholtz for their time, support, input and valuable guidance.

I would like to thank all my past and current lab mates particularly Dr. Arjang Shahriari for guiding me academically as well as professionally during my former and later years of Ph.D. research, Dr. Onur Ozkan for all the insightful discussions, Manojkumar Lokanathan for being a great project partner to work with on numerous problems and Awan Bhati for all the timely help with the CO_2 hydrate-related experiments. I would like to thank the undergraduate students, Denise Lin and Jaime Estrada for their help along the way. I have learned a lot from everyone and thoroughly enjoyed the countless hours spent in the lab brainstorming and discussing ideas while having fun at the same time.

I would like to acknowledge the staff at the Walker Department of Mechanical Engineering at the University of Texas at Austin, Ricardo Palacios, Mark Philips, Israel Gutierrez, Terrie Chandler, Lori Holloway, Ashlee Vrana, Diana Ziegler and Micah Jackman for their technical and administrative support.

Abstract

Investigating thermodynamics and kinetics of hydrate phase change phenomena using experimental and machine learning tools

Palash Vadiraj Acharya, Ph.D.

The University of Texas at Austin, 2021

Supervisor: Vaibhav Bahadur

Hydrates are ice-like crystalline solids which form under high pressure and low temperature conditions from water (forming a cage of host molecules) and another liquid or gas (guest molecule). Hydrates can enable numerous industrial applications in the fields of carbon capture and sequestration (CCS), flow assurance, natural gas transportation/storage and desalination. A significant technological barrier to many hydrates-related applications is the slow rate of formation of hydrates, which is a result of thermodynamic and kinetics-related limitations.

This dissertation investigates the role of electric field and surface chemistry in accelerating the nucleation kinetics of clathrate hydrates (CO_2, tetrahydrofuran). It also investigates the role of amino acids in inhibiting the nucleation kinetics and thermodynamics of CO_2 hydrate formation. It also evaluates the utility of machine learning models in predicting the thermodynamic formation conditions for gas hydrates. In addition to the focus on fundamental investigations, this dissertation also evaluates the utility of hydrates as a carbon capture tool when coupled with a steam reforming system

to generate blue hydrogen from landfill gas. The content of the dissertation work is motivated by three objectives, as described ahead.

Objective 1 investigates the influence of electric fields and surface chemistry on nucleation kinetics of hydrate formation for two kinds of hydrate forming systems (considered as two separate subtasks): miscible liquid-liquid systems (Tetrahydrofuran-water) and gas-liquid (CO_2-water) systems. As background, it is noted that the role of electric field has been widely studied for accelerating freezing of water. Subtask 1-1 investigates the role of electric field when used in conjunction with open-cell aluminum metal foam-based electrodes in accelerating the formation of THF hydrates. It is demonstrated that aluminum foam electrodes trigger near-instantaneous nucleation (in only tens of seconds) of THF hydrates at very low voltages (~20V). The promotion effect can be ascribed to two distinct interfacial mechanisms at play: namely, electrolytic bubble generation and the formation of metal ion complex-based coordination compounds.

While THF hydrates form under atmospheric pressure, CO_2 gas hydrates form at much higher pressures and are therefore studied using a custom-built high-pressure cell. Subtask 1-2 highlights the role of aluminum in accelerating nucleation kinetics of CO_2 gas hydrates. Statistically meaningful measurements of induction times for CO_2 hydrate nucleation are undertaken using water droplets as individual microsystems for hydrate formation. The influence of various metal surfaces, droplet size, CO_2 dissolution time, and the presence of salts in water on nucleation kinetics have been characterized. It is observed that Al metal significantly accelerates the nucleation kinetics of CO_2 hydrates (the effect of which cannot be replicated by salts of Al) with nucleation initiating from the Al-water interface.

Prediction of thermodynamic conditions of hydrate formation is critical to their synthesis and Objective 2 is centered around developing modeling and experimental tools for effective prediction of thermodynamic phase equilibria for hydrates. Subtask 2-1 demonstrates the utility of machine learning models to predict hydrate dissociation temperature (HDT) as a function of constituent hydrate precursors and salt inhibitors. Importantly, and in contrast to most previous studies, thermodynamic variables such as the activity-based contribution due to electrolytes, partial pressure of individual gases, and specific gravity of the overall mixture have been used as input features in the prediction algorithms. Using such features results in more physics-aware ML algorithms, which can capture the individual contributions of gases and electrolytes in a more fundamental manner. Three ML algorithms: Random Forest (RF), Extra Trees (ET), and Extreme Gradient Boosting (XGBoost) are trained and their performance is evaluated on an extensive experimental dataset comprising of more than 1800 experimental data points. The overall coefficient of determination (R^2) is greater than 97% for all the three ML models with XGBoost exhibiting the best prediction performance with an R^2 metric of 99.56%.

Subtask 2-2 investigates the role of amino acids on the kinetics and thermodynamics of CO_2 hydrate formation using droplet-based microsystems. Amino acids are environmentally friendly and inexpensive hydrate formation inhibitors. Nucleation kinetics as well as the depression in thermodynamic hydrate formation temperature for CO_2 hydrates in the presence of five amino acids containing non-polar side chains have been evaluated. All the amino acids inhibit nucleation with tryptophan exhibiting the slowest nucleation rate. Isoleucine exhibits the highest thermodynamic inhibition effect with the highest depression in freezing point temperature corresponding to 0.2 K for the concentrations studied in the present analysis.

Landfills produce significant amounts of methane, which is a potent greenhouse gas. Steam reforming of the landfill gas generates CO_2 + H_2 as byproducts. The generated hydrogen can be used in refineries, to produce fertilizers or to produce electricity in a fuel cell. Objective 3 investigates the techno-economic factors associated with a facility coupling a sorption enhanced steam methane reforming system with a hydrates-based capture system for landfills across Texas. The electrical energy requirements, water use, operating and capital costs required to set up and keep such a facility running have been evaluated in detail. The cost of producing hydrogen for all counties is about \$0.5/kg of H_2 (excluding the cost for natural gas). The total carbon capture cost lies in the range of \$96-\$145/metric ton of CO_2 with the lowest/highest cost corresponding to Harris/Brazoria county producing the highest/lowest amount of CO_2. A minimum cost of \$0.9(2.4)/kg of H_2 would be required for Harris (Brazoria) county for a positive 30-year net present value; a 5-year payback period would require a minimum cost of \$1.35(4.95)/kg of H_2.

In summary, this dissertation significantly advances the current understanding of hydrate formation by introducing novel techniques (consuming ultra-low energy as well as passive tools) for enhancing hydrate formation kinetics. It also develops novel ML and experimental tools for predicting thermodynamic formation conditions of hydrates in the presence of various inhibitors. Finally, this work assesses the technical and economic viability of a hydrates-centered future for the natural gas industry.

Table of Contents

List of Tables xv

List of Figures xvi

Chapter 1: Introduction and literature review 1

1.1 Literature Review 7

1.1.1 Past studies on electric field-assisted freezing of water and hydrates 7

1.1.2 Past studies on methods to accelerate nucleation of hydrates 20

1.1.3 Past studies on thermodynamic inhibition of gas hydrate formation using amino acids 26

1.1.4 Past studies on methods to predict thermodynamic conditions for hydrate formation 28

1.2 Objectives of research for this dissertation 31

1.3 Organization of the rest of dissertation 35

Chapter 2: Electronucleation of Tetrahydrofuran hydrates using metal foam-based electrodes 36

2.1 Experimental Procedure 37

2.2 Results 40

2.3 Discussions 46

2.4 Conclusions 48

Chapter 3: Aluminum-based promotion of nucleation of carbon dioxide hydrates 49

3.1 Experimental procedure 49

3.2 Results and discussions 55

3.3 Conclusions 64

Chapter 4: Studying the thermodynamics and kinetics of CO_2 hydrate nucleation in the presence of amino acids 65

4.1 Description of experiments 65

4.1.1 Materials 65

4.1.2 Experimental apparatus and procedure 67

4.1.3 Average depression in freezing point temperature 70

4.1.4 Calculation of nucleation rate 71

4.2. Results and Discussions 71

4.2.1 Kinetic measurements 71

4.3.2 Thermodynamic measurements 75

5.4 Conclusions 79

Chapter 5: Thermodynamic features-driven machine learning-based prediction of clathrate hydrate equilibria 81

5.1 Methodology of the present study 81

5.2 Description of machine learning models 83

5.2.1 Random Forest and Extra Trees 84

5.2.2 XGBoost (Extreme gradient boosting) 85

5.3 Development of Machine Learning models 87

5.3.1 Experimental database 87

5.3.2 Calculations of activity and partial pressure 89

5.3.3 Procedure for conducting ML analysis 91

5.4 Results and discussions 92

5.4.1 Validity of the model 92

5.5 Conclusions 107

Chapter 6: Techno-economic analysis of hydrates-based carbon capture system for landfill gases in Texas 108

6.1 Technical Analysis 109

6.1.1 LFG data 109

6.1.2 Sorption enhanced steam methane reforming 110

6.1.3 Hydrates-based carbon capture 112

6.1.4 Energetics of hydrate formation process: Compression 113

6.1.5 Energetics of hydrate formation process: Refrigeration 115

6.2 Economic Analysis 116

6.2 Results and Discussions 119

6.3 Conclusions 131

Chapter 7: Conclusions and suggestions for future work 133

7.1 Major scientific findings and contributions of this dissertation 133

7.1.1 Role of electric field and aluminum foams in accelerating nucleation of THF hydrates 133

7.1.2 Role of aluminum in accelerating nucleation of CO_2 hydrates 134

7.1.3 Investigating inhibition effect of amino acids on CO_2 hydrate formation 135

7.1.4 Investigating the predictive utility of machine learning algorithms when combined with thermodynamic features to predict phase equilibrium conditions for hydrate formation 136

7.1.5 Studying the techno-economics associated with industrial sized hydrates-based carbon capture facility 137

7.2 Recommendations for future work 138

7.2.1 Role of electric field and acoustics for nucleation of cyclopentane hydrates 138

7.2.2 Bubble-based promotion of CO_2 hydrate formation 140

7.2.3 Machine learning + QSPR 141

7.2.4 Aluminum or active metal-based promotion of CH_4, H_2, and tetraalkylammonium salt hydrates 143

7.2.5 Droplet-based measurement of thermodynamic phase equilibria of hydrates in the presence of an electric field.....143

Appendices.....144

Appendix A: Supporting information for Al-based promotion of CO_2 hydrates ...144

Appendix B: Fundamental Interfacial mechanisms underlying electrofreezing 149

Appendix C: Magnesium-promoted rapid Nucleation of Carbon Dioxide Hydrates 150

Appendix D: Machine learning-based predictions of benefits of high thermal conductivity encapsulation materials for power electronics packaging 152

Appendix E: Green hydrogen-based energy storage in Texas for decarbonization of the electric grid 154

Appendix F: Modeling the influence of Marangoni flows on the Leidenfrost state on solid and liquid substrates 156

Appendix G: Review of nanocomposite dielectric materials with high thermal conductivity 157

Appendix H: Assessing the performance of advanced cooling techniques on thermal management of next-generation power electronics.....159

Appendix I: Estimation of fuel quality using statistical regression -based analysis of Leidenfrost droplets.....160

References.....161

List of Tables

Table 1.1 Summary of induction times reported in previous studies using various promotion techniques. 22

Table 2.1 Time taken for hydrates to form in the entire tube (minutes). 48

Table 3.1 Summary of induction time data for various experiments. 56

Table 4.1 Physical properties of the amino acids considered in the present study. [a]Numerical values were taken from Ref. [157]. 66

Table 4.2 Summary of induction time and nucleation rate data for 20μL water droplets containing various amino acids at 0.1 mol% concentration. 73

Table 5.1. Summary of the experimental database used in the present study. 89

Table 5.2 Accuracy of predictions obtained by ML algorithms employed in the present study. 94

Table 5.3 Comparison between predictions (3 ML models) and experimental data [47] for hydrate formation under varying salt concentrations. 102

Table 5.4 Comparison between predictions (3 ML models) and experimental data [186] for hydrate formation from binary and ternary gas mixtures 105

Table 6.1 Details of landfills and the amount of gas collected across different counties in Texas. Data obtained from EPA website [217]. 110

Table 6.2 Itemized cost estimation for annual capital and operating cost (in million $) for 10 counties in Texas. 126

Table A.1 Induction time data for 40 μL droplets obtained in a single run 145

Table A.2 Induction time data for 20 μL droplets obtained in a single run 145

List of Figures

Figure 1.1 Structure and type of gas hydrates [8]. Depending on the type of hydrocarbon molecule, different cage structures exist where the unit cell for sI and sII has two types of cage structures, and sH has three types of cage structures. The number and corresponding superscripts for a cage structure indicate the number of edges in each face and the number of corresponding faces in the cage lattice. 3

Figure 1.2. Fraction of water droplets (radius: 1 mm) frozen under different conditions and temperatures. Electric fields enable more effective freezing as compared to mechanical disturbances. This plot is based on data reported in Reference [21] and published in [9]. The applied electric field ranged from 0-15 x 10^5 V/m. 10

Figure 1.3. Electrolytic bubble formation at cathode [42] (a) A sharp cathode produces a larger hydrogen bubble, which interferes with coordination compound formation at the anode (b) A flat cathode, on the other hand, produces a large number of smaller bubbles which do not affect reactions occurring at the anode. This explains the observed higher electrofreezing tendency with flat cathodes as compared to a sharp cathode. Figures 1.3 reprinted with permission from Reference [42]. Copyright: 2005 by Elsevier. 15

Figure 1.4. (a) Schematic of experimental setup to observe confinement-induced freezing under an electric field [43]. Water is present in the gap between the gold tip and the negatively biased gold (111) surface. A piezo driver of known sensitivity controls gap spacing. The black and white spheres represent hydrogen and oxygen molecules in a bilayer of water molecules, respectively. (b) Schematic of experimental setup to study the role of an electric field on homogeneous nucleation of water droplets [47]. Droplets travel through a microfluidic channel cooled to -40 ^{o}C under a transverse electric field. Figure 1.3(a) reprinted with permission from Reference [43]. Copyright: 2005 American Physical Society. Figure 1.4(b) reprinted with permission from Reference [47]. Copyright: 2011 American Chemical Society. 17

Figure 1.5. Electrowetting-based experimental setups used for studies on electrofreezing (a) Top view of nucleation and phase front propagation inside a droplet [51]. Electrofreezing commences at the three-phase line, with multiple nucleation points at higher voltages. (b) Experiments to isolate the influence of electric field and current flow on electrofreezing [52]. Results indicate that both phenomena influence electrofreezing. Figure 1.5(a) reprinted with permission from Reference [51]. Copyright: 2015 AIP Publishing LLC. Figure 1.5(b) reprinted with permission from Reference [52]. Copyright: 2015 American Chemical Society 19

Figure 1.6 Formation of bubbles on cathode during electronucleation experiments at different voltages. Such bubbles act as nucleating sites with the convection currents and pressure variation with bubble growth, further promoting hydrate formation. Figure 1.6 reprinted with permission from Reference [54]. Copyright: 2016 American Chemical Society; further permission related to the material excerpted should be directed to the ACS.....20

Figure 2.1 (a) Experimental setup, (b) Stainless steel and aluminum foam electrodes inside the tube (right image shows the foam electrode), and c) detection of nucleation by tracking the thermal signature and current flow in the hydrate precursor solution.....38

Figure 2.2 Voltage-dependent electronucleation induction times for the baseline (non-foam, inert electrode) case and the cases where the aluminum foam was the cathode and anode. The numbers next to the data points indicate the average and standard deviation (in parenthesis) in the measurements. 41

Figure 2.3 Schematic depiction of mechanisms underlying electronucleation (a) Bubble-related effects when aluminum foam is the cathode (b) Coordination compound formation-based nucleation when aluminum foam is the anode. 43

Figure 2.4 Aluminum foams acting as the (a) cathode, which leads to significant bubble generation, and (b) anode, where no bubble generation is observed. 44

Figure 2.5 Bubble generation (a) is seen with the foam electrode as the cathode. However, aluminum ions in solution are detected via a color change (b) due to chelation, which indicates that aluminum-based coordination compounds are formed when the foam electrode is the anode. 46
Figure 3.1 Schematic illustration of the experimental setup (top) Images of the pressure vessel housed in an environmental chamber (bottom). Figure reprinted with permission from [148]. Copyright 2020 American Chemical Society. 51
Figure 3.2 Surface roughness profiles for (a) aluminum, (b) copper and (c) stainless steel plates. Figure reprinted with permission from [148]. Copyright 2020 American Chemical Society. 53
Figure 3.3 Water droplet (left) with a CO_2 dissolution time of 90 mins turn opaque (right) upon conversion to CO_2 hydrate. Figure reprinted with permission from [148]. Copyright 2020 American Chemical Society. 55
Figure 3.4 Cumulative probability distribution for three different droplet volumes (10, 20 and 40 μL). Figure reprinted with permission from [148]. Copyright 2020 American Chemical Society. 57
Figure 3.5. Histogram showing fraction of droplets nucleating in various time intervals (grouped using 100-minute bins) for three different droplet volumes (10, 20 and 40 μL) (dissolution time: 90 minutes). Figure reprinted with permission from [148]. Copyright 2020 American Chemical Society. 58
Figure 3.6. CO_2 hydrates (with whiskers) formed from water droplets with a long CO_2 dissolution time (24 hours). Figure reprinted with permission from [148]. Copyright 2020 American Chemical Society.....60

Figure 3.7. Snapshots depicting CO_2 hydrate nucleation at the Al-water interface (left to right). Nucleation originates at the spot, marked in a yellow circle, and proceeds towards the 3-phase line. Figure reprinted with permission from [148]. Copyright 2020 American Chemical Society. 61
Figure 4.1 Schematic illustration of the experimental setup. Figure reprinted with permission from [148]. Copyright 2020 American Chemical Society 68
Figure 4.2. Snapshots at succeeding time intervals depicting film growth during a hydrate formation event. 70
Figure 4.3. Water droplets containing isoleucine, before (left) and after (right) CO_2 hydrate formation. 72
Figure 4.4. Cumulative probability distribution for CO_2 hydrate formation in the presence of amino acids. The graphs represent the curves fitted to the probability values obtained from the experimental induction time data points using Equation 4.2. 75
Figure 4.5 Comparison between experimental phase equilibria points obtained in the present work vs. CSMGem for pure CO_2 hydrates. The literature values were obtained from the work of Fan and Guo [166] and Dholabhai et al. [167] 76
Figure 4.6. Snapshots showing the progression of dissociation events for pure water droplets and droplets containing isoleucine and leucine. Water droplet dissociates at the end, demonstrating the thermodynamic inhibition effect of the amino acids on CO_2 hydrates. 77
Figure 4.7. Experimentally measured HL_wV phase equilibrium data points for CO_2 hydrates in the presence of varying concentrations of amino acids. 78

Figure 4.8 Average depression in freeing point temperature for the amino acids considered in the present study. Molar concentrations are denoted in mol% in brackets.....79
Figure 5.1. An illustrative decision tree associated with hydrate dissociation temperature predictions.....84
Figure 5.2. Comparison of experimental hydrate dissociation temperatures versus predictions obtained from three ML models, (a) Random Forest, (b) Extra Trees, and (c) XGBoost.....97
Figure 5.3. Distribution of the absolute relative error in predicting hydrate dissociation temperature (logarithmic y-axis) for (a) training and (b) test data sets obtained using XGBoost, Random Forest and Extra Trees algorithms. 99
Figure 5.4. Pressure-Temperature data associated with the formation of methane hydrates in the presence of (a) NaCl and (b) $CaCl_2$ (varying weight percentages). Solid symbols represent the predictions from XGBoost model, while non-solid symbols represent experimental data [185], [189].....101
Figure 6.1 Illustrative concept of LFG-based blue hydrogen generation via SESMR and CO_2 capture via hydrates.....111
Figure 6.2. Three-stage compression process for compressing the gas to hydrate forming conditions (3.2 MPa).....114
Figure 6.3. Total amount of CO_2 and H_2 that can be collected/produced annually (in million metric tons) for the top 10 counties in Texas. 121
Figure 6.4. Amount of water required daily for capturing all the CO_2 collected as hydrates. 122

Figure 6.5. Electrical energy requirements for compression and refrigeration process. .123
Figure 6.6. Capital cost for compressors, reactor vessels and refrigeration system. 124
Figure 6.7. Cost (Capital + Operating) required to capture one metric ton of CO_2 across different counties in Texas. 129
Figure 6.8 Net present value at 30 years and payback period for a combined SESMR + hydrates-based carbon capture system for producing hydrogen using steam reforming of LFG in (a) Harris county and (b) Brazoria county. 130
Figure 7.1 Schematic of cell to study electronucleation at a cyclopentane-water interface.....139
Figure 7.2 Rapid hydrate formation observed in bulk water (left) and test tube (right), induced by bubbling CO_2 through water. 141
Figure A.1. Nucleation order of the droplets for experiments employing 40 (top) and 20 (bottom) μL droplets 144
Figure A.2 Fraction of 20 μL droplets nucleating in different time intervals (droplets contain 3.5 wt% NaCl).....146
Figure A.3 Fraction of 20 μL droplets nucleating in different time intervals (24 hour CO_2 dissolution time).....146
Figure A.4 Droplet morphologies for a CO_2 dissolution time of 90 minutes (top) and 24 hours (bottom) for a droplet volume of 20 μL. 147
Figure A.5 DI water droplets imbued with pyrocatechol violet indicator placed on the Al substrate (top) turned blue (bottom) indicating the presence of Aluminum ions.....148

Chapter 1: Introduction and literature review

The rapid onset of global warming, attributable to the rapidly increasing concentrations of greenhouse gases (GHGs like CO_2, CH_4 and N_2O) is arguably one of the most potent disasters facing humanity today. CO_2, in particular, accounted for more than 80% of all the anthropogenic US greenhouse gas emissions in 2019 [1]. It is imperative to limit the rise in global average temperature to 1.5-2 ^oC above the preindustrial levels, as targeted by the Paris agreement to reduce the risks and impact of climate change resulting from global warming [2]. While constraining fossil fuel emissions and transitioning towards renewables is crucial, active deployment of carbon capture and sequestration (CCS) practices is likely key to achieving the targets set by the Paris agreement. Clathrate hydrates that act as effective storehouses of CO_2 have been explored as one of the potential CCS pathways owing to their desirable long-term sequestration properties. Some of these properties include a high storage capacity (184 unit volumes of gas at STP conditions in one unit volume of hydrates), higher density than seawater (1040 to 1160 kg/m^3), and stability at moderate oceanic and permafrost depths at a temperature below 10 ^oC [3]. Due to these properties, CO_2 hydrates could be potentially stored in deep oceanic basins and permafrost regions, sub-seafloor saline formations and depleted/existing natural gas hydrate reservoirs (via CH_4-CO_2 exchange), provided they meet the thermodynamic criteria (pressure and temperature conditions) required for stable storage [3].

Gas hydrates are naturally occurring crystalline compounds consisting of a lattice of hydrogen-bonded water molecules (host) encapsulating a guest hydrocarbon molecule such as methane, carbon dioxide, hydrogen etc. [4]. The water molecules comprising the cage structure are held together via hydrogen bonds. The guest molecule interacts with

the host water molecules in the cage lattice via Van der Waal forces to keep the cage structure stable and prevent it from collapsing. Depending on the size of the guest molecule, three common hydrate structures exist: structure I (sI, cubic) [5], structure II (sII, cubic) [6] and structure H (sH, hexagonal) [7]. Hydrates can also be classified depending on the characteristics of the precursor solution: three systems commonly exist: miscible liquid-liquid system (THF + water), immiscible liquid-liquid (cyclopentane + water) system, and gas-water (CO_2 + water) system. Miscible/Immiscible liquid-water hydrate systems commonly form at atmospheric pressure and low-temperature conditions and are often used to mimic the behavior of gas hydrate formation under milder laboratory conditions.

It is notable that while hydrate formation is beneficial for applications such as carbon capture and storage, methane hydrates are detrimental to the subsea infrastructure in the oil and gas industry as they lead to pipeline plugging, rupture and blowouts. Operating conditions in these deep-water production facilities are very conducive to hydrate formation.

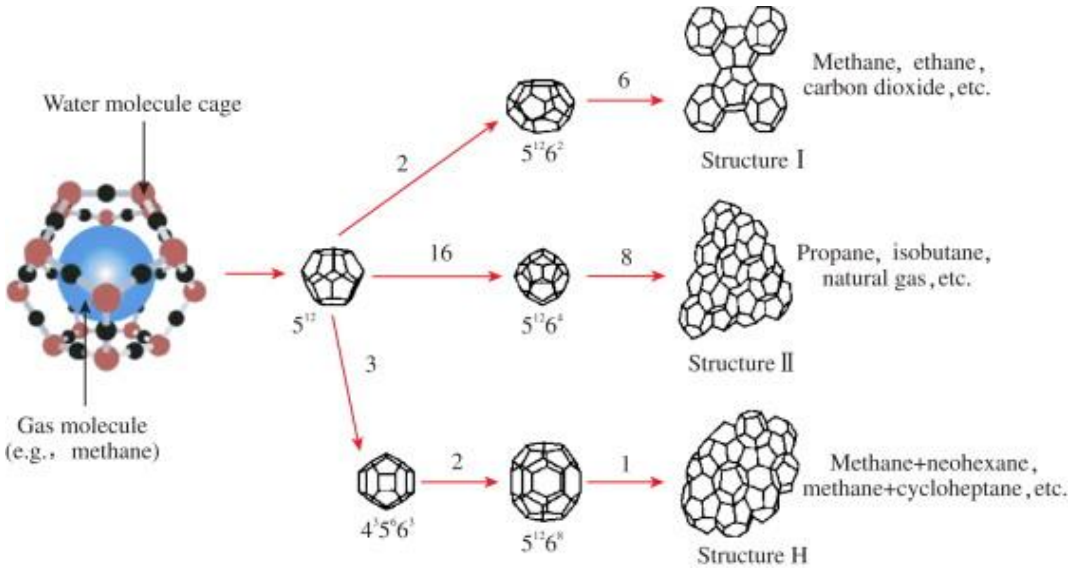

Figure 1.1 Structure and type of gas hydrates [8]. Depending on the type of hydrocarbon molecule, different cage structures exist where the unit cell for sI and sII has two types of cage structures, and sH has three types of cage structures. The number and corresponding superscripts for a cage structure indicate the number of edges in each face and the number of corresponding faces in the cage lattice.

Formation of hydrates is characterized by kinetics and thermodynamics-related constraints. Kinetic constraints result in slow growth/conversion rates and very long induction/formation times. Thermodynamic constraints are related to the thermodynamically stable pressure-temperature (p-T) region required for hydrate formation. Nucleation of hydrates is typically characterized by the formation of the first 'cluster' of stable hydrate molecules, and is characterized by delayed induction/wait times typically ranging from hours to days, especially in a quiescent medium. While several experimental and theoretical studies have investigated the effect of various promotion techniques for accelerating nucleation, it still remains a challenge due to the stochastic nature and the small length scales associated with the nucleation process. The primary focus of this dissertation is to study both kinetic and thermodynamic constraints

associated with nucleation of hydrates using experimental and machine-learning tools. Additionally, the practical utility and the techno-economic factors associated with using such hydrates as carbon capture tools is also assessed.

Chapters 2 and 3 detail studies investigating the role of electric fields and surface chemistry on the kinetics of hydrate nucleation for two kinds of hydrates-forming systems (miscible liquid-water and gas-water systems). The role of electric fields in accelerating crystallization processes has been extensively investigated for freezing of water (electrofreezing) [9]. Since the physics underlying hydrate and ice nucleation are similar in some aspects, it is expected that the application of an electric field will enhance hydrate nucleation kinetics as well. Since hydrate formation is a two-stage process comprising nucleation and growth, aluminum metal foam has been used as electronucleation electrodes to speed up nucleation (due to electric fields) and growth (due to high thermal conductivity of the foam medium to remove the heat released). Metal foams enhance the effective thermal conductivity of the hydrate precursor solution and assist in rapid removal of the heat of hydrate formation, thereby accelerating hydrate conversion process. Furthermore, the higher surface area to volume ratio and the presence of numerous nucleation sites on the foam surface act in coherence with the electric field to further promote hydrate formation. *The usage of open-cell aluminum metal foams as electronucleation electrodes leads to instantaneous formation of tetrahydrofuran (THF) hydrates (with induction time of the order of a few seconds) and reduces the stochasticity of the nucleation process*.

Having demonstrated the utility of aluminum metal foam in accelerating electronucleation of THF hydrates (which are used as model hydrates to mimic gas hydrate formation in laboratory conditions), Chapter 3 details a study on the influence of

Al surfaces on the nucleation kinetics of CO_2 hydrates which are formed under high-pressure conditions. The role of various chemical and mechanical promotion techniques on gas hydrate formation, such as surfactants, mechanical stirring etc., has been extensively studied [10]–[13]. While such techniques lead to faster hydrate formation, they are either energy-intensive (energy required for scaled-up mechanical stirring) or have adverse environmental effects (foaming effect due to surfactants). Since hydrate nucleation is primarily a heterogeneous interfacial phenomenon, it is expected that nucleation process should be tunable via control of surface chemistry (surface in contact with gas and liquid). Accordingly, *it is observed that the use of aluminum metal significantly promotes the nucleation of CO_2 gas hydrates, with inductions times spanning from 8 minutes to a few hours*. It is noted that this promotion, resulting from interfacial chemical reactions occurring at the Al-water interface, cannot be replicated by salts of Al or any other metal such as copper or stainless steel.

Chapters 4 and 5 investigate the thermodynamics of gas hydrate formation. Hydrate-formation studies involve tuning thermodynamic formation conditions by adding inhibitors such as electrolytes and alcohols or promoters such as quaternary ammonium salts and THF. One application concerns the formation of methane hydrates in pipelines which can cause significant plugging issues, resulting in enormous costs for prevention/removal [14]. Thermodynamic hydrate inhibitors (THIs) are commonly used to shift the hydrate formation conditions to higher pressure and/or lower temperature regions, thereby delaying hydrate formation in such applications. However, such THIs are highly volatile in nature and harmful to the environment. Furthermore, effective operation of such THIs requires injection of large quantities of chemicals, further increasing the recovery costs. A new class of inhibitors called ionic liquids (ILs) that attract water molecules via electrostatic interactions have been studied due to their

combined dual influence involving thermodynamic as well as kinetic inhibition. However, such ILs are environmentally unfriendly and expensive. In order to overcome the challenges mentioned above, amino acids were introduced as a new class of gas inhibitors in 2011 [15]. Since amino acids are environmentally friendly and less expensive when compared to other THIs, they have been gaining traction as alternatives for thermodynamic inhibition of gas hydrate formation. The procedure to quantify the inhibition effect of such THIs is to experimentally measure thermodynamic phase equilibria using well-established experimental methods. However, these procedures are time intensive and often result in generation of limited number of data points after long duration experimental runs. Chapter 4 discusses a novel method for rapid measurements of thermodynamic phase equilibria for CO_2 hydrates in the presence of amino acids. *The thermodynamic inhibition behavior of five amino acids has been studied using water droplets as individual microsystems for hydrate formation.* Additionally, the kinetic behavior of these amino acids has also been studied, and a correlation has been observed between the hydrophobic behavior of the structural side chains and the magnitude of the inhibition effect.

Chapter 5 studies the role of machine learning-based techniques to predict the thermodynamic phase equilibria of gas hydrates in the presence of salt-based inhibitors. Overall, *ML models have been developed using fundamental thermodynamic parameters of the constituent gases or chemicals in the system as input features*. The models exhibit excellent prediction accuracies and have been able to predict the thermodynamic formation conditions for gas hydrates with a coefficient of determination (R^2) accuracy as high as 99.56% and an Average Absolute relative deviation (AARD) error as low as 0.086%.

While Chapters 2-5 are devoted to fundamental investigations of the thermodynamics and kinetics of hydrate formation, Chapter 6 studies the utility of using hydrates as a tool to capture and store CO_2 generated by steam methane reforming (SMR) of landfill gas (LFG) collected by various counties across Texas. Specifically, a hydrates-based carbon capture system has been coupled with an SMR system to generate H_2 from landfill gases and store CO_2 in the form of hydrates. While the cost for hydrogen production has been evaluated, *the techno-economic factors involved in setting up a hydrates-centered facility for carbon capture across various counties in Texas have also been analyzed in detail*. In doing so, the energetics associated with the compression and refrigeration process required for hydrate formation have been delineated and an analysis of the capital and operating costs associated with such a production facility has been carried out. This study constitutes a starting point for assessments of the technical and techno-economic viability of a hydrates-centered future for the carbon capture and natural gas industry.

1.1 LITERATURE REVIEW

1.1.1 Past studies on electric field-assisted freezing of water and hydrates[1]

There are numerous studies on various aspects of water-ice phase transitions. Since there are numerous parallels between the principles underlying ice and hydrate formation, this section provides a detailed review of the fundamental mechanisms underlying electric-field and electric-charge stimulated nucleation of ice and hydrate. While electrofreezing is a vast area with numerous studies targeting the fundamental

[1] The content of this section has been published as the following journal review article: Acharya, P.V. and Bahadur, V., 2018. Fundamental interfacial mechanisms underlying electrofreezing. Advances in Colloid and Interface Science, 251, pp.26-43.

aspects of freezing phase change behavior, electronucleation of hydrates is a relatively new field of study.

The majority of experimental studies on electrofreezing have utilized DC fields. The first-ever demonstration of electrofreezing was by Dufour [50] in 1861, wherein electric fields were observed to initiate freezing in supercooled water droplets. Following this study, there was a century-long hiatus on experimental studies. Subsequent studies can be conveniently summarized and analyzed by grouping them into three time periods as detailed ahead.

The period from 1951-1980 have included experimental studies on the role of electrical phenomena in triggering ice nucleation in cirrus clouds [16]. Some studies also analyzed ice formation in the vicinity of high voltage conductors [17]. These studies led to the emergence of multiple theories and mechanisms underlying electrofreezing, many of which were validated in subsequent experimental studies and molecular dynamics simulations.

Schaefer (in 1953) observed the freezing of supercooled water droplets resting on a plastic surface subjected to electric discharges from a Tesla coil [18]. No freezing was noticed when supercooled water droplets floating in air in a cold chamber were subjected to the same discharge. This suggested the combined interplay of an electric field and a surface on electrofreezing. In early studies, freezing water droplets were exposed to an electrical discharge since the electric fields exceeded the threshold for electrical breakdown. In 1963, Pruppacher [19] designed experiments wherein water droplets were subject to electric fields of up to 6×10^6 V/m without the surrounding medium undergoing breakdown. Results indicated that electrofreezing was not due to particulate matter produced in corona discharges or the polarization of water. *Ice nucleation was always initiated at a moving three-phase contact line on a surface in the presence of an*

electric field; this was observed for DC and AC electric fields. It was proposed that the movement of the three-phase line results in charge transfer from the surface to the bulk of the liquid, resulting from the movement of the electrical double layer. These incoming charges stabilize the accumulating water clusters in the bulk of the supercooled droplet, thereby producing an ice nucleus that initiates freezing upon reaching a critical size.

Loeb [20] proposed that the water surface gets drawn out into tiny filaments when the force resulting from the applied electric field overcomes the surface tension. This results in the formation of minute crystallites at the tip of these filaments, which at length scales less than 1 μm diameter act as nucleating agents [20]. Based on Prupaccher's results [19], Loeb proposed the following necessary prerequisites for nucleation:

- The liquid surface needs to be drawn out into tiny filaments of a dimension comparable to the size of a crystallite.
- A solid near the nucleation site is essential to dissipate the latent heat of crystallization (this could potentially explain the non-freezing behavior of droplets when suspended in a chamber, as reported by Schaefer [18]).
- Space is required near the contact line for water to expand on freezing.

Further studies [21], [22] showed that electrofreezing was triggered by the disruption of the droplet-air interface instead of the movement of a three-phase line. Such disruptions can be triggered electrically or mechanically. Electric-field-induced surface disruption led to longer filaments when compared to mechanical disruption, thereby enhancing nucleation to a larger extent. This is evident from the work of Abbas and Latham [21], wherein a higher fraction of droplets froze (Figure 1.2) when disrupted by an electric field, as against mechanical disruption from a penetrating insulating fiber.

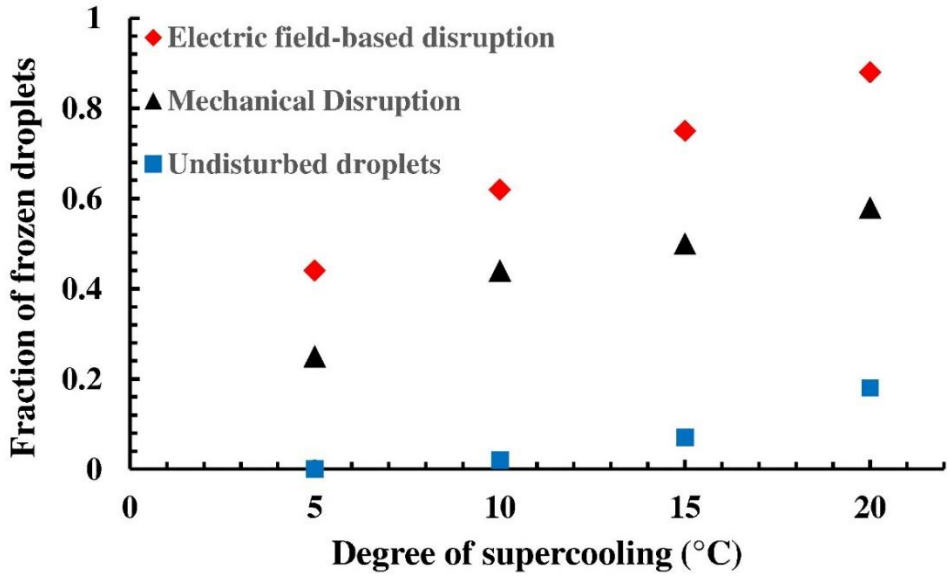

Figure 1.2. Fraction of water droplets (radius: 1 mm) frozen under different conditions and temperatures. Electric fields enable more effective freezing as compared to mechanical disturbances. This plot is based on data reported in Reference [21] and published in [9]. The applied electric field ranged from 0-15 x 10^5 V/m.

Smith et al. [23] studied the freezing of supercooled water droplets (radius: 2 mm) at temperatures ranging from 0 to -12 ^oC, falling vertically through electric fields. It was reported that the fraction of frozen droplets increased steadily from 0 at -5 ^oC to 0.6 at -10 ^oC only in cases where the electric field was turned on. Notably, the results are close to the findings of Abbas and Latham [21] (Figure 1.2). No enhancement in the freezing fraction was observed in the absence of an electric field. Furthermore, the probability of freezing was unaffected by the passage of a spark through the medium. It was suggested that the collapse of cavities (due to cavitation of dissolved gases in the liquid) resulting from vibrations of the droplet surface increases the local pressure of the surrounding fluid. This elevates the equilibrium freezing temperature of the surrounding fluid, thereby inducing nucleation at a lower degree of supercooling.

In 1973, Pruppacher [24] discussed a new mechanism to explain electrofreezing, which used the concept of adsorbed layers proposed by Evans [25]. According to Evans [25], nucleation in the bulk of a liquid proceeds from a thin layer of interfacial water firmly adsorbed on the surface, against the conventional notion that freezing initiates directly on the surface. The molecules in a freshly adsorbed water layer can be easily reoriented, and ice nucleation is quicker when compared with a firmly adsorbed layer. For firmly adsorbed water layers oriented by the surface, a higher degree of supercooling is required to enable a 2-D transformation of this layer to a structure similar to that of ice. However, when this layer freshly wets the surface in a transient fashion (as in the case of a moving contact line as observed by Pruppacher [19]) or is loosely bonded to the surface, it is energetically favorable to bring about the same transformation at a lower supercooling by applying an electric field. This theory of disordered layers has been investigated via molecular dynamics simulations, which confirm the presence of such adsorbed layers and their role in ice nucleation [26]–[29].

In 1951, Rau [30] studied the electrofreezing of water droplets on a chromium surface (negative electrode). Droplets were seen to freeze following an electric spark produced by a positive point electrode on top of the droplet. Similarly, freezing was initiated by a spherical electrode covered with a dielectric without the initiation of a spark at temperatures as high as –4 ^{o}C for electric fields ranging from 2-6 x 10^5 V/m. It was suggested that the electric field rearranges water clusters due to polarization, thereby creating a structure more favorable for ice nucleation.

A similar theory was proposed by Salt [31] to explain the freezing of supercooled water droplets under an AC field. Pruppacher [19] refuted this theory based on observations that electric fields as high as 3 x 10^6 V/m were insufficient to induce freezing in a water column. Gabarashvili & Gliki [32] noted that the electric field

experienced by a layer of water molecules situated adjacent to the surfaces of charged particles would be enhanced due to the presence of surface projections. The resulting polarization of water molecules adjacent to the surface stabilizes subsequent layers, thereby assisting freezing. The electric field near the surface projections of naphthalene particles charged to 3000V was estimated to reach 7.2 x 10^8 V/m [32]. This theory of polarization of local water molecules (adjacent to charged surfaces) has also been studied via experiments and simulations in recent years.

It is noted that not all early studies on electrofreezing yielded positive results. Dawson and Cardell [33] (1973) measured the freezing probability of droplets supercooled to temperatures ranging from –8 to –15 ^oC, under the influence of electric fields up to 10^6 V/m. No electrofreezing was detected even under three favorable circumstances: high electric fields that led to droplet instability, collision of charged and uncharged droplets in the electric field, and the presence of corona discharge. Similar results were reported by Doolittle and Vali [34] (1974), wherein it was observed that electric fields up to 6 x 10^5 V/m had no intrinsic effect on the heterogeneous freezing of water droplets containing leaf-derived nuclei and silver iodide based colloids.

There were relatively fewer experimental studies in the last two decades of the twentieth century (1981-2000); however, some studies in this period were the basis for significant later progress. Shichiri and Nagata [35] studied the influence of electric current and electrode material on the nucleation of ice crystals. They observed that an electric current elevated the nucleation temperature. Furthermore, *nucleation initiated at the cathode and anode for electrode materials having low and high ionization tendencies*, respectively. Another mechanism associated with the flow of electric current is bubble generation due to electrolysis at the electrodes. It was inferred by Sivanesan & Gobinathan [36] that *electrolytic bubble generation and its subsequent collapse, along*

with a favorable orientation of the water layer adjacent to the electrodes, could be possible mechanisms underlying electrofreezing. Shichiri & Araki [37] proposed that the attraction of the dipoles (in water) to surface charge leads to supersaturation of water molecules in a bubble near the electrode surface. This results in heterogeneous nucleation of an ice crystal in the vapor phase. When the bubble departs, this crystal deposits on the electrode surface and acts as the seed for further nucleation/growth.

The structural similarity of the substrate with that of ice has been considered an important criterion for a solid to be a good ice-nucleant [38]. Gavish et al. [39] studied freezing on hydrophobic surfaces of polar and non-polar amino acid crystals with a crystalline structure different from ice. Crystals that exhibited a polar axis demonstrated freezing temperatures higher by 3-5 °C when compared to their non-polar counterparts. It was initially hypothesized [39] that concentrated electric fields within the cracks in the crystals, with a magnitude large enough to induce a phase transformation of the interfacial water molecules, were responsible for promoting nucleation. However, similar experiments later showed that the pyroelectric charge is responsible for electrofreezing instead of the hypothesis proposed by Gavish et al. [39].

Braslavsky and Lipson [40] (1997) reported an electrofreezing temperature of –0.1 ^{o}C, which is the highest recorded freezing temperature under electric fields. However, this was accompanied by a very long crystal propagation time (8 hours) and was dependent on the long-term temperature stability of the surrounding growth medium. The experiment involved supercooling part of the liquid locally with a Peltier cooling system followed by the passage of high voltage pulses (10μs pulse of 10,000V) through the liquid.

The period since 2000 has produced several significant studies, which clearly highlight the varied, multiphysics and complex mechanisms underlying electrofreezing.

Hozumi et al. [41] and Hozumi et al. [42] studied the influence of electrode material and geometry on electrofreezing. *Nucleation was observed to initiate from the anode when the electrode metal had a high ionization tendency*. It was hypothesized that polynuclear coordination compound-based complexes were being formed; the similarity of the structure of these complexes to the hexagonal structure of ice was hypothesized as being responsible for electrofreezing. This study established the following order of metals, arranged in descending order of their ability to electrofreeze water: Al, Cu > Ag > Au > Pt > C. Shichiri and Nagata [35] reported similar results earlier, who correlated the propensity to electrofreeze with the ionization potential. Having explored the influence of material properties, Hozumi et al. [42] studied the effect of electrode geometry on electrofreezing, using various combinations of flat and sharp electrode geometries for the cathode and anode (Figure 1.3). The experimentally determined propensity to electrofreeze, in decreasing order, was [73]:

$$Flat_a - Flat_c > Flat_a - Sharp_c > Sharp_a - Flat_c > Sharp_a - Sharp_c$$

where a & c denote the anode and cathode, respectively. The flat geometry configuration of anode houses a higher surface density of ions due to the presence of numerous micro-convex surfaces compared to a sharp geometry. This results in a larger density of interfacial coordination compounds, which translates to accelerated electrofreezing.

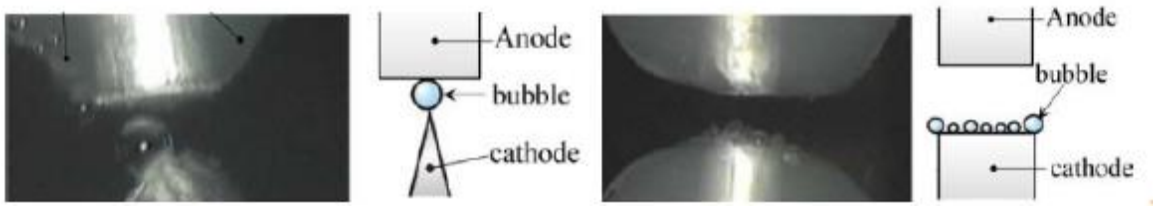

Figure 1.3. Electrolytic bubble formation at cathode [42] (a) A sharp cathode produces a larger hydrogen bubble, which interferes with coordination compound formation at the anode (b) A flat cathode, on the other hand, produces a large number of smaller bubbles which do not affect reactions occurring at the anode. This explains the observed higher electrofreezing tendency with flat cathodes as compared to a sharp cathode. Figures 1.3 reprinted with permission from Reference [42]. Copyright: 2005 by Elsevier.

Choi et al. [43] observed electric field-dependent freezing of water confined between two electrodes with molecular-level spacing at room temperature. Figure 1.4a shows a schematic of the experimental setup. The concept underlying confinement-induced freezing is reducing translational entropy of water molecules confined in gaps (a few molecular layers thick), which induces solidification. Electric fields enhance this effect by inducing a perturbation in the water network by exerting a torque on the molecules to restructure them into an ordered hydrogen-bonding network. It was reported [43] that the critical gap for inducing freezing was approximately 14 Angstrom, the thickness of 3-4 molecular layers of water. The electric field required ranged from (2-8) x 10^6 V/m. The electric field reported in this study is much lesser than molecular dynamics simulations-based predictions of electric fields required to induce dipole polarization in water (>10^9 V/m). It is noted that very high electric fields (~10^9 V/m) are challenging to apply due to limitations in experimental setups and the dielectric breakdown strength of water, which is (O)10^7 V/m and (O)10^8 V/m for millimeter and micrometer-scale volumes of water, respectively [44], [45]**.** Furthermore, the effective electric field in the

inside (bulk) of a spherical droplet (E_{in}) is less than the electric field outside the droplet (E_{out}), when the droplet is not in direct contact with electrodes. The relation is [46]:

$$E_{in} = \left(\frac{3\varepsilon_{out}}{\varepsilon_{fluid} + 2\varepsilon_{out}} \right) E_{out} \tag{1.1}$$

where ε_{out} & ε_{fluid} denote the dielectric constants of the surrounding medium and water, respectively. This relation suggests that an applied electric field of (O)10^9 V/m would effectively only produce an internal field of (O)10^7 V/m, thereby attenuating the applied field by at least two orders of magnitude inside the droplet.

Stan et al. [47] quantified the influence of an electric field on homogeneous nucleation; a schematic of the experimental setup is shown in Figure 1.4b. Discrete water droplets traveled in a flow cell with a transverse electric field, where they cooled until they froze. Based on the experimental results and thermodynamic analysis, it was estimated that the minimum electric field to produce any perceivable change in nucleation is 1.8 x 10^7 V/m. Furthermore, it was reported that electric fields of O(10^7) V/m enhance the nucleation rate due to the formation of ferroelectric ice (ice XI).

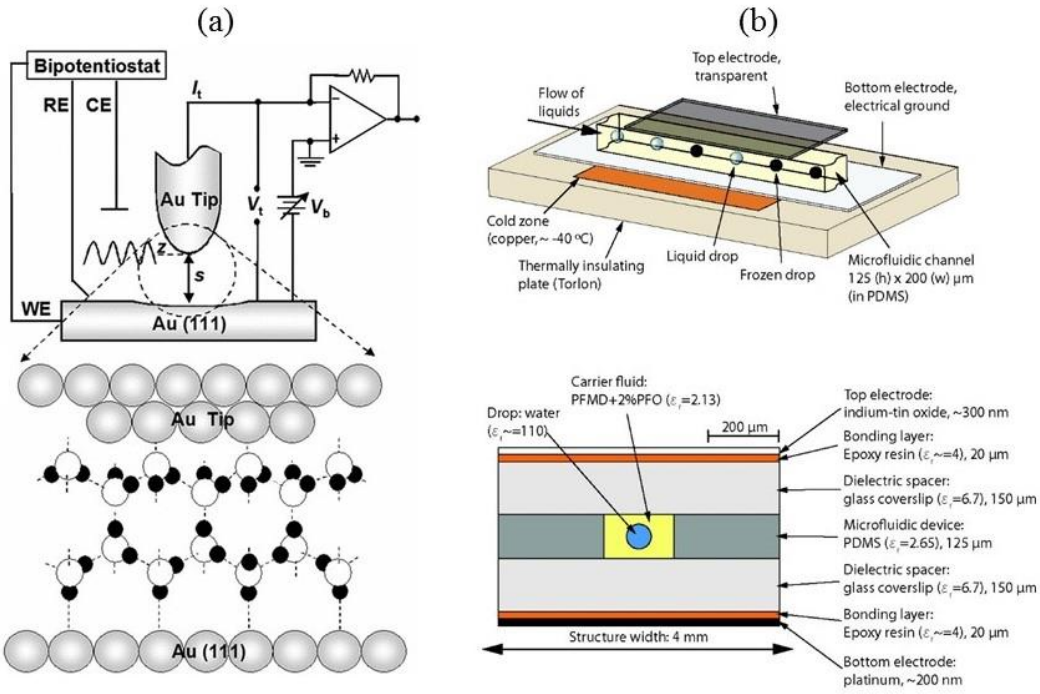

Figure 1.4. (a) Schematic of experimental setup to observe confinement-induced freezing under an electric field [43]. Water is present in the gap between the gold tip and the negatively biased gold (111) surface. A piezo driver of known sensitivity controls gap spacing. The black and white spheres represent hydrogen and oxygen molecules in a bilayer of water molecules, respectively. (b) Schematic of experimental setup to study the role of an electric field on homogeneous nucleation of water droplets [47]. Droplets travel through a microfluidic channel cooled to -40 ^{o}C under a transverse electric field. Figure 1.3(a) reprinted with permission from Reference [43]. Copyright: 2005 American Physical Society. Figure 1.4(b) reprinted with permission from Reference [47]. Copyright: 2011 American Chemical Society.

Recent studies have analyzed electrofreezing via experiments using an experimental configuration typically used for studies on electrowetting. Electrowetting [48] is a well-known microfluidic technique to change the wettability of droplets via an applied electric field. This electric field exists in a dielectric layer beneath a static droplet (Figure 1.5b). The droplet has higher electrical conductivity than the dielectric and can be considered equipotential. Nakajima et al. [49] (2007) investigated the effect of 3-phase

contact line movement (using electrowetting-based actuation) on freezing of supercooled water droplets on a hydrophobic surface. It was observed that contact line motion enhances electrofreezing; these results corroborate the observations of Pruppacher [19], almost five decades ago. Daniel et al. [50] studied the influence of charge-induced filamentation on the freezing of supercooled water droplets; this filamentation results from a Coulombic instability when the surface charge exceeds the Rayleigh limit. No perceivable influence of filamentation in inducing freezing was observed.

Yang et al. [51] (2015) studied the dynamics of ice-nucleation in supercooled water droplets in an electrowetting setup using electric fields of (O) 10^6 V/m. High-speed visualization (Figure 1.5a) showed that nucleation initiates at the three-phase line and that this phenomenon is polarity-independent. Importantly, it was seen that contact line motion due to the electric field was essential for nucleation. Contact line motion in the absence of an electric field, as well as the application of an electric field without contact line motion, failed to initiate nucleation.

Carpenter and Bahadur [52] used an electrowetting setup to isolate the influence of electric field and electric current on electrofreezing (Figure 1.5b). The maximum electric field used in this study was 80 x 10^6 V/m, which is 13X higher than the highest field (6 x 10^6 V/m) utilized in previous studies. Electric field (in the absence of current flow) elevated freezing temperatures by more than 15 ^{o}C, with the polarity-independent electrofreezing effect saturating at high electric fields (>20 x10^6 V/m). Additionally, by intentionally introducing pinholes in the electrowetting dielectric layer, passages for current flow were established, and electrofreezing experiments were conducted in the presence of electric current. Current flow enhanced the electrofreezing effect over that obtained by electric field alone (Figure 1.5b). Similar results were also obtained by Shichiri and Nagata [53].

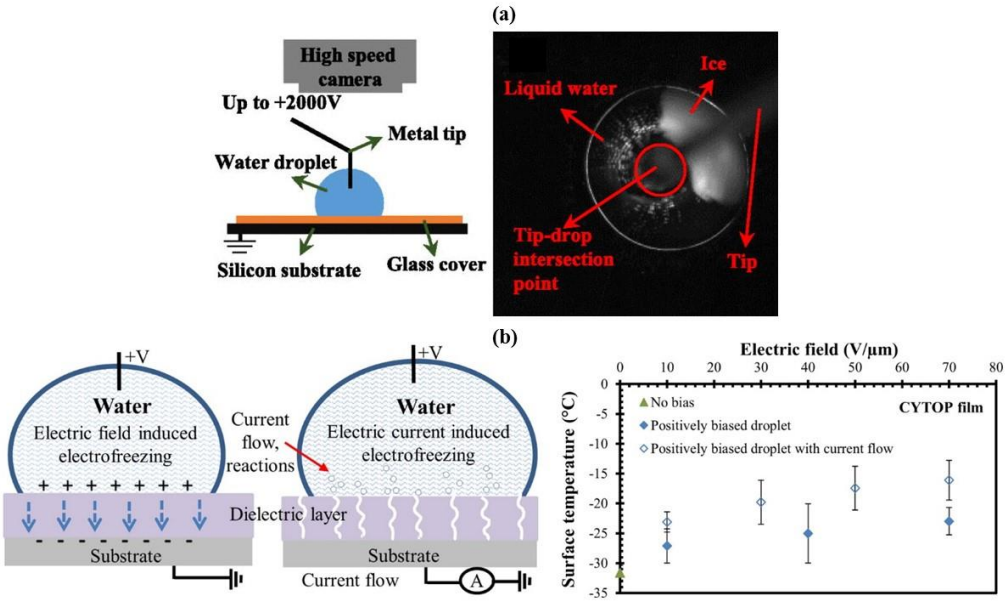

Figure 1.5. Electrowetting-based experimental setups used for studies on electrofreezing (a) Top view of nucleation and phase front propagation inside a droplet [51]. Electrofreezing commences at the three-phase line, with multiple nucleation points at higher voltages. (b) Experiments to isolate the influence of electric field and current flow on electrofreezing [52]. Results indicate that both phenomena influence electrofreezing. Figure 1.5(a) reprinted with permission from Reference [51]. Copyright: 2015 AIP Publishing LLC. Figure 1.5(b) reprinted with permission from Reference [52]. Copyright: 2015 American Chemical Society

Carpenter and Bahadur [54] showed for the first time that electrofreezing could significantly accelerate the nucleation of tetrahydrofuran (THF) hydrates. A significant challenge underlying the synthesis of hydrates is the long induction (wait) time before hydrates form. This can range from hours to days for quiescent systems and is a significant hindrance to the realization of applications that require synthesis of hydrates. Carpenter and Bahadur observed that the induction time of THF hydrates could be significantly reduced (100X) by applying an electric potential across the hydrate precursor solution. Electric voltages applied in the absence of current were observed to have delayed nucleation kinetics when compared to experiments carried out with electric

current passing through the solution. Induction times of the order of a few minutes were reported at electronucleation voltages of 100V (in the presence of electric current). The promoting effect was ascribed to current flow leading to bubble generation (Figure 1.6) via localized electrolysis which acted as nucleation sites for hydrate formation.

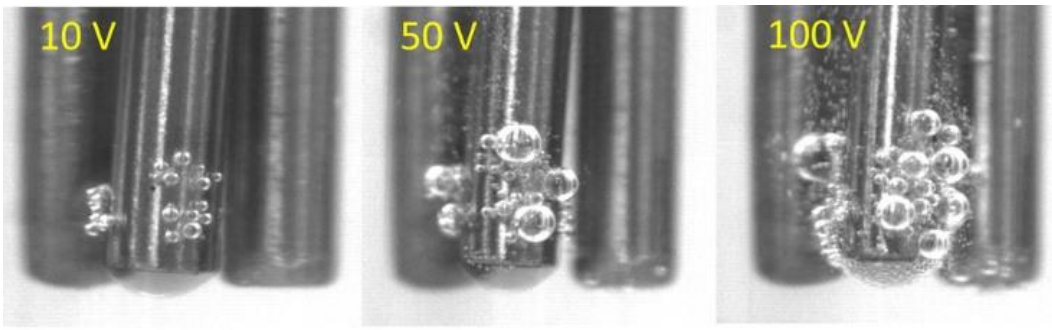

Figure 1.6 Formation of bubbles on cathode during electronucleation experiments at different voltages. Such bubbles act as nucleating sites with the convection currents and pressure variation with bubble growth, further promoting hydrate formation. Figure 1.6 reprinted with permission from Reference [54]. Copyright: 2016 American Chemical Society; further permission related to the material excerpted should be directed to the ACS.

1.1.2 Past studies on methods to accelerate nucleation of hydrates

Most of the water freezing-related studies capture the effect of varying electric fields on the degree of supercooling (excess cooling below the equilibrium temperature), whereas studies characterizing hydrate formation predominantly deal with induction time, which is defined as the time required to form a stable hydrate nucleus upon entering the thermodynamically stable p-T region for hydrate formation. Induction time characterizes a system's ability to maintain its metastable equilibrium state without undergoing transformation into hydrate. Long induction times are beneficial for applications such as flow assurance of gas pipelines, while short induction times are needed for gas

separation, carbon capture and storage, desalination, and transportation and storage of natural gas via hydrates.

Key techniques to promote hydrate formation by shortening the induction time can be grouped into three major categories as summarized in Table 1.1: usage of chemical additives, presence of an extra surface and mechanical techniques such as stirring and spraying. The addition of chemicals such as THF [55] and quaternary ammonium salts such as TBAB [56] that form semiclathrate hydrate at ambient pressure conditions has been observed to shorten the induction time of mixed CO_2/N_2 hydrate systems. It is noted that the promoting effect of chemical additives is usually studied in the presence of mechanical stirring, which promotes hydrate formation kinetics significantly by enhancing the effective gas-liquid interfacial area [57]. Experiments carried out with methane hydrates at around 4 MPa and 273.95K in the presence of mechanical stirring reported induction times of 12, 19 and 56 mins with some cases not yielding hydrate formation even after 1440 mins [57]. Induction times as early as 2 mins and 1.7 mins have been reported for CH_4 (8 MPa and 4 ^oC) and CO_2 (3.1 MPa and 1 ^oC) hydrates for stirred tank reactors. Several studies have reported beneficial effects on hydrate formation via mechanical stirring [57]–[60] as well as when liquid is sprayed through a nozzle [61], [62].

The usage of surfactants has been observed to reduce the induction time within timeframes of a few hours[10]–[13]. Sodium dodecyl sulphate (SDS), in particular, has been highlighted for its ability to accelerate hydrate formation in non-stirred systems by inducing a morphological change in the hydrate structure to ensure that gas water contacts are maintained [12], [13]. Zhang et. al. reported induction times in the range of 0.57-13.03 hours for nominal SDS concentrations ranging from 260-10000 ppm at 271K and 274K and 7 MPa pressure for methane hydrates in a non-stirred batch reactor [11].

Lirio et al. observed that CO_2 hydrates start forming at induction times of 60 mins in the presence of 5 ppm SDS which further decreased to 13 mins in the presence of 5ppm SDS+5mol% THF [63].

Similarly, the presence of metal surfaces in the form of silver nanoparticles has been reported to reduce the induction time and promote the formation for methane[64]–[66], ethane [67], and carbon dioxide hydrates [68]. Such metal surfaces serve as nucleation sites and therefore increase the probability of heterogeneous nucleation. Porous media and metals, in particular, have been extensively studied to promote hydrate formation due to their high surface area to volume ratio, which helps in improving gas-liquid contacts and interactions [69]–[74]. Different kinds of porous media such as silica gel pores [73], [75]–[77], porous glass [78]–[80], silica sand particles [81] and aluminum foam have been used in hydrate promotion studies in the past. An average induction time of 27.5 mins was reported for THF hydrates in BZ-06 porous medium using 3 mol% THF solution [80]. Induction times in the range of 20-200 minutes were observed for methane hydrate formation in a porous media comprised of silica and alumina particles mixed with SDS solution and pure water [81].

Table 1.1 Summary of induction times reported in previous studies using various promotion techniques.

Authors	Year	Hydrate	Nucleation promotion technique	T(K)	P(MPa)	Induction time (min)
Skovberg et al. [57]	1993	Methane	Stirring	273.95	4	56
				273.95	4	19
				273.95	4	19
				273.95	4	12
				275.95	4	>1440
				274.95	4	>1440
				274.95	4	>1440

Table 1.1 (continued)

Skovberg et al. [57]	1993	Ethane	Stirring	274.95	0.9	51
				274.95	0.85	51
Hao et al. [58]	2007	Methane	Stirring	273.5	5	230
Liu et al [80]	2015	THF	Porous medium: Soda glass (BZ-06)	279.15	-	52
						31
						146
						232
						42
						152
						57
						43
						33
						90
						77
						49
Zhou et al. [82]	2014	Carbon Dioxide	Stirring+ Nanoparticles: Graphite	277.15	2.5	8.7
					3.5	7
					4.5	6.3
					5.5	5.7
					6.5	4.3
			Stirring		2.5	47.3
					3.5	38.7
					4.5	32.3
					5.5	23.9
					6.5	20.1
Zhou et al. [83]	2018	Carbon Dioxide	Stirring + Graphite nanoparticles + TBAB	277.15	4.5	4.2
						3.4
						3.5
						3
						2.8

Table 1.1 (continued)

Kumar et al. [84]	2015	Carbon dioxide	SDS + Porous medium (Silica sand)	274.65	3	4.5
						9
			SDS + Porous medium (Silica gel)			3
						15
						34
Liu et al [71]	2019	Methane	SDS	274.6	7.3	66
						150
						222
			SDS + Porous medium (SiC foam)			684
						1338
						1194
						90
						294
						0
						78
						228
						0
Lirio et al. [62]	2013	Carbon Dioxide	SDS	279.3	3	60 (±2)
			THF	289.1		17 (±2)
			SDS+THF	290.1		13 (±2)
				288.4		25 (±2)
Zhang et al. [11]	2007	Methane	SDS	271	7	130.2
				274		24.6
Liu et al. [81]	2018	Methane	Porous medium: Silica	275.15	7	160
						110
						310
						200
						150
						170
						200
						160
						170

Table 1.1 (continued)

Liu et al. [81]	2018	Methane	Porous medium: Alumina	275.15	7	100
						160
						150
						180
						190
						150
						200
						160
						170
Shi et al. [85]	2017	Carbon dioxide	TBPB + stirring	276.65	1.7	6.3
						17.2
						12.5
				278.05		6.8
						44.3
						23.3
				278.25		13.5
						2
						1
				278.35		1.8
						1.5
						2
				278.45		1.5
						1.5
						1.3
				278.75		4.5
						2.3
						1.3
				277.95		1.8
						1.6
						1.8
				276.15		2.8
						2.8
						2.6

1.1.3 Past studies on thermodynamic inhibition of gas hydrate formation using amino acids

Hydrate formation is constrained by very long induction (wait) times, and the previous sections review various methods that have been used in the past for accelerating hydrate nucleation kinetics. However, since gas hydrates form at extreme conditions of high pressures and low temperatures, the thermodynamics of hydrate formation has also been the subject of numerous research studies. This section explicitly reviews studies that have used amino acids to inhibit thermodynamics of hydrate formation and discusses techniques that have been very commonly used to measure the inhibition effect of different additives on thermodynamic hydrate phase equilibria.

Amino acids are structurally composed of a carboxylic group (-COOH), an amine group (-NH_3) and a residual side-chain group that can either be an apolar alkyl chain (hydrophobic) or a positively or negatively charged polar chain (hydrophilic). Such amino acids alter the structure of water molecules by virtue of hydrogen bonding of amine and carboxylic groups, and electrostatic interactions due to the formation of zwitterions, thereby reducing their activity coefficient. A systematic review of literature employing the use of amino acids as gas hydrate inhibitors [86] observed that most studies had been carried out to investigate the kinetics (rather than the thermodynamics) of gas hydrate formation in the presence of amino acids, with a focus on CCS and gas storage-related applications. It is noted that gas hydrates-based research employing amino acids for modifying thermodynamics of hydrate formation is in its nascent stage.

Overall, nine amino acids (proline, glycine, alanine, arginine, serine, valine, lysine, methionine, histidine) have been studied for CO_2, CH_4 and natural gas (NG) hydrate formation inhibition [86]. Sa et al. [15] captured the influence of hydrophobic amino acids such as glycine, L-alanine and L-valine on the three-phase (hydrate-liquid-

vapor) equilibrium conditions of CO_2 hydrate. Based on their analysis, the following inhibiting order for amino acids (based on mol%) was reported in decreasing order: L-valine > L-alanine> glycine, the inhibition effect being attributed to the molecular structure of the residual functional group. In a follow-up study [87], the perturbation of the molecular structure of water in the presence of amino acids was observed using Raman spectroscopy, wherein the inhibiting efficiency of CH_4 and Natural gas hydrates was observed to depend on the physicochemical property of amino acids. L-proline was reported to be an excellent THI due to its strong hydrophilicity with water. In another study, the behavior of five amino acids (glycine, alanine, proline, serine and arginine) was studied on methane hydrate HL_wV conditions [88]. While all amino acids exhibited hydrate inhibition, glycine showed the highest inhibition impact with an average depression temperature of 1.78K at 10 wt% [88]. Dissociation enthalpies calculated using the Clausius-Clapeyron equation indicated that the amino acids did not participate in hydrate cage occupation during hydrate formation. The inhibition effect of five amino acids (glycine, alanine, proline, serine and arginine) was studied for carbon dioxide hydrate [89], wherein glycine was reported to exhibit the highest inhibition strength with an average depression temperature of 1.83 K at 10 wt%.

Most studies evaluating the impact of amino acids or conventional THIs on hydrate phase equilibria employ the isochoric method with step heating procedure. In this method, the system is charged with a certain amount of water+promoter, pressurized with the hydrate forming gas (or mixture), and cooled below the hydrate formation temperature to form hydrates. Following this, the system is sequentially heated in small steps to dissociate the formed hydrates, leading to an increase in system pressure until it is outside the hydrate stability region, where only a slight increase in pressure is observed. When tracing this procedure on the p-T diagram, the equilibrium point is

characterized as the intersection of the heating curve (corresponding to hydrate dissociation) and the cooling curve, or the point where a change in slope of the dissociation trace is observed [90]. More recently, a novel design based on a droplet resting on a bilateral temperature-controlled stage was utilized to evaluate hydrate liquid vapor (HL_wV) phase equilibria measurements [91], [92]. The fundamental ideology behind this technique is that for a hydrate-covered droplet resting on a temperature-controlled stage, with a temperature gradient existing across the droplet, the region of the stage above the HL_wV temperature will dissociate, leading to a distinct visual liquid-hydrate boundary. This boundary, therefore, demarcates the location at which the temperature crosses the HL_wV curve.

1.1.4 Past studies on methods to predict thermodynamic conditions for hydrate formation

The previous section outlined the experimental techniques commonly used for measuring hydrate phase equilibria in the presence and absence of different promoters/inhibitors. In addition to above techniques, various analytical/empirical modeling approaches have been proposed to predict hydrate dissociation temperatures (HDT) that can be grouped into four categories. The first two are the K-value method (uses vapor-solid equilibrium constants and K-value charts) [93] and gas gravity chart method (uses specific gravity of natural gases) [94] to predict hydrate formation/dissociation conditions. These approaches involve simple graphical techniques to estimate HDT and show significant deviations from experiments, especially for specific gravities between 0.9 and 1 [95]. Mixtures having the same specific gravity but different percentage compositions of constituent gases exhibit different equilibrium behavior. This cannot be captured by the specific gravity method; errors of up to 50%

have been reported [96]. The third method involves using empirical correlations containing parameters fitted to experimental data; these have been mainly used to predict hydrate forming conditions for sweet natural gases [97]–[101]. The fourth method involves statistical thermodynamics-based modeling approaches. The first such model developed in 1959, known as Van der Waals and Platteeuw (vdW-P) model, was based on a modification of classical adsorption statistical mechanics using Lennard-Jones potential function to calculate dissociation pressure for pure gas hydrates [102]. Parrish and Prausnitz [103] extended this methodology for single and multicomponent gas hydrates by using this model along with the Kihara potential function to describe gas-water interactions. Several studies have used the vdW-P model coupled with various equations of state to calculate equilibrium conditions for gas hydrates in the presence of electrolytes and alcohols [104]–[112]. Such thermodynamic models used to characterize hydrate formation require detailed knowledge of the underlying complex processes leading to hydrate formation. It is noted that there are significant challenges associated with such thermodynamic models that try to capture the physics underlying hydrate formation using macroscopic constructs, whereas hydrate formation events occur at a molecular level [113].

With the advent of computing technologies, a fifth method based on machine learning approaches has rapidly gained traction. Machine learning (ML) is increasingly being used to predict the behavior of complex non-linear systems in fields ranging from finance, medicine, geology, sensors etc. [114]–[116]. ML algorithms, which are a subset of artificial intelligence, can predict performance and discern patterns characterizing a system by learning from data. They can also be used to model complex systems and automate analytical model building. Multiple machine learning algorithms such as neural

networks, decision trees, and support vector machines have been recently studied to predict dissociation/formation conditions of hydrates as detailed ahead.

The first study (in 1998) on this topic employed neural networks to predict hydrate dissociation conditions [117]. Four models employing different input features such as gas specific gravity and composition of hydrocarbons and inhibitors were studied using Artificial Neural Networks (ANN) [117]. Since then, multiple neural network based-studies employing specific gravity of the gas and either the pressure or temperature as the input variable have been used to predict hydrate forming conditions [118], [119]. It is noted that the use of specific gravity as a variable results in loss of information on the gas composition. Gas composition has therefore been used as the input feature in a majority of ML-based prediction studies [120]–[125]. Hamidreza and Mohammad employed Extremely Randomized trees and Least square support vector machines (LSSVM) on a database of more than 1840 experimental data points and achieved good predictions with an R^2 accuracy greater than 96% [123]. LSSVM and Gradient Boosted Regression trees have been employed in other studies to predict hydrate dissociation conditions with good accuracy [122], [124], [125].

Most of the studies evaluating the performance of ML algorithms in evaluating hydrate dissociation temperature (HDT) so far use either percentage composition of gases and total pressure as features to train the algorithm. Exceptions include a few studies which have used either specific gravity [126] or electrical conductivity [127] of the aqueous solution as features. While models using percentage composition of gases and total pressure as features report good prediction capability, this approach makes it challenging to quantify the contribution of individual gases (in a mixture) towards hydrate formation. As an illustration, the same total pressure can be achieved for a 30% CO_2: 70% CH_4 mixture and a 70% CO_2: 30% CH_4 mixture (composition in molar

volumes). In such cases, the total pressure feature in itself is of limited use in identifying the relative contribution of gases. The model would then primarily rely on the percentage composition of individual gases to predict the HDT. Furthermore, the contribution of inhibitors such as salts is captured via their individual weight percentage or molality term. From a chemistry standpoint, the inhibition action of salts depends on more fundamental factors such as the ionic strength of the solution, salt-water interactions etc. which cannot be captured via a simple weight percentage term. Since ML models are data driven, the capability to predict HDT is highly contingent on the availability of experimental data for a particular salt or a combination of salts. As an illustration, the inhibiting influence of NaCl has been more widely studied than that of KCl, $CaCl_2$ or $MgCl_2$. This makes the database employed in prior studies using weight percentage of individual salts highly skewed towards prediction of NaCl-based inhibition.

1.2 OBJECTIVES OF RESEARCH FOR THIS DISSERTATION

The strategic goal of this dissertation is to explore novel pathways leading to enhancement of hydrate nucleation kinetics and establish novel methods (experimental + ML techniques rooted in fundamental chemical thermodynamics) for prediction of hydrate equilibrium conditions. In addition to studying fundamentals, the goal is also to evaluate the practical utility of using hydrates in a real-world application. Therefore, the techno-economic factors and constraints involved in using CO_2 hydrates for carbon capture and sequestration (CCS) of CO_2 coming out as a byproduct of steam methane reforming of landfill gas in Texas has been analyzed. The proposed research program is organized around three primary objectives, as discussed below.

Objective 1 (Nucleation kinetics-related): Investigate the role of electric field and surface chemistry in accelerating nucleation of THF (miscible liquid-liquid system) and CO_2 (gas-liquid system) hydrates

Subtask 1

Induction times for THF hydrate nucleation upon the application of low-voltage electric fields using open-cell aluminum foam as electronucleation electrodes have been evaluated as a part of subtask 1.

Fundamental questions addressed in subtask 1 of Objective 1 are:

- Do open-cell metal foams help reduce induction times compared to bare stainless steel rods when used as electronucleation electrodes?
- Can the hydrate conversion time be reduced by using metal foams (that aid in increasing the effective thermal conductivity of the THF-water solution)? If so, how quickly does hydrate conversion happen when compared to using bare stainless- steel electrodes?
- Is the electronucleation of THF hydrate dependent on the polarity of the foam electrode?
- If nucleation promotion is polarity-dependent, what are the fundamental electrochemistry-related mechanisms underlying polarity-dependent electronucleation?

Subtask 2

Nucleation promotion of CO_2 hydrates on commonly used metallic surfaces such as Al, Cu, and stainless steel has been studied as part of subtask 2.

Fundamental questions addressed in subtask 2 of Objective 1 are:

- Does surface chemistry influence the nucleation of CO_2 hydrates?

- What is the extent of nucleation promotion by aluminum?
- Can the nucleation promoting effect of Al be replicated by salts of aluminum such as $AlCl_3$, $Al_2(SO_4)_3$?
- Is the promoting effect of Al surface replicable with salt water?
- What is the effect of increased dissolution time (higher amount of dissolved CO_2 in liquid) on nucleation of CO_2 hydrates?
- Is it possible to pinpoint the origin of the nucleation site (solid-water, gas-water, or gas-solid-water interface)?

<u>Objective 2 (Thermodynamics-related)</u>: Investigate thermodynamic inhibition effect of amino acids on CO_2 hydrates using droplets-based system and develop machine learning tools to predict thermodynamic conditions for gas hydrate formation

<u>Subtask 1</u>

Individual droplets on Al surfaces have been used to evaluate the thermodynamic phase equilibrium (p-T) conditions for CO_2 hydrate formation.

Fundamental questions addressed in subtask 1 of Objective 2 are:

- Does Al metal influence the thermodynamics of CO_2 hydrate formation?
- Do amino acids influence nucleation kinetics for CO_2 hydrates?
- What is the average depression in freezing point temperature that can be obtained using amino acids?
- Is the inhibition behavior dependent on the side chain properties for amino acids?

<u>Subtask 2</u>

Machine learning models (using thermodynamically consistent variables as input features in the algorithm) have been trained, and their performance has been evaluated on an extensive experimental database consisting of more than 1800 data points.

Fundamental questions addressed in subtask 2 of Objective 2 are:

- What fundamental thermodynamic variables related to hydrate formation/dissociation could be used as features in ML algorithms?
- Can ML algorithms capture the inhibition effect of salts containing monovalent as well as divalent ions?
- Does the use of newly introduced ML algorithms such as extreme gradient boosting (XGBoost) lead to a significant improvement in the prediction of hydrate dissociation temperature when compared to conventional tree-based methods?
- What are the drawbacks of using machine learning for the prediction of hydrate phase equilibrium conditions?

Objective 3 (application of CO_2 hydrates): Conduct feasibility analysis and investigate the techno-economic factors associated with the use of gas hydrates for capturing CO_2 generated by steam reforming of landfill gas (LFG) in Texas

Fundamental and techno-economic questions addressed in Objective 3 are:

- What would be the costs involved in producing H_2 via steam methane reforming of landfill gas across various counties in Texas?
- What would be the water and electricity requirements (compression and refrigeration) for a production facility used for capturing CO_2 as gas hydrates?
- What would be the capital + operating costs (itemized cost estimation) involved in setting up gas hydrates-based carbon capture facilities across Texas?
- Would adding a thermodynamic promoter such as TBAB (that decreases/increases hydrate forming pressure/temperature) decrease the overall cost required to capture one metric ton of CO_2?

- What would be the net present value and payback period for a project which involves coupled SMR+hydrates-based carbon capture system?

1.3 ORGANIZATION OF THE REST OF DISSERTATION

This dissertation is divided into seven chapters. Chapters 2-6 detail the studies related to the above three objectives. The work presented in Chapters 2-4 is experimental in nature and contains a description of the experimental setup, procedures, analysis and discussion of the results. Chapter 5 provides a brief description of the machine learning techniques, development of the ML models, procedure and discussion of the prediction results. Chapter 6 outlines the technical details related to steam methane reforming procedure to generate H_2 and CO_2, the thermodynamics associated with the compression and cooling process to capture CO_2 as hydrates, data collection procedure for the landfills in Texas, and economic analysis for hydrates-based carbon capture. Chapter 7 summarizes the conclusions and advancements from the present work and outlines suggestions for future work. Appendix A provides supporting information for droplet nucleation experiments presented in Chapter 3. Appendix B to I include brief summaries of other complementary research (carried out during the Ph.D. program) that have been published as journal and conference articles.

Chapter 2: Electronucleation of Tetrahydrofuran hydrates using metal foam-based electrodes[2]

This chapter describes findings from a study on electronucleation of tetrahydrofuran (THF) hydrates, wherein the induction time for the nucleation of hydrates is significantly reduced. Electronucleation involves applying an electrical potential difference across the hydrate precursor solution. This study demonstrates that open-cell aluminum foam electrodes can reduce the electronucleation induction time by more than 150X when compared to non-foam (bare stainless steel) electrodes. Experiments with THF hydrates revealed that aluminum foam electrodes trigger near-instantaneous nucleation (in only tens of seconds) at voltages as low as 20V which is a significant advancement from previous findings [54]. The enhancement in nucleation kinetics can be attributed to two distinct interfacial mechanisms at the electrode-liquid interface, namely electrolytic bubble generation and the formation of metal ion complex-based coordination compounds. These mechanisms (which depend on the electrode material and polarity) affect the induction time to vastly different extents. Coordination compound-based complexes (verified via detection of metal ions in solution) exerts a much greater influence on electronucleation than the mechanistic effects associated with bubble generation. Overall, this work uncovers the benefits of using foams to promote electronucleation and shows that foams lead to more deterministic (as opposed to stochastic) nucleation when compared with non-foam electrodes.

[2] The contents of this chapter have been published in the following journal article: Shahriari, A., Acharya, P.V., Carpenter, K. and Bahadur, V., 2017. Metal-foam-based ultrafast electronucleation of hydrates at low voltages. *Langmuir*, *33*(23), pp.5652-5656. (https://pubs.acs.org/doi/10.1021/acs.langmuir.7b00913); further permission related to the material excerpted should be directed to the ACS. P.V.A. performed research, conducted experiments and analyzed data.

2.1 EXPERIMENTAL PROCEDURE

Electronucleation of tetrahydrofuran (THF) hydrates was studied in this work. It is noted that THF hydrates are commonly used as a model for methane hydrates [80], [128]–[131], which are challenging to study since they require high-pressure conditions (>350 atmospheres at 25 ^{o}C) to form. THF (C_4H_8O) forms structure II hydrates [59] from a THF-water mixture (stoichiometric molar ratio of THF:water is 1:17) at atmospheric pressure and below 4.4 °C. In this work, there was an excess of THF to prevent ice formation, and the ratio of THF to water was selected as 1:15.

Figures 2.1(a-b) show a schematic depiction of the experimental setup. All experiments were conducted in a water/glycol-based cold bath. THF electronucleation was studied in glass tubes (inner diameter: 14 mm, length: 95 mm) fitted with a rubber stopper. The stopper also held the two electrodes and a thermocouple (Figure 2.1(b)). A T-type ungrounded thermocouple was used to detect electronucleation; this type of thermocouple prevents the applied voltage from influencing temperature measurements.

Open-cell aluminum foams with a porosity of 92% and a surface area-to-volume of 1720 m^2/m^3 were used in this study. A 6 mm x 8 mm x 50 mm sized foam plug was used as one of the electrodes, as shown in Figure 2.1(b). A stainless-steel electrode (diameter: 1.6 mm) was used as the other electrode and can be considered inert compared to the more electrochemically active aluminum electrode. The spacing between the electrodes and the thermocouple was approximately 5 mm. The electrodes were connected to a DC power supply (Kepco) and an ammeter (Keithley). Additionally, baseline electronucleation experiments were conducted with two stainless steel electrodes, i.e. without any foam electrode.

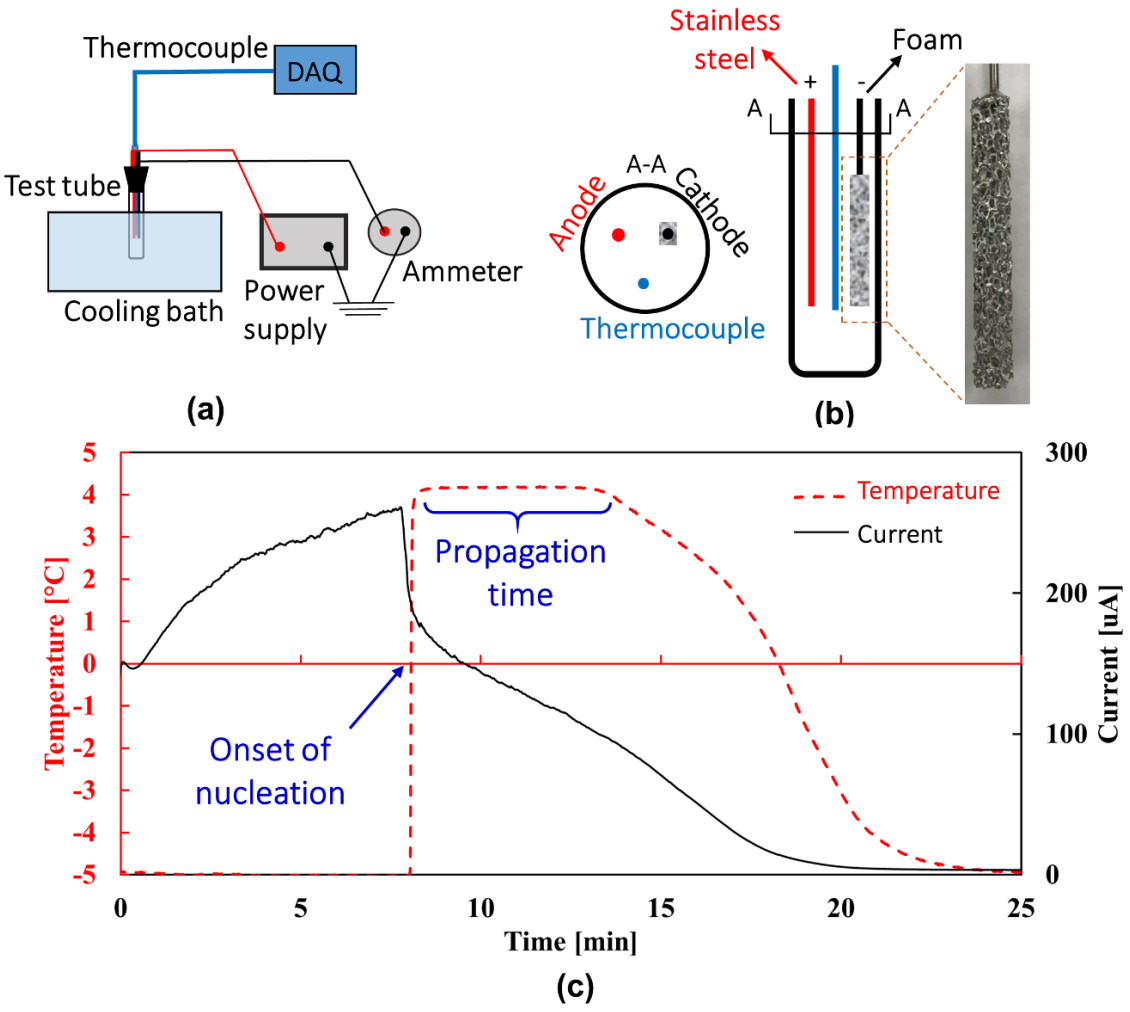

Figure 2.1 (a) Experimental setup, (b) Stainless steel and aluminum foam electrodes inside the tube (right image shows the foam electrode), and c) detection of nucleation by tracking the thermal signature and current flow in the hydrate precursor solution.

A single tube was used in every experimental run to avoid the possibility of nucleation in one tube influencing any other surrounding tubes in the cooling bath. To eliminate the possibility of contamination, all electrodes, the thermocouple and the glass tube were cleaned after every single experiment. The electrodes, thermocouple and the tube underwent three separate ultrasonication treatments, each lasting for 10 minutes,

with the tube filled with acetone, isopropyl alcohol, and deionized water successively. The electrodes, thermocouples and test tubes were dried and kept in a vacuum desiccator until the following experiment. The tube contained 8.77 ml of THF hydrate precursor solution (water-THF mixture), which was agitated (to ensure complete mixing) and degassed to remove air bubbles (which can act as potential nucleation sites). The tube was then immersed in the cooling bath set at 5 °C. After the tube reached 5 °C, the bath temperature was lowered to -5 °C. Once the water-THF mixture was supercooled to a steady temperature of -5 °C, an electrical voltage (5, 10 or 20 V DC) was applied. The induction time was measured starting from this point onwards to the time when hydrate nucleation was detected.

Electronucleation was detected by tracking the thermal signature of the solution [54]. The heat released at the onset of nucleation (recalescence) instantaneously raises the temperature of the entire solution to ~ 4 °C (Figure 2.1(c)). This also confirms that a THF hydrate is being formed and not ice, which would have otherwise led to a temperature spike to 0 °C. The second indicator [54] of hydrate nucleation is a sudden decrease in the electrical conductivity of the solution (Figure 2.1(c)). It is noted that other researchers have also used these methods to infer the nucleation of THF hydrates [59] and ice [132], [133]. Notably, the magnitude of Joule heating is very low, and its influence is neglected. The maximum current in all these experiments was 86 μA, 211 μA and 803 μA at 5, 10 and 20V, respectively; this translates to less than 16 milliwatts (at 20 V) of heat generation. Also, the temperature increase to 4 °C indicates hydrate formation and confirms that ice is not being formed (in which case the temperature spike would have been to 0 °C).

2.2 RESULTS

Figure 2.2 shows the measured induction times as a function of the voltage for the baseline (non-foam) case and the cases with the aluminum foam electrode acting as the cathode and anode. Each data point is the average of more than five measurements. The baseline case (with stainless steel electrodes) shows a voltage-dependent reduction in the induction time, in line with a previous study investigating the electronucleation of THF hydrates [54]. The use of aluminum foam as the cathode (negative polarity electrode) significantly reduces the induction time, as evident from the 10X decrease at 20 V. This clearly highlights the benefits of foams, with the high surface area associated with the porous foams aiding nucleation. In this work, the porosity of the aluminum foam resulted in a 17X enhancement in the surface area compared to the bare electrode.

The induction time is further reduced dramatically by switching the polarity to make the foam electrode as the anode (positive polarity electrode). Figure 2.2 shows that the induction time is reduced by ~40X (at 5V) when compared to the same foam used as the cathode. The average induction times at 10 V and 20 V, with the foam anode, were only 43 seconds and 20 seconds, respectively, which reflects a substantial acceleration in nucleation kinetics when compared with the numbers reported in a previous related work [54] (nucleation time of 7 minutes at 100 V). Positively biased aluminum electrodes can thus enable instantaneous nucleation, which can benefit the development of applications that need ‘hydrates on demand’. It is noted that no nucleation was observed in any experiment at 0 V even after twelve hours. Overall, these results suggest that aluminum foams with the appropriate polarity can enable a two-order of magnitude reduction in induction time compared to non-foam inert electrodes. As an illustration, the induction time decreases by 150X at 5 V when an inert stainless steel electrode is replaced with an aluminum foam electrode as the anode.

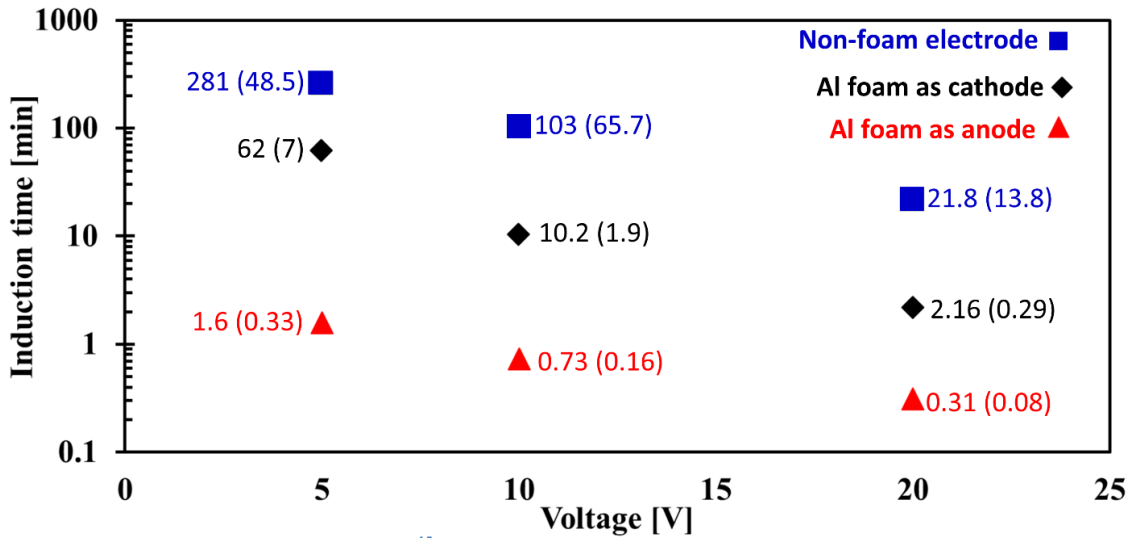

Figure 2.2 Voltage-dependent electronucleation induction times for the baseline (non-foam, inert electrode) case and the cases where the aluminum foam was the cathode and anode. The numbers next to the data points indicate the average and standard deviation (in parenthesis) in the measurements.

An interesting observation from Figure 2.2 is that the spread in the measurements is significantly reduced in the foam experiments, especially at higher voltages. The standard deviations in the induction time measurements for the non-foam experiments are ~ 60% of the mean value for experiments at 10 and 20 V. The corresponding standard deviations with the use of foam electrodes (either as cathode or anode) are reduced to 13-25% of the mean value. This suggests that the use of foams can suppress the inherent stochastic nature of nucleation and transform nucleation to a more deterministic phenomenon.

The influence of polarity is very remarkable, with the induction time reduced by factors of 40, 14, and 7 at 5, 10, and 20V, respectively, by switching the foam polarity from negative to positive. This also suggests that multiple physical phenomena are likely at play. One electronucleation mechanism briefly mentioned in a previous study [54] was bubble generation at the electrodes, resulting from hydrolysis reactions. These bubbles

can act as nucleation sites. Furthermore, the convection currents associated with bubble growth and detachment can assist in triggering nucleation. Bubble generation on the foam electrode was indeed observed, as detailed below. However, this mechanism alone cannot explain the polarity-dependent induction time.

This study identifies and proves the existence of another mechanism, which affects nucleation more profoundly than bubble-related effects, and is polarity dependent. This mechanism can be understood by examining the results of Hozumi et al. [134] and Shichiri and Nagata [35], who conducted experimental studies to determine the influence of electrode material on the electric field-induced freezing of pure water. Freezing was enhanced [134] with aluminum electrodes, as compared to more inert materials (platinum, gold). It was hypothesized [134] that this enhancement is due to the formation of aluminum-based coordination compounds at the electrodes, the structure of which resembles the crystal structure of ice [134]. The existence of a similar mechanism is analyzed in this work to explain the accelerated hydrate formation with aluminum foam as the anode.

Both the above mechanisms (bubble generation, coordination compound formation) can be further understood by considering the chemical reactions taking place at the electrodes. For the case of the foam electrode as the cathode, water is reduced to hydroxyl ions, and hydrogen gas is generated (Figure 2.3a), which accounts for the bubbles ($4H_2O + 4e^- \rightarrow 4OH^- + 2H_2 \uparrow$) observed at the cathode. The high surface area of the foam, and the presence of surface irregularities, provide a large number of nucleation sites for gas bubble generation, which explains the faster electronucleation as compared to the non-foam electrode. At the anode (stainless steel), the hydroxyl ions are oxidized to generate oxygen ($4OH^- \rightarrow O_2 \uparrow + 2H_2O + 4e^-$). Furthermore, stoichiometric calculations

indicate that less than 0.001% of the water is electrolyzed; this will not change the composition of the hydrate-forming mixture.

Polarity-dependent nucleation can be explained by a different reaction occurring at the foam when it is the anode. In this case, the oxidation of aluminum is favored [134] over the oxidation of hydroxyl ions due to the high ionization tendency of aluminum ($Al \rightarrow Al^{3+} + 3e^-$). Al^{3+} ions therefore enter the solution and are surrounded by water molecules to form a hydroxo-aquo-aluminum coordination compound $[Al(H_2O)_6]^{3+}$ (Figure 2.3b). Furthermore, OH^- ions form bridges between the coordination compounds leading to the synthesis of an octahedral polynuclear complex [134]. We hypothesize that the structured ordering of water molecules due to the presence of such coordination compounds that act as seeds for hydrate formation promotes nucleation.

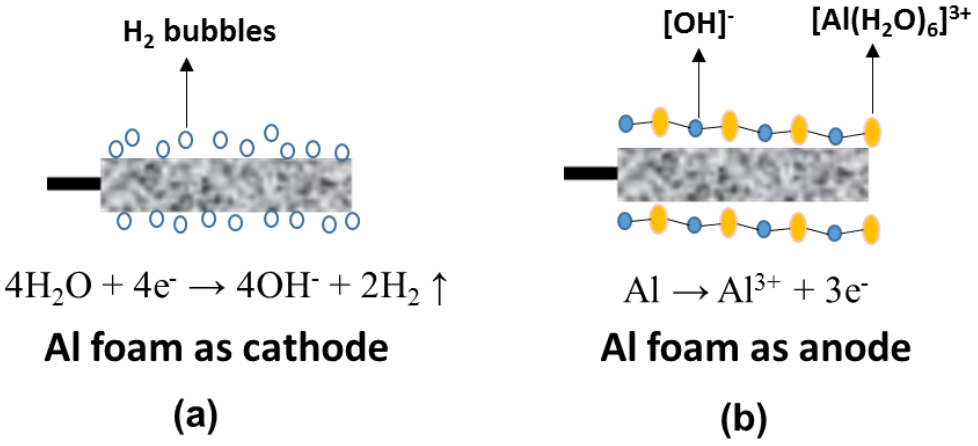

Figure 2.3 Schematic depiction of mechanisms underlying electronucleation (a) Bubble-related effects when aluminum foam is the cathode (b) Coordination compound formation-based nucleation when aluminum foam is the anode.

The bubble formation hypothesis was validated by high magnification visualization of bubble activity in the foam electrode during electronucleation. Figure 2.4

shows the aluminum foam electrode as the cathode and the anode in separate experiments. When the foam is the cathode (Figure 2.4a), significant bubble generation and departures are seen on the foam surface, as depicted in Figure 2.4a. Mechanistic effects associated with bubble growth and detachment, such as contact line motion, localized fluid convection etc., can provide the activation energy to trigger nucleation.

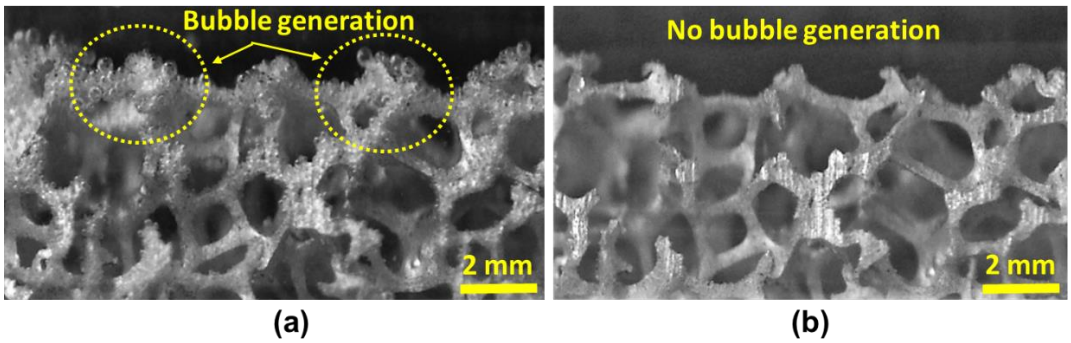

Figure 2.4 Aluminum foams acting as the (a) cathode, which leads to significant bubble generation, and (b) anode, where no bubble generation is observed.

In contrast, negligible bubble generation is observed when the foam is the anode (Figure 2.4b). This indicates that an alternative electrochemical reaction (oxidation of aluminum to form coordination compounds) occurs at the foam anode and is responsible for nucleation promotion. While it is challenging to detect the formation of coordination compounds at the interface experimentally, this work successfully detected the presence of Al^{3+} ions in solution, which are the precursors to the Al-based coordination compounds.

The current-time plot (Figure 2.1c) can be used to estimate the concentration of Al^{3+} ions in the present experiments by estimating the total charge transfer in the solution till the onset of nucleation. These calculations indicate that the concentrations of Al^{3+} ions will be (O) 10^{-6} mol/liter at the onset of nucleation. The $[Al(H_2O)_6]^{3+}$ concentrations from

such low concentrations of Al^{3+} ions could be challenging to detect with conventional spectroscopic studies [135]–[137] and was not attempted.

In this work, a colorimetric indicator reaction was used to prove that Al^{3+} ions enter the solution when the foam is the anode. Subsequent solvation of these ions leads to the formation of $[Al(H_2O)_6]^{3+}$ based coordination compounds. Pyrocatechol Violet (PV) is commonly used as a complexometric indicator dye to detect the presence of Group III cations [138], [139]. As it chelates metals, it forms a blue-violet-colored coordination compound. In this work, PV was used to detect Al^{3+} ions in solution to partly validate our hypothesis that aluminum ions leave the foam electrode (when it is the anode) to form coordination compounds, which accelerates the nucleation of hydrates.

Figure 2.5 shows the aluminum foam electrode as the cathode and the anode in separate electronucleation experiments where 0.2 mM PV is dissolved in the solution. When the foam is the cathode (Figure 2.5a), no color change is observed; instead, there is bubble formation, which will also accelerate nucleation. However, when the foam is the anode (Figure 2.5b), the color of the solution changes to violet-blue starting from the foam as the PV chelates aluminum ions.

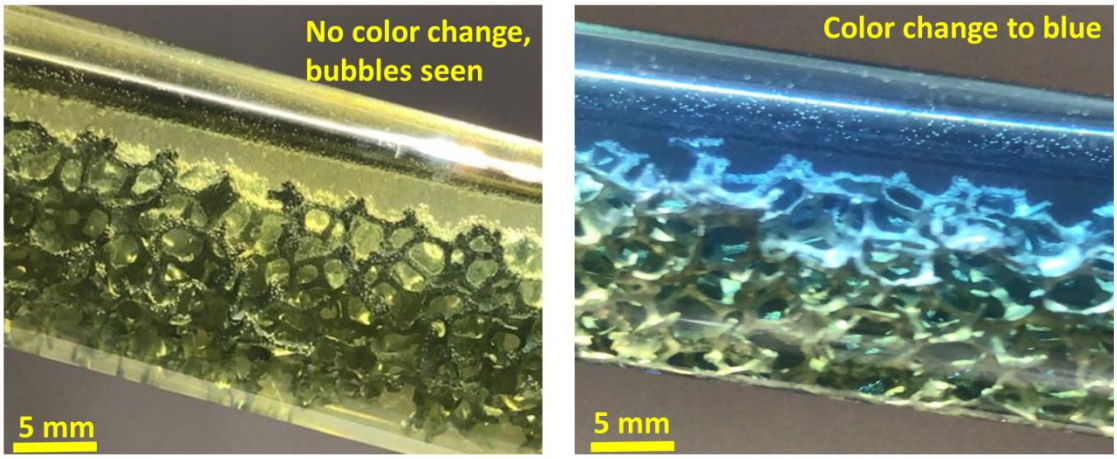

Figure 2.5 Bubble generation (a) is seen with the foam electrode as the cathode. However, aluminum ions in solution are detected via a color change (b) due to chelation, which indicates that aluminum-based coordination compounds are formed when the foam electrode is the anode.

The above experiments offer compelling evidence to attribute accelerated hydrate nucleation to the formation of aluminum-based coordination compounds in the absence of bubbles. Furthermore, induction time measurements indicate that the coordination compound formation mechanism influences nucleation more strongly than bubble-related mechanistic effects.

2.3 Discussions

It is important to note that metal foams also accelerate the rate at which the hydrate formation front progresses, in addition to promoting electronucleation. This can be attributed to the higher thermal conductivity of the aluminum foam-precursor solution network (12 W/mK), as opposed to the conductivity of the precursor solution alone (0.6 W/mK). The effective thermal conductivity of a metal foam ($k_{effective}$) in a liquid solution can be estimated using the following equation [140]:

$$k_{effective} = k_{Al}\left[\frac{2+\frac{k_{sol}}{k_{Al}}-2\phi\left(1-\frac{k_{sol}}{k_{Al}}\right)}{2+\frac{k_{sol}}{k_{Al}}+\phi\left(1-\frac{k_{sol}}{k_{Al}}\right)}\right] \quad (2.1)$$

In the above equation, k_{Al} is the thermal conductivity of aluminum (205 W/mK), k_{sol} is the thermal conductivity of the THF/water solution (~ 0.6 W/mK) and ϕ is the porosity of the foam (0.92).

Higher thermal conductivity aids removal of the heat generated during hydrate formation. In this work, the decreased time for hydrate formation was quantified by measuring the phase change propagation time, which is the time taken since the onset of nucleation to convert the entire tube to a hydrate plug. This time can be inferred from the temperature-time curve in Figure 2.1c and is summarized for various cases in Table 2.1. Firstly, it is seen that the propagation time for the -5 °C experiments is reduced from 7.5 minutes in the absence of foams (non-foam electrodes used) to 5.1 minutes with the foam (average of 5 experiments each with the foam as the cathode and anode). Importantly, it was seen that the foam polarity and the magnitude of the applied voltage did not measurably influence the propagation time. Repeating the experiments at -10 °C shows that the propagation time is reduced from 4.8 minutes to 1.9 minutes upon using foams. The -10 °C experiment was carried out without voltages since the additional supercooling ensures nucleation with low induction times. It is noted that that hydrate formation rates are determined by all the pathways available to reject the generated heat, and the present results apply only to this particular geometry. Nevertheless, it is clear that the heat

transfer benefits and the electronucleation promotion associated with foams will assist in the synthesis of hydrates.

Table 2.1 Time taken for hydrates to form in the entire tube (minutes).

Bath temperature	With foam electrode	Without foam electrode
-5°C	5.1	7.5
-10°C	1.9	4.8

2.4 CONCLUSIONS

In conclusion, the findings presented in this chapter revealed that positively biased aluminum foams enable near-instantaneous low voltage electronucleation of THF hydrates. This study has shown up to a 150X decrease in induction time with foams, as compared to non-foam electrode electronucleation. The underlying promotion effects which depend on the polarity of the foam electrode can be attributed to bubble-based mechanistic effects (cathode) and electrochemistry-based mechanisms (anode), which influence the nucleation kinetics to different extents. This study suggests that foam-based electronucleation can promote rapid hydrate formation (reducing the propagation time at -5 ^{o}C by 32% when compared to bare stainless steel electrodes) without requiring excessive supercooling, which has energy consumption reduction benefits.

Chapter 3: Aluminum-based promotion of nucleation of carbon dioxide hydrates[3]

This chapter investigates the discovery of a simple, passive nucleation promotion technique for gas hydrate systems, wherein *an aluminum surface significantly accelerates nucleation of CO_2 hydrates*. Since such hydrates form under high-pressure, low-temperature conditions, experiments were carried out using a custom-built high-pressure vessel housed in an environmental chamber. Statistically meaningful measurements of induction times for CO_2 hydrate nucleation were undertaken using water droplets as individual micro-systems for hydrate formation. The influence of various metal surfaces, droplet size, CO_2 dissolution time, and the presence of salts in water on nucleation kinetics have been characterized. Interestingly, nucleation initiated only on aluminum surfaces, the influence of which could not be replicated by salts of aluminum. Experiments carried out with cuvettes revealed that nucleation initiated from the Al-water interface in the bulk of the liquid. Nucleation promotion can be ascribed to the chemical reactions occurring at the aluminum-water interface leading to the generation of hydrogen bubbles that likely act as nucleation sites and seed the formation of hydrates.

3.1 EXPERIMENTAL PROCEDURE

Experiments on CO_2 hydrate nucleation were conducted using water droplets in CO_2 ambient in a high-pressure cell. While most studies form hydrates from bulk liquid-gas mixtures, the use of droplets allows conducting multiple experiments in one run. Each droplet acts as an independent system, making it possible to obtain statistically

[3] The contents of this chapter have been published in the following journal article: Acharya, P.V., Kar, A., Shahriari, A., Bhati, A., Mhadeshwar, A. and Bahadur, V., 2020. Aluminum-based promotion of nucleation of carbon dioxide hydrates. *The Journal of Physical Chemistry Letters*, 11(4), pp.1477-1482. P.V.A. conceptualized the work, performed research, designed and built the experimental setup, carried out experiments and analyzed the data.

significant data, bearing in mind that nucleation is stochastic and that hydrate formation experiments are usually very long (half a day). The use of droplets/bubbles to study nucleation and formation of hydrates [141]–[147] and ice [51], [52] is widely employed. This approach also enables high-quality visualization of kinetics and crystal growth.

Figure 3.1 illustrates a schematic and images of the experimental setup. A custom-built, non-stirred, 450 ml pressure vessel (Parr Instruments) with optical sapphire windows was used. The vessel is built to withstand a maximum pressure of 13 MPa at up to 225 ^{o}C. It is equipped with a thermocouple and a pressure transducer connected to a data acquisition system that continuously monitors and logs the temperature and pressure inside the vessel every second. The pressure vessel was placed in an environmental chamber (ESPEC) to cool it down to hydrate formation temperatures. Droplets were monitored with a high-speed camera (Photron Fastcam) fitted with a macro lens (Tokina).

Deionized (DI) water droplets (equal volumes unless specified otherwise) were dispensed on horizontally mounted metal plates in the vessel. In a single experiment, up to three such plates (containing 2-6 droplets each) could be accommodated inside the pressure vessel.

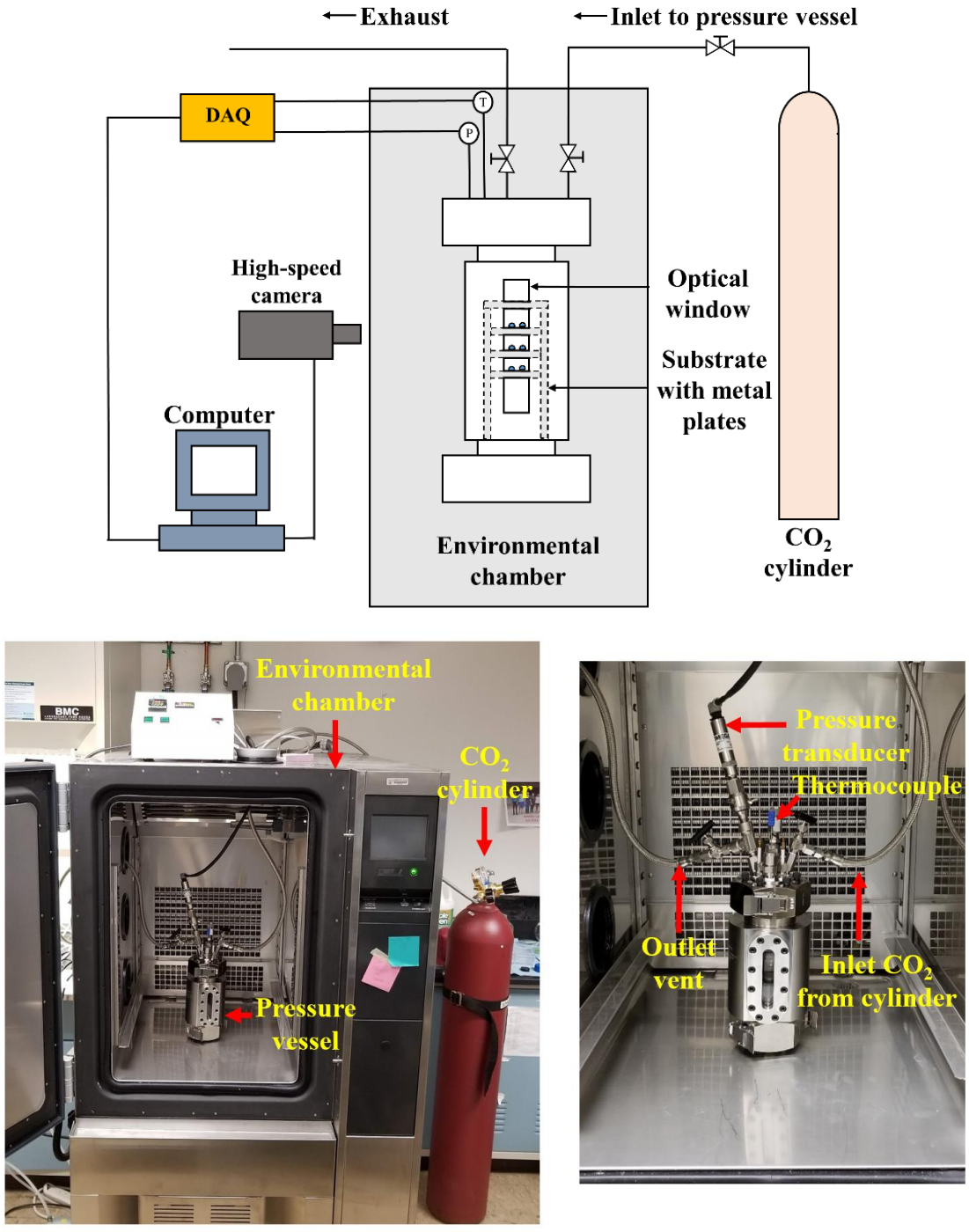

Figure 3.1 Schematic illustration of the experimental setup (top) Images of the pressure vessel housed in an environmental chamber (bottom). Figure reprinted with permission from [148]. Copyright 2020 American Chemical Society.

Four surfaces (dimensions 4.5 x 3 cm) were studied in this work: aluminum, anodized aluminum, copper, and stainless steel (SS). All the metallic surfaces (Al, Cu and SS) had a polished mirror-like texture to minimize the influence of surface roughness on nucleation promotion. The RMS value of the surface roughness for Al, Cu and SS plates were 40, 49 and 61 nm, respectively (surface roughness profiles provided in Fig 3.2). The surfaces were covered to prevent contact with air; the protective covering was removed just before the experiments to minimize contamination and oxide formation. New metal plates and droplets were used for every experiment to avoid the possibility of changes in surface chemistry/morphology and to avoid the memory effect.

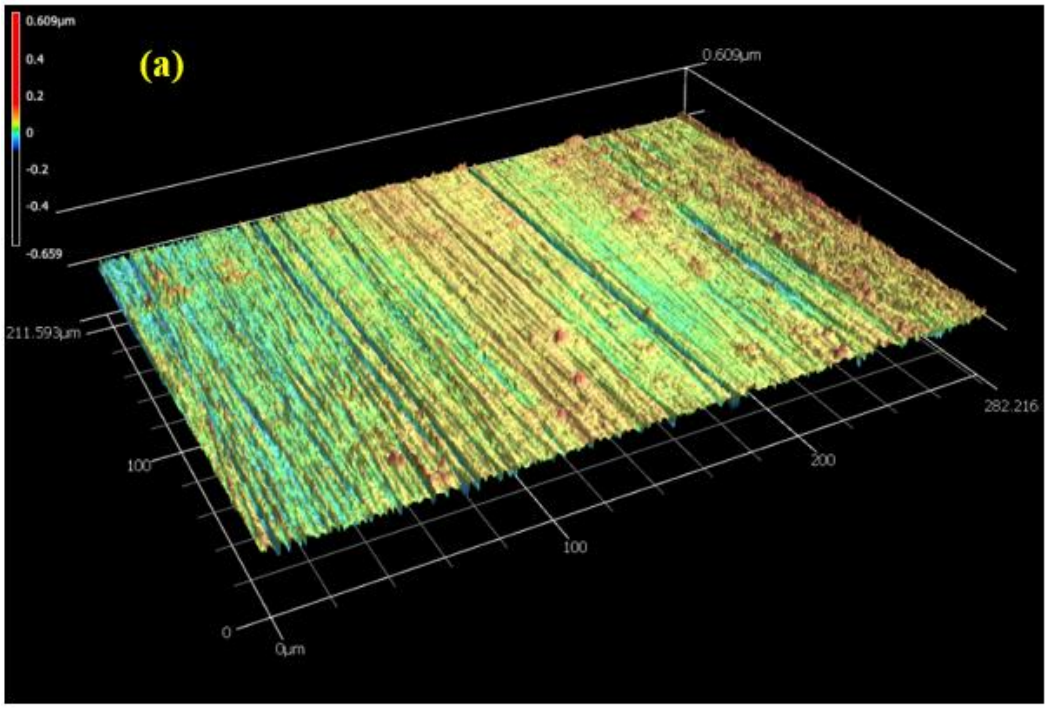

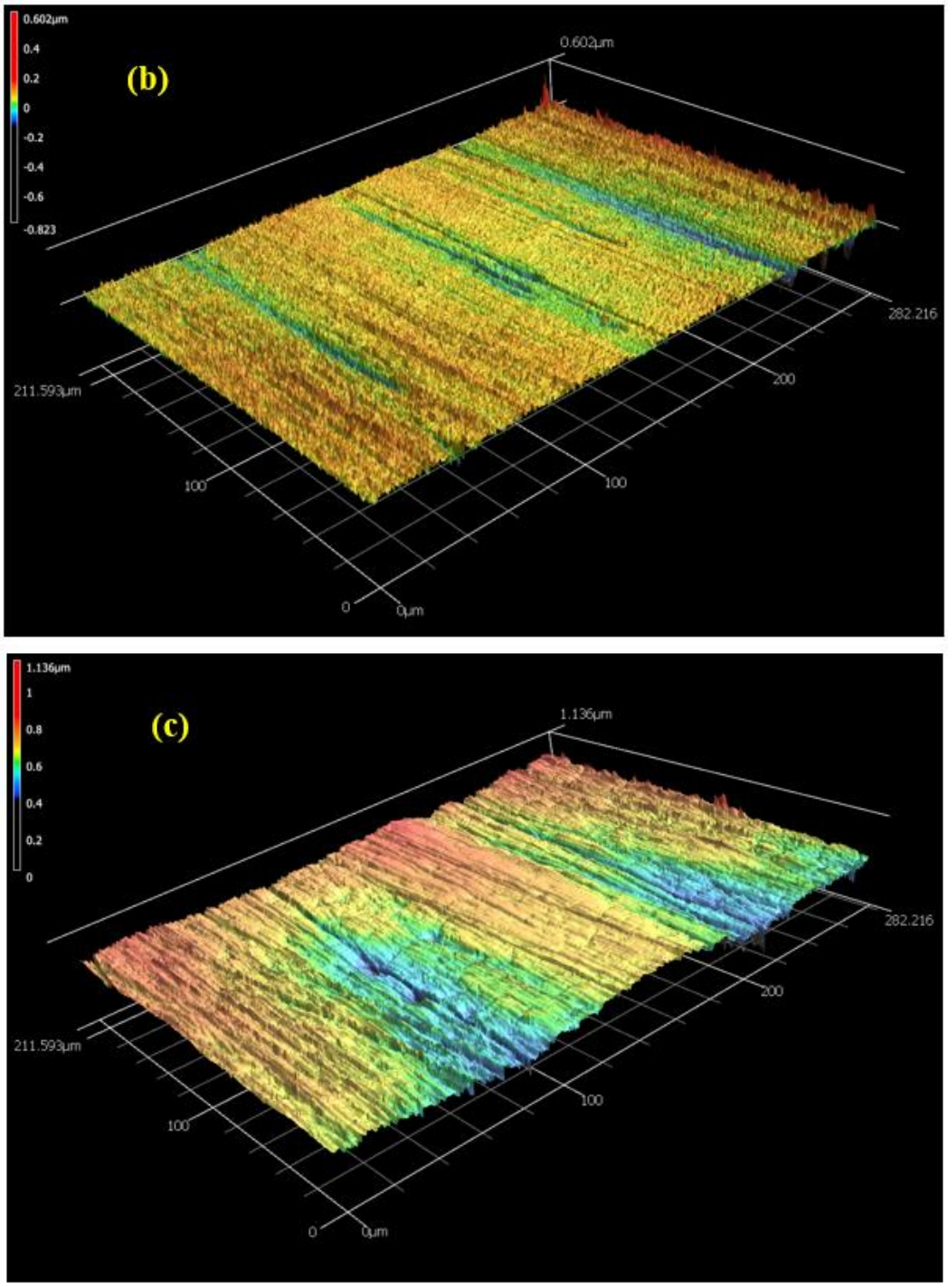

Figure 3.2 Surface roughness profiles for (a) aluminum, (b) copper and (c) stainless steel plates. Figure reprinted with permission from [148]. Copyright 2020 American Chemical Society.

The experimental procedure is detailed ahead. First, the metal surfaces were rinsed with isopropanol (IPA) and DI water, and then successively dried with a burst of N_2 gas. Next, multiple droplets were dispensed with a micropipette on the metal plates at a sufficient distance from each other (a minimum distance of 10 mm) to ensure that a nucleating droplet did not influence its neighbors. The metal surfaces were placed inside the pressure vessel and purged with CO_2 gas for about 60 seconds to remove residual gases in the vessel environment. This was followed by pressurizing the chamber with 99.99% purity CO_2 (3 MPa) at 20 ^oC. The droplets were then allowed to stay in the CO_2 environment for 90 minutes (unless specified otherwise), allowing CO_2 to diffuse into the water. Next, the chamber was isochorically cooled down to 0.5 ^oC to bring the p-T conditions into the hydrate stability region; a temperature higher than 0 ^oC was selected to eliminate the possibility of ice formation. Finally, visualization was turned on, and hydrate nucleation and growth were recorded. All experiments were stopped after all droplets had nucleated or after a duration of 24 hours.

Nucleation was detected via continuous visualization; the droplet turns opaque upon nucleation, and the morphology changes, as clearly seen in Figure 3.3. The induction time is calculated as the time when nucleation occurs after the droplets have entered the thermodynamically stable p-T region for hydrate formation [4].

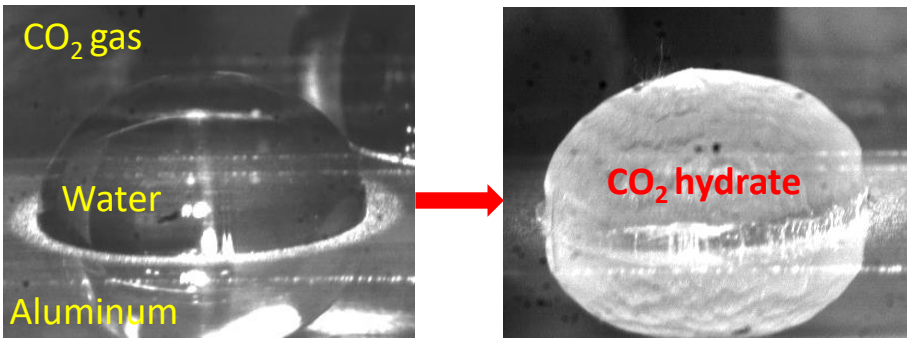

Figure 3.3 Water droplet (left) with a CO_2 dissolution time of 90 mins turn opaque (right) upon conversion to CO_2 hydrate. Figure reprinted with permission from [148]. Copyright 2020 American Chemical Society.

3.2 Results and Discussions

Table 3.1 summarizes the induction time measurements from this work; the reported induction time is the average of at least 25 droplets. In some previous studies [141], [142], the independence of nucleation events is questionable since adjacent droplets were reported to nucleate simultaneously. However, the observed sequence of droplet nucleation in this work was random in a spatial and temporal sense, which shows that the experimental approach did not compromise the stochastic nature of nucleation. The order of nucleation of droplets in the 3-plate configuration is provided in Appendix A.

Table 3.1 Summary of induction time data for various experiments.

Surface	Salt added to DI water	CO_2 dissolution time (mins.)	Droplet volume (µL)	Nucleation rate (min^{-1})	Induction time (mins.)		
					Mean	Std. dev.	Range.
Aluminum 5052	None	90	10	0.0026	494.1	353.6	20-1321
			20	0.0046	296.6	230.7	27-1000
			40	0.0069	194.2	163.7	8-617
		1440	20	0.0027	501.7	402.7	21-1422
	3.5 wt% NaCl	90		0.003	453.1	405.1	8-1567
Stainless steel (T316SS)	None			-	No nucleation	-	
	0.0625-5 wt% $AlCl_3$						
	0.0625-5 wt% $Al_2(SO_4)_3$						
	3.5 wt% NaCl						
Copper	None						
Anodized aluminum	None	90	20		No nucleation		

Key takeaways from Table 3.1 are highlighted ahead. *Firstly, nucleation was observed only on the aluminum surface. No nucleation was ever observed on copper, stainless steel or anodized aluminum surfaces within 24 hours*. Induction times with Al showed a stochastic nature and ranged from 8 minutes to 22 hours, with every droplet eventually nucleating.

Secondly, the *mean induction time decreased, and the nucleation rate increased with increasing droplet volume*. This can be attributed to more nucleation sites becoming available, noting that the three-phase line length and Al-water interfacial area will increase with volume. The similarity between the mean and standard deviation for induction times indicates an underlying exponential distribution. Accordingly, the nucleation rate is evaluated using the following formulation [149]:

$$P(t) = 1 - \exp(-0.693 * J * t) \quad (3.1)$$

In the above equation, J is the nucleation rate, which can be obtained by fitting the above equation to the induction time data obtained from experiments. The probability that a droplet will nucleate in time (t) will be the ratio of the total number of droplets nucleating before time t divided by the total number of droplets in the sample set. By dividing the entire duration into an equal number of time bins, the cumulative nucleation probability for successive times has been obtained as depicted in Figure 3.4 for different droplet volumes (10, 20 and 40 μL). The solid lines represent the fitted equation with nucleation rates of 0.0026, 0.0046 and 0.0069 (min^{-1}) for droplet volumes of 10, 20 and 40 μL, respectively.

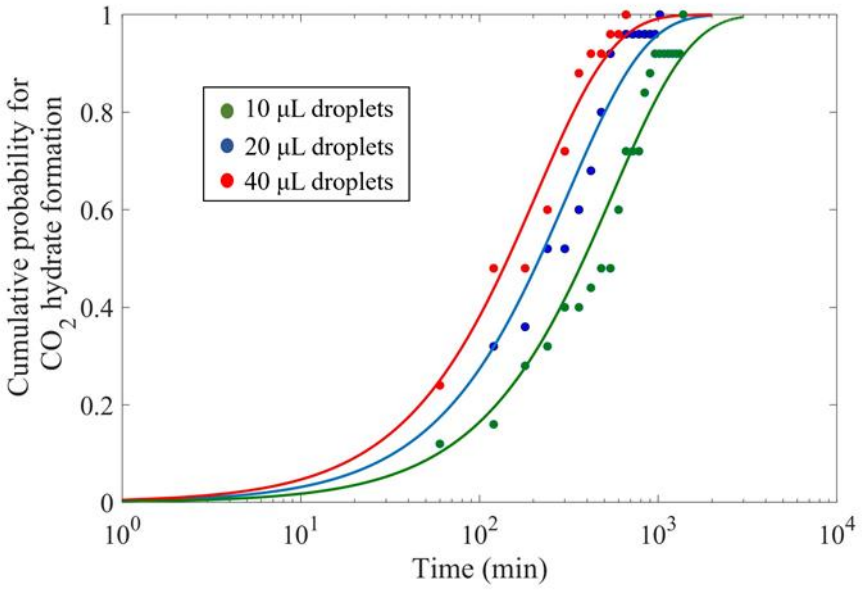

Figure 3.4 Cumulative probability distribution for three different droplet volumes (10, 20 and 40 μL). Figure reprinted with permission from [148]. Copyright 2020 American Chemical Society.

The data on nucleation can be more meaningfully analyzed using a histogram (Figure 3.5), which shows the fraction of droplets nucleating in different time interval bins for three droplet volumes. It is seen that an increase in the metal-droplet interfacial area (due to increasing droplet volumes) leads to more favorable (faster) nucleation trends. This is reflected in a narrower distribution in the fraction of nucleating droplets, which tends to concentrate towards regions of lower induction time intervals. Additional histograms for droplets containing 3.5 wt% NaCl (Figure A.2) and those subjected to a 24-hour dissolution time (Figure A.3) are included in Appendix A.

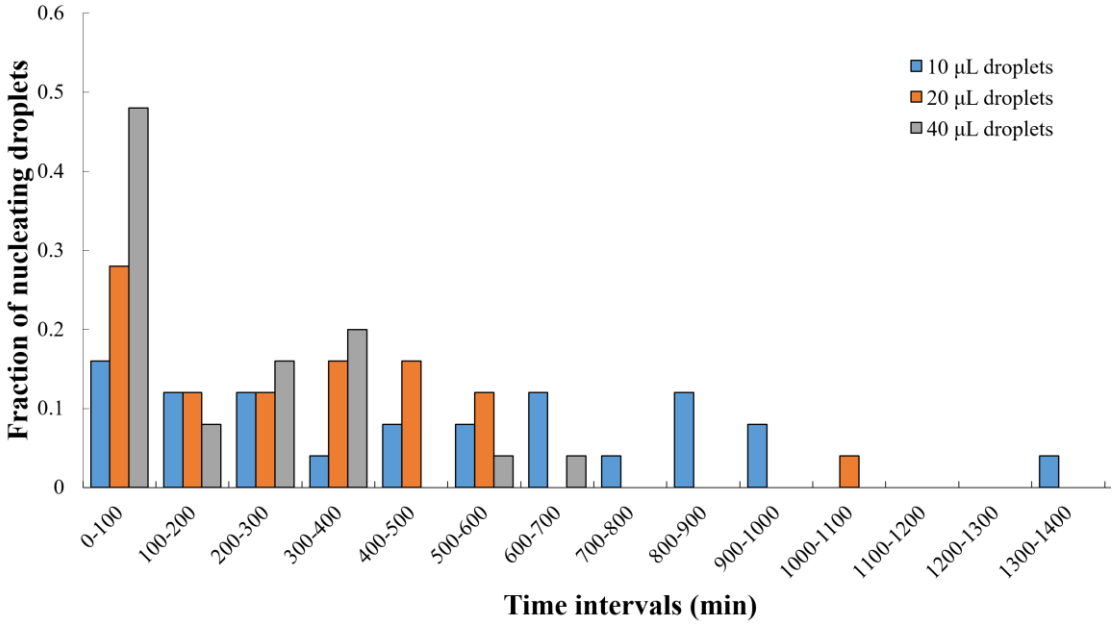

Figure 3.5. Histogram showing fraction of droplets nucleating in various time intervals (grouped using 100-minute bins) for three different droplet volumes (10, 20 and 40 µL) (dissolution time: 90 minutes). Figure reprinted with permission from [148]. Copyright 2020 American Chemical Society.

Thirdly, experiments with water containing 0.6 M sodium chloride (3.5 wt% NaCl, to mimic sea-water concentration) showed a 53% increase in the mean induction time and a 35% reduction in the nucleation rate (20 µL droplets), compared to the results

for DI water. This slower nucleation in the presence of salt is consistent with previous observations [4]. Salt ions in aqueous solutions attract water dipoles via Coulombic bonds (much stronger than hydrogen bonding or van der Waals forces), which reduces the availability of water molecules to form hydrates [4]. Notably, Al surfaces still succeeded in promoting nucleation in saltwater solutions. *This repetition of a previously known phenomenon strengthens the scientific rigor of our approach.*

Another interesting finding of this study concerns the influence of the droplet CO_2 content on the nature of the hydrates formed. Experiments were conducted with water droplets staying in high-pressure CO_2 for 24 hours (instead of 90 minutes) prior to cool-down. This extended time allows the droplet to thoroughly saturate with water (diffusion constant of CO_2 in water [150] at 298 K is 1.92×10^{-9} m^2/s, which implies a mass diffusion length of 25.7 mm in 24 hours vs. 6.4 mm in 90 minutes). While the induction time increased for the higher dissolution time case, the most striking contrast from the 90-minute dissolution time was the morphology of the resulting hydrates. Much more vigorous growth was observed for the 24-hour dissolution time case, with hydrate 'whiskers' seen protruding out of the droplets (Figure 3.6 and Figure A.4 in Appendix A). This can be attributed to higher initial CO_2 concentrations prior to hydrate formation, which enhances diffusion post nucleation, as the CO_2 dissolved in the interior diffuses towards the hydrate shell. Similar whisker-like growth has been observed previously on droplets subjected to a high driving pressure [141].

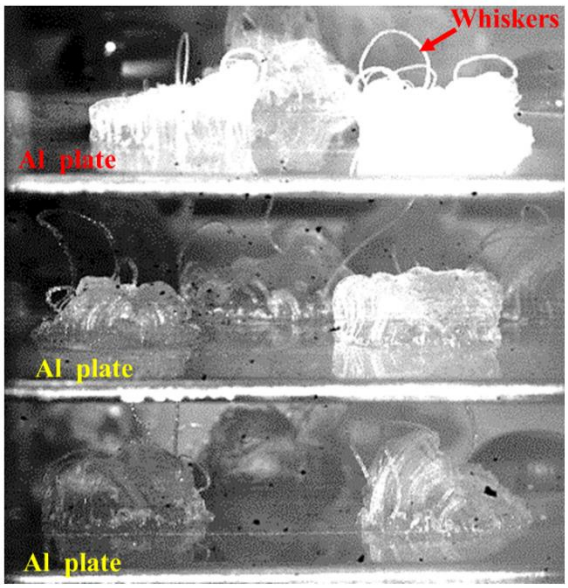

Figure 3.6. CO_2 hydrates (with whiskers) formed from water droplets with a long CO_2 dissolution time (24 hours). Figure reprinted with permission from [148]. Copyright 2020 American Chemical Society.

Another *key finding from our experiments concerns the location of the hydrate nucleation sites*. Previous studies on hydrate formation report [151], [152] that nucleation is triggered at the gas-liquid interface due to higher mole fractions of the guest molecule at the interface (at least two orders of magnitude higher than the bulk phase). In droplet-based nucleation experiments of hydrates [144], [153] and ice [51], [52], nucleation is always observed at the gas-liquid interface or 3-phase line since the nucleation probability is higher than in the other regions of the droplet.

To determine the location of the nucleation sites, experiments were conducted using PMMA Spectrophotometry cuvettes containing 1.75 ml of DI water, with an Al plate dipped as-per two configurations: i) partially submerged longer plate with a 3-phase contact line, and ii) a completely submerged shorter plate without a 3-phase line. Baseline experiments were conducted without any plates and with a stainless-steel plate;

no nucleation was observed. In contrast, nucleation was observed on both configurations of Al plates. Most interestingly, nucleation was always initiated at the Al-water interface (in the interior of the liquid), even for the partially submerged plate configuration (shown in Figure 3.7). This is a very interesting and non-intuitive finding, highlighting the role of the Al-water interface in nucleation promotion.

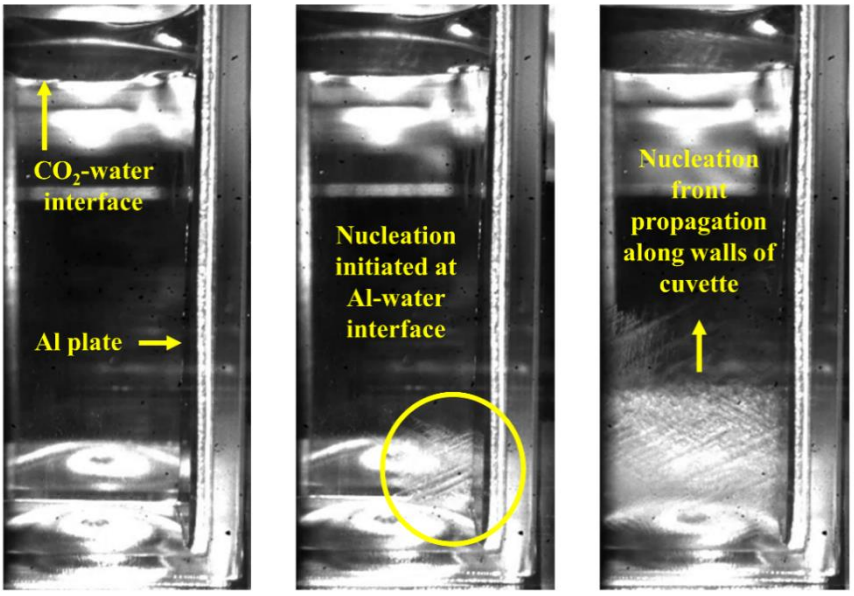

Figure 3.7. Snapshots depicting CO_2 hydrate nucleation at the Al-water interface (left to right). Nucleation originates at the spot, marked in a yellow circle, and proceeds towards the 3-phase line. Figure reprinted with permission from [148]. Copyright 2020 American Chemical Society.

These results clearly highlight the influence of aluminum in 'catalyzing' nucleation in a CO_2-rich water solution, independent of the gas-phase CO_2. This nucleation promotion could be a consequence of bubbles generated due to reactions at the Al-water interface. The line of reasoning for this hypothesis is briefly outlined ahead.

Firstly, post-experiment surface examination shows visible discoloration of the surface. A colorimetric indicator further confirmed the evidence of a surface chemical

reaction. Droplets were imbued with pyrocatechol violet (PV) indicator and placed on an Al substrate. PV is an indicator dye and chelates Al^{3+} ions to form a blue-violet-colored coordination compound. Droplets turned blue shortly after contacting the Al surface, confirming the presence of Al^{3+} ions (Figure A.5. in Appendix A). Previous studies [41], [135] show that solvation of Al^{3+} ions forms Al-based coordination compounds, most notably a hydroxo−aquo−aluminum coordination compound $[Al\text{-}(H_2O)_6]^{3+}$, leading to the synthesis of octahedral polynuclear complexes. It has been theorized (but not experimentally proven) that the resemblance of such structures to the lattice structure of ice [41] and hydrates [154] promotes nucleation.

However, the above hypothesis cannot explain the present results. Experiments were conducted (Table 3.1) with two Al salts ($Al_2(SO_4)_3$ and $AlCl_3$) dissolved in water in varying weight concentrations (0.0625, 0125, 0.25, 0.5 and 5 wt%). Both salts produce Al^{3+} ions in water. These experiments were conducted on inert stainless steel to ensure the absence of surface-related nucleation. No nucleation was observed in any experiments, despite the presence of Al^{3+} ions.

The nucleation-promoting Al plates have a 2-10 nm [155] thick native oxide layer. Such oxide layers are porous, hydrophilic, and can be broken down by the weakly acidic solution (carbonic acid formed in the CO_2-water environment), thereby resulting in Al-water contact. Further insights emerge from similar experiments conducted on Al surfaces with thicker oxide layers (anodized aluminum with 25 μm thick oxide layer, deposited via electrolytic oxidation). Interestingly, no nucleation was observed (Table 3.1) on such surfaces. Although anodized Al is porous on the outside, it is not porous throughout the oxide layer and prevents water contact with the Al surface. The absence of nucleation on anodized Al suggests that Al-water contact is necessary for nucleation.

It is possible that the cause of nucleation promotion is not directly related to the ionic species generated at the interface. Instead, hydrogen (H_2) bubble generation at the surface is likely responsible for nucleation. It has been reported that hydrogen nano-bubbles form at the surface of a platinum electrode; the resulting high Laplace pressure generated due to the small radii leads to favorable conditions for the formation of hydrogen hydrates [156]. Bubbles have also been reported to assist the nucleation of tetrahydrofuran hydrates in similar studies conducted in the past [54], [154]. Presently, Al reacting with carbonic acid/water will lead to the generation of H_2 bubbles, which seed the nucleation of CO_2 hydrates. Carbonic acid will also assist in breaking down any thin or native oxide layers to promote Al-water contact. This hypothesis is also backed by the lack of nucleation on Cu surfaces. Cu is less electropositive than Al and does not readily undergo displacement reactions to generate H_2, which would lead to bubble formation. It is noted that detecting such bubbles visually or via in-situ spectroscopy is challenging since these experiments are carried out in a high-pressure cell, and the concentrations of any species will be low. Additional related evidence supporting the proposed mechanism lies in Figure 3.5, wherein increased Al-water interfacial area (and therefore more nucleation sites containing H_2 bubbles) for higher droplet volumes lead to a narrower distribution in the fraction of nucleating droplets towards lower time intervals. This suggests a causal relation between interfacial area enhancement and nucleation promotion.

Interestingly, the proposed nucleation mechanism suggests that Al might not be as good of a nucleating agent for CH_4 hydrates as compared to CO_2 hydrates. The solubility of CH_4 in water is much lower than that of CO_2, and the dissolved CH_4 will not result in the generation of carbonic acid, which can break down the native oxide layer to promote Al-water contact. While H_2 bubbles appear to be the most probable cause of

nucleation promotion, it is likely that there are additional factors, such as the roughness/texture at the micro/nano scale, which could also promote nucleation.

3.3 CONCLUSIONS

This chapter presented a simple, passive and novel approach to promote nucleation of CO_2 hydrates via the use of active metals such as Aluminum surfaces. Induction times as early as 8 minutes have been obtained using Al metals, whereas no nucleation was observed on stainless steel, copper or anodized Al surface. The nucleation promoting effect attributable to the interfacial reactions occurring at the Al-water interface could not be replicated by salts of Aluminum. Nucleation was observed to proceed from the Al-water interface in the bulk of the liquid. The findings presented in this chapter could seed further studies on metal-mediated hydrate nucleation and could be used as a guide to design materials for reactors to be used for rapid hydrate production in varied industrial applications.

Chapter 4: Studying the thermodynamics and kinetics of CO_2 hydrate nucleation in the presence of amino acids

This chapter reports thermodynamics and kinetics measurements of CO_2 hydrate nucleation in the presence of amino acids: measurements have been conducted using a novel approach. A multi-droplet configuration has been used to extract the nucleation kinetics and hydrate-liquid-vapor (HL_wV) p-T phase equilibrium data points in the presence of five non-polar amino acids, wherein water droplets on multiple aluminum plates inside a high-pressure vessel are monitored visually. Using such a configuration for thermodynamic measurements enables extraction of multiple data points (enabling high throughput measurements with minimal sample volume) and provides direct visual evidence for the relative inhibition impact of different thermodynamic hydrate inhibitors (THI) in a single experimental run. The kinetic inhibition effect is the highest for tryptophan and lowest for leucine/isoleucine and follows the order of hydropathy index that defines the relative extent of hydrophobicity of the amino acid side chain. Isoleucine and methionine exhibit the highest thermodynamic inhibition effect when compared to other amino acids, which do not significantly affect the thermodynamic formation conditions of CO_2 hydrates.

4.1 DESCRIPTION OF EXPERIMENTS

4.1.1 Materials

The chemical structure of the amino acids used in the present work is outlined in Table 4.1. All the amino acids L-leucine, L-isoleucine, L-phenylalanine, L-methionine and L-tryptophan were obtained from Sigma-Aldrich, and amino acid solutions were prepared using deionized water. CO_2 gas with a purity of 99.99% was used in all experiments. All the samples were weighed using a weight balance with an accuracy of

0.1 mg. The inhibition effect was studied for two different molar concentrations (0.1 and 0.2 mol%) for all the amino acids (except tryptophan, where only 0.1 mol% was used). These concentration values were selected based on the low inherent solubilities of the amino acids at atmospheric temperatures (present study), and considering that solubilities decrease with decreasing temperatures and increasing pH values (up to a particular value) [15].

Table 4.1 Physical properties of the amino acids considered in the present study.
[a]Numerical values were taken from Ref. [157].

Amino acid	**Molecular Weight (g/mol)**	**Molecular structure**	**Hydropathy index[a]**
Isoleucine	131.17	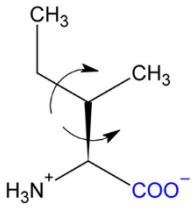	4.5
Leucine	131.17	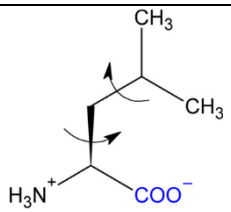	3.8
Phenylalanine	165.19	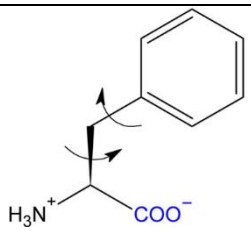	2.8
Methionine	149.21	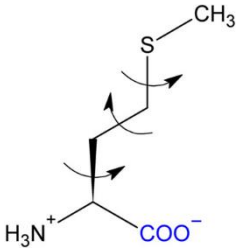	1.9

Table 4.1 (continued)

Tryptophan	204.23	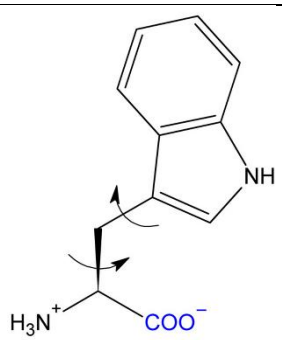	-0.9

4.1.2 Experimental apparatus and procedure

A custom-built non-stirred pressure vessel with oblong sapphire windows on either side obtained from Parr instruments was used to carry out the experiments. The vessel is equipped with a thermocouple and a pressure transducer connected to a data acquisition system that can continuously log the temperature and pressure every second with an accuracy of ±0.1 K and ±0.01 MPa, respectively. The droplets were dispensed on multiple Al metal plates positioned on top of each other using a substrate holder. A high-speed camera (Photron Fast cam) fitted with a macro lens (Tokina) was used to visualize the droplets through the optical sapphire windows. The vessel was placed inside an environmental chamber (ESPEC) that contains side slots for visualization and can cool or heat the vessel with a temperature resolution of 0.1 K.

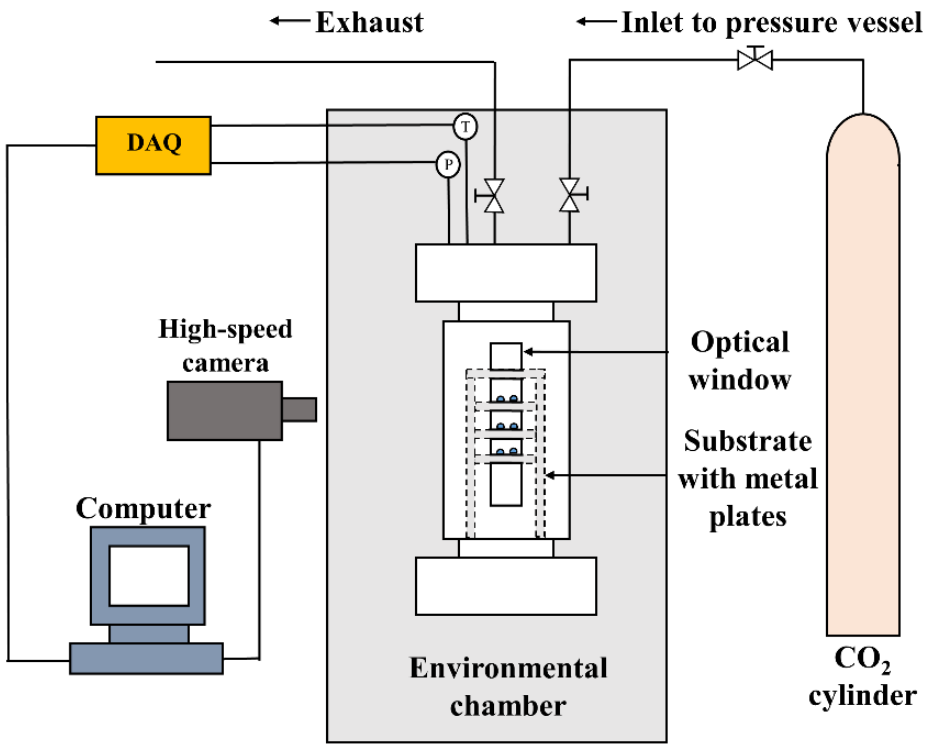

Figure 4.1 Schematic illustration of the experimental setup. Figure reprinted with permission from [148]. Copyright 2020 American Chemical Society

The experimental procedure consisted of cleaning the aluminum metal plates with isopropyl alcohol (IPA) and deionized (DI) water, followed by drying with nitrogen gas to ensure the surface was free from particulate matter and residual moisture. It is noted that fresh metal plates were used for every run. DI water droplets (volume: 20 µL) containing amino acids were dispensed on the plates with the inter droplet distance being sufficient to ensure that every droplet acted as an independent, isolated hydrate forming-microsystem without interference from the adjoining droplet. The pressure vessel containing the plates with droplets on them was purged with CO_2 gas for 60s to remove residual gases from the vessel environment.

For the kinetics experiments, the chamber was then isochorically cooled down to a temperature of 0.5 ^{o}C, and upon temperature stabilization, the vessel was then pressurized to 400 PSIG (2.8 MPa). Droplet nucleation was recorded using the high-speed camera, which was post-processed to obtain the induction times. For the thermodynamic experiments, the chamber was isochorically cooled down to about 3-4 K below hydrate formation temperatures and kept undisturbed in that environment for at least an hour to allow thermal equilibrium. The vessel was then pressurized with CO_2 gas to the desired experimental pressure and was left in that environment for about 4-8 hours (depending on the induction time) to allow all the droplets to nucleate. Hydrate nucleation in previous thermodynamic-related studies has been achieved by either resorting to subcooling the system to a very low temperature or using dry ice as nucleating agents. In this study, aluminum metal surface has been used to induce hydrate formation as it significantly enhances the nucleation kinetics of CO_2 hydrates [158].

Hydrate formation events can be monitored visually using the high-speed camera (as illustrated in Figure 4.2). Following nucleation of all droplets, the vessel was heated to a temperature very close to the dissociation condition (typically 1.5-2 K below the HL_wV point), followed by stepwise heating in slow steps of 0.1K/20 mins. When the temperature and pressure cross the HL_wV line, the hydrate-covered droplet dissociates, which could be observed via the optical windows on the vessel monitored by the high-speed camera. The video obtained from the high-speed camera was subjected to post-processing analysis wherein the droplet dissociation event was cross-referenced with the pressure and temperature reading recorded by the data acquisition system (DAQ).

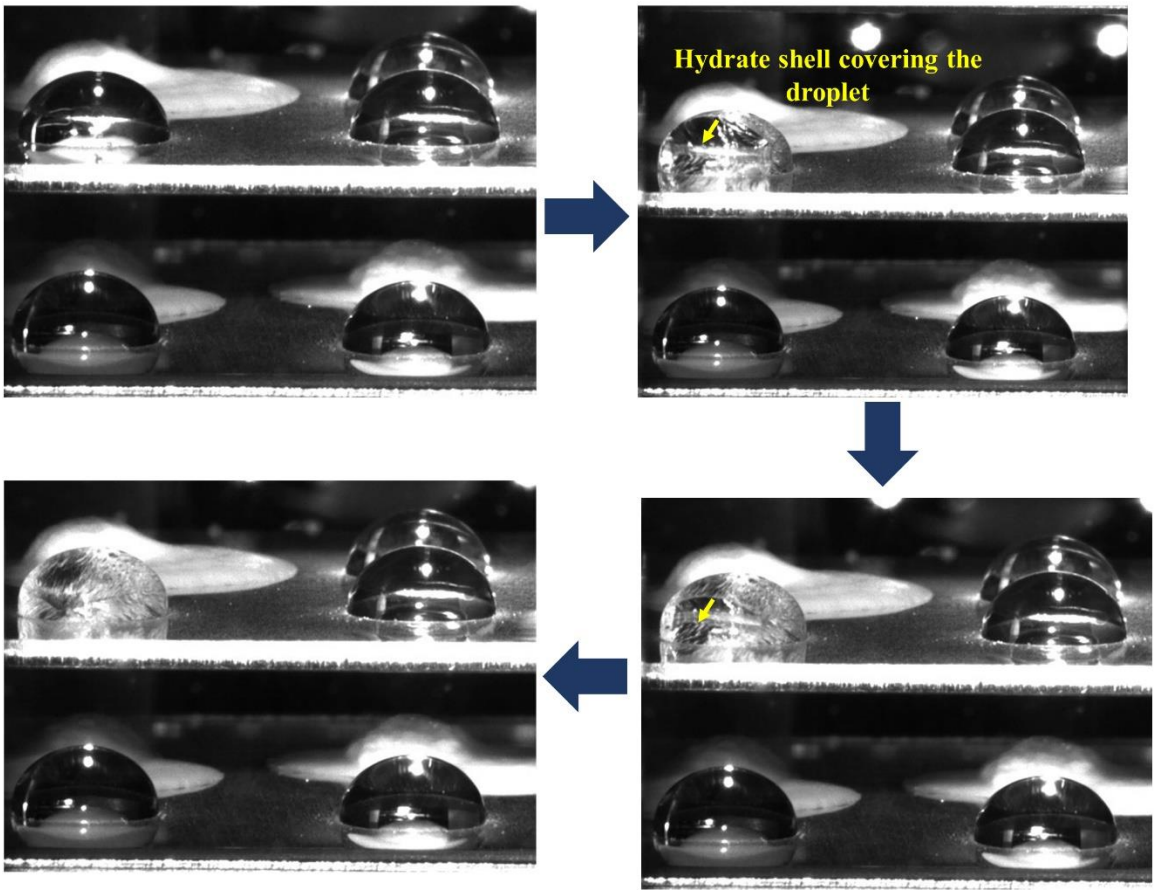

Figure 4.2. Snapshots at succeeding time intervals depicting film growth during a hydrate formation event.

4.1.3 Average depression in freezing point temperature

The average depression in freezing point temperature was calculated using Equation 4.1:

$$\bar{T} = \frac{1}{m}\sum_{i=1}^{m}\Delta T \qquad (4.1)$$

In the above equation, m is the number of data points, ΔT is the difference between hydrate dissociation temperature for samples containing amino acids, and dissociation temperature of pure CO_2 hydrate at constant pressure as calculated using the software CSMGem [14].

4.1.4 Calculation of nucleation rate

Nucleation rate was calculated using the following equation [149]:

$$P(t) = 1 - exp(-0.693 * J * t) \quad (4.2)$$

In the above equation, P(t) represents the nucleation probability. J is the nucleation rate which can be evaluated by fitting the above equation to the cumulative nucleation probability values obtained using the experimentally measured induction times.

4.2. RESULTS AND DISCUSSIONS

4.2.1 Kinetic measurements

Figure 4.3 depicts snapshots of the water droplets (20 µL) containing isoleucine before and after hydrate formation. Upon nucleation, the droplet turns opaque, which was used to evaluate the induction time. Up to 16 such droplets could be accommodated in one experiment using this configuration.

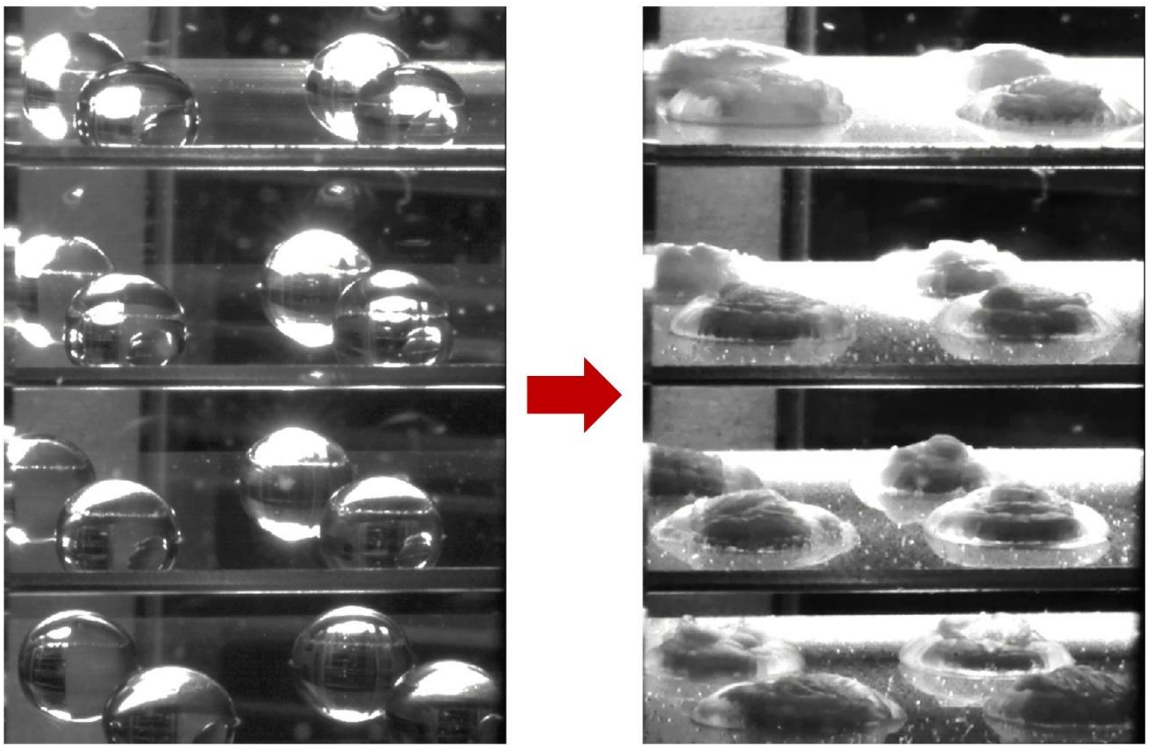

Figure 4.3. Water droplets containing isoleucine, before (left) and after (right) CO_2 hydrate formation.

Table 4.2 summarizes the induction time (average of at least 30 measurements) and nucleation rate data for 20µL water droplets containing amino acids at 0.1 mol% concentration. It is noted that the kinetics of phenylalanine has not been studied herein as it tends to spread vigorously upon nucleation, thereby affecting adjacent droplets. The kinetic inhibition effect of all the amino acids can be very clearly observed in Table 4.2, as droplets containing amino acids have an average induction time at least 15 mins higher than that for pure water droplets.

Table 4.2 Summary of induction time and nucleation rate data for 20µL water droplets containing various amino acids at 0.1 mol% concentration.

Amino acid	Induction time (min)			Nucleation rate (min^{-1})
	Average	Std dev	range	
Isoleucine	41	77.7	3.1-443.4	0.0481
Leucine	36.5	47.4	4.8-202.8	0.0487
Methionine	38.4	41.8	2.7-202.6	0.0415
Tryptophan	47.1	50.7	6.6-267.2	0.0316
Pure water	20	22.9	3.4-110.8	0.0739

The kinetic inhibition behavior observed via the average induction time data aligns with the trends underlying the nucleation rate (Table 4.2) and the graph of cumulative probability distribution curves (fitted using Equation 4.2), as illustrated in Figure 4.4. Pure water droplets have the highest nucleation rate of 0.0739 min^{-1} and the least average induction time of 20 mins, with the fastest nucleation occurring in 3.4 mins. On the other hand, droplets containing tryptophan were observed to have the slowest nucleation kinetics with a nucleation rate of 0.0316 min^{-1}, and an average induction time of 47.1 mins. It is interesting that the kinetic inhibition behavior trends observed in Figure 4.4 correlate with the hydropathy index values defining the extent of hydrophobicity/hydrophilicity of the alkyl group side chains, which describes the ability of amino acids to have access to water molecules or hinder their access to interact with water [157]. It is noted that higher/lower hydropathy values denote strong hydrophobicity/hydrophilicity.

One possible explanation for the inhibition behavior is that the presence of amino acids in water leads to the formation of zwitterions that affect the bulk water reorientation structure dynamics, which could be conducive to hydrate inhibition [159]–[161]. It was proposed by Sa et al. [162] that the kinetic inhibition of hydrates in the presence of amino acids is attributable to the perturbation of the structure of water molecules due to the

hydrophilic terminal groups and hydrophobic side chains via hydrogen bonding. However, the extent of perturbation was dictated by the properties of the side chain wherein amino acids containing hydrophilic side chains were observed to disrupt the local water structure, whereas those with a hydrophobic group were observed to strengthen this structure. Hydropathy has been observed to have an inverse correlation with hydrate inhibition impact for ionic liquids [163], and has been suggested to influence the inhibition behavior of amino acids on hydrates as well [15], [164], [165]. Based on the hydropathy index values, tryptophan is the least hydrophobic and would therefore cause the highest relative disruption to the structuring of the water molecules, during hydrate formation leading to the relatively slower nucleation kinetics. On the other hand, isoleucine and leucine have the highest hydropathy index amongst all the amino acids and subsequently exhibited the least kinetic inhibition effect.

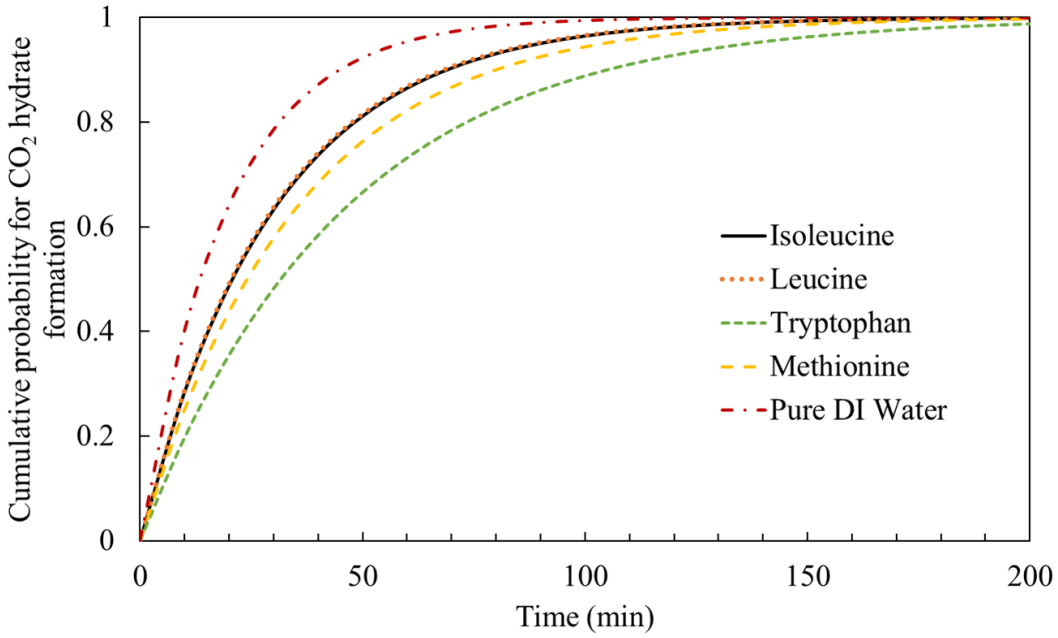

Figure 4.4. Cumulative probability distribution for CO_2 hydrate formation in the presence of amino acids. The graphs represent the curves fitted to the probability values obtained from the experimental induction time data points using Equation 4.2.

4.3.2 Thermodynamic measurements

To demonstrate the rigor and the validity of the experimental apparatus and the procedure adopted in this study, the thermodynamic phase equilibria (HL_wV) data points obtained for CO_2 hydrates with pure water were plotted (Figure 4.5) along with the data points reported in previous studies [166], [167] and predictions from CSMGem (which exhibits the highest accuracy amongst five common prediction programs [168]). The measured HL_wV data points exhibit excellent agreement with the values reported in literature and CSMGem predictions. Another important takeaway from Figure 4.5 is that aluminum does not affect the thermodynamics of CO_2 hydrate formation for the range of pressures and temperatures considered in the present study.

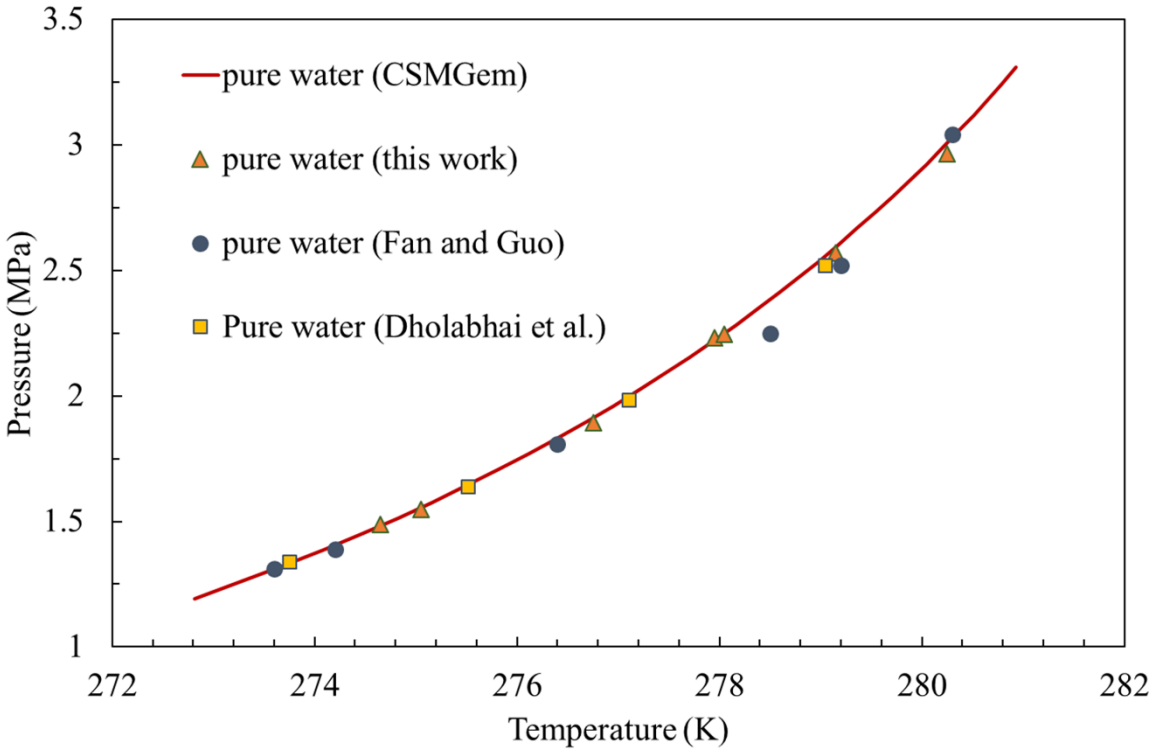

Figure 4.5 Comparison between experimental phase equilibria points obtained in the present work vs. CSMGem for pure CO_2 hydrates. The literature values were obtained from the work of Fan and Guo [166] and Dholabhai et al. [167]

Figure 4.6 illustrates the images captured during droplet dissociation, specifically during the time instants when the thermodynamic p-T conditions crossed the phase equilibrium boundary for CO_2 hydrates. In this particular case, isoleucine dissociates first, followed by leucine and pure water, denoting the order of inhibition impact. It is noted that the droplets with the highest depression in freezing point temperature will dissociate before the other droplets, which also serves as a visual tool to gauge the relative thermodynamic inhibition behavior for various amino acids. It is noted that the multi-droplet methodology adopted in the present study can be extended to investigate

the effect of any thermodynamically promoting or inhibiting chemical/salt/alcohol etc., on the phase equilibria of CO_2 hydrates.

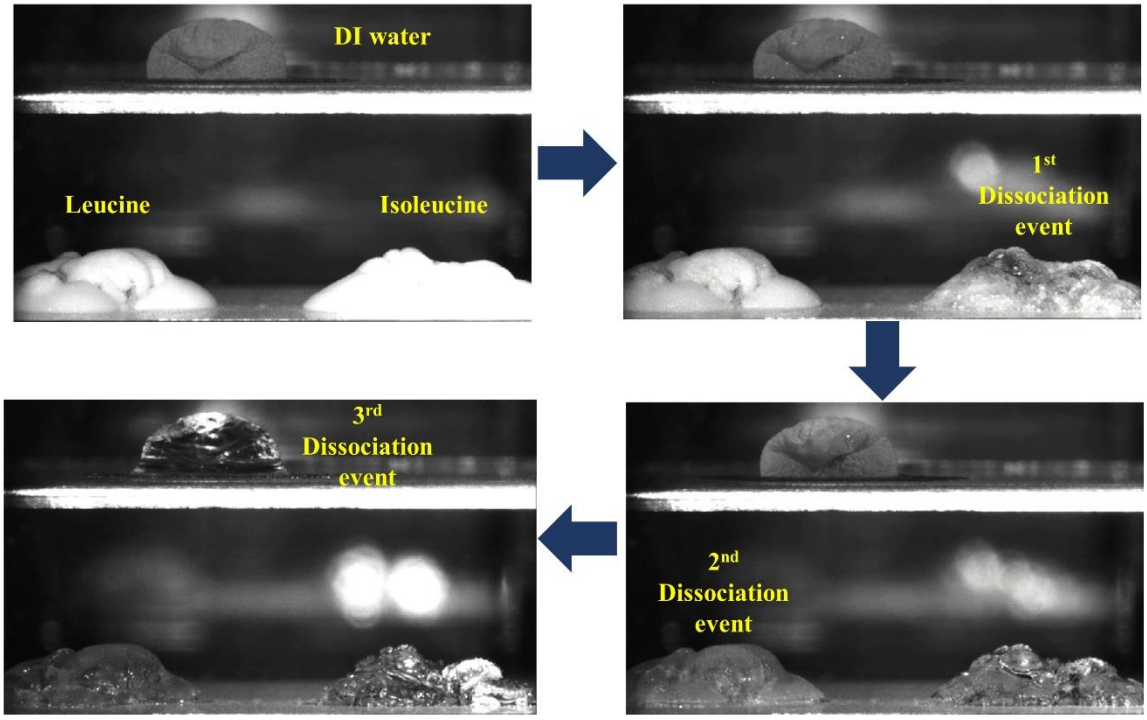

Figure 4.6. Snapshots showing the progression of dissociation events for pure water droplets and droplets containing isoleucine and leucine. Water droplet dissociates at the end, demonstrating the thermodynamic inhibition effect of the amino acids on CO_2 hydrates.

Figure 4.7 summarizes the experimental HL_wV data points obtained for CO_2 hydrates in the presence of varying concentrations of amino acids. Most amino acids have a negligible thermodynamic inhibition effect, attributable to the non-polar nature of the side chain and the low molar concentrations (0.1 and 0.2 mol %) explored in the present study (owing to very low solubilities at atmospheric pressure). The maximum inhibition effect was observed for isoleucine and methionine.

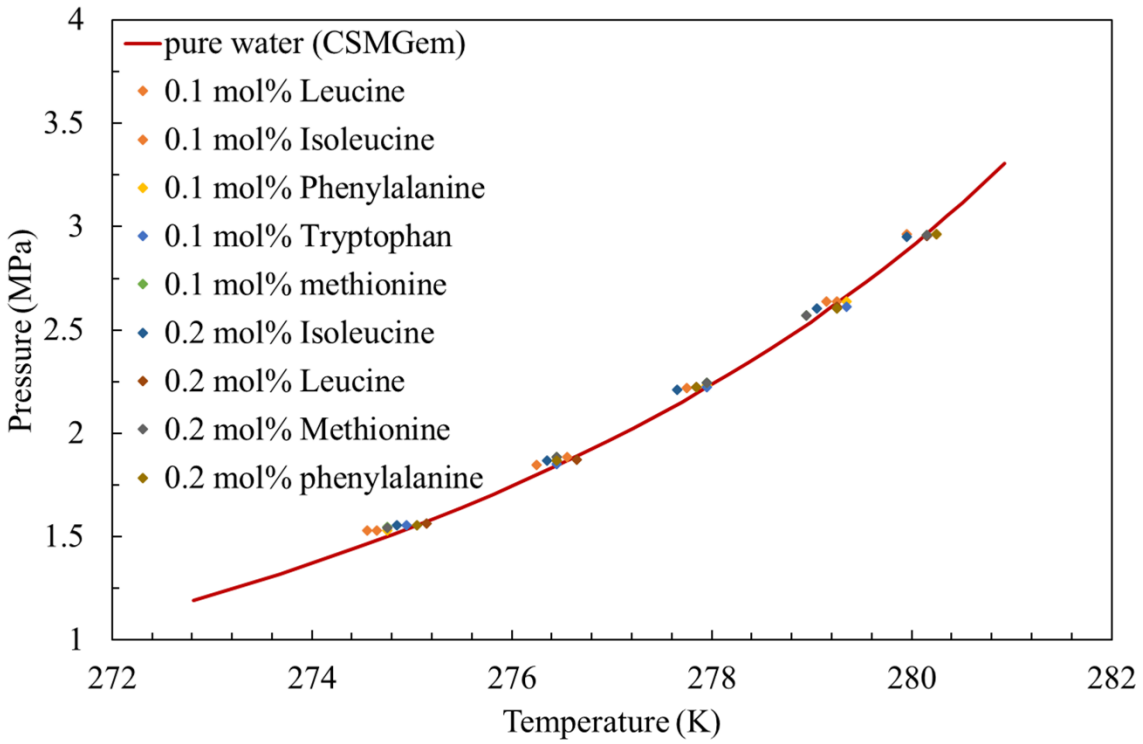

Figure 4.7. Experimentally measured HL_wV phase equilibrium data points for CO_2 hydrates in the presence of varying concentrations of amino acids.

In order to quantify the magnitude of the inhibition effect, the average depression in freezing point temperature was evaluated for all the amino acids as depicted in the histogram in Figure 4.8. The highest depression in freezing point temperature was observed for isoleucine (0.2 K) and methionine (0.12 K). The remaining amino acids had an average depression that was lesser than 0.1 K, which is the accuracy of the thermocouple used in the setup. Unlike the kinetic inhibition behavior, no dependence on the hydropathy index can be observed for the thermodynamic inhibition behavior.

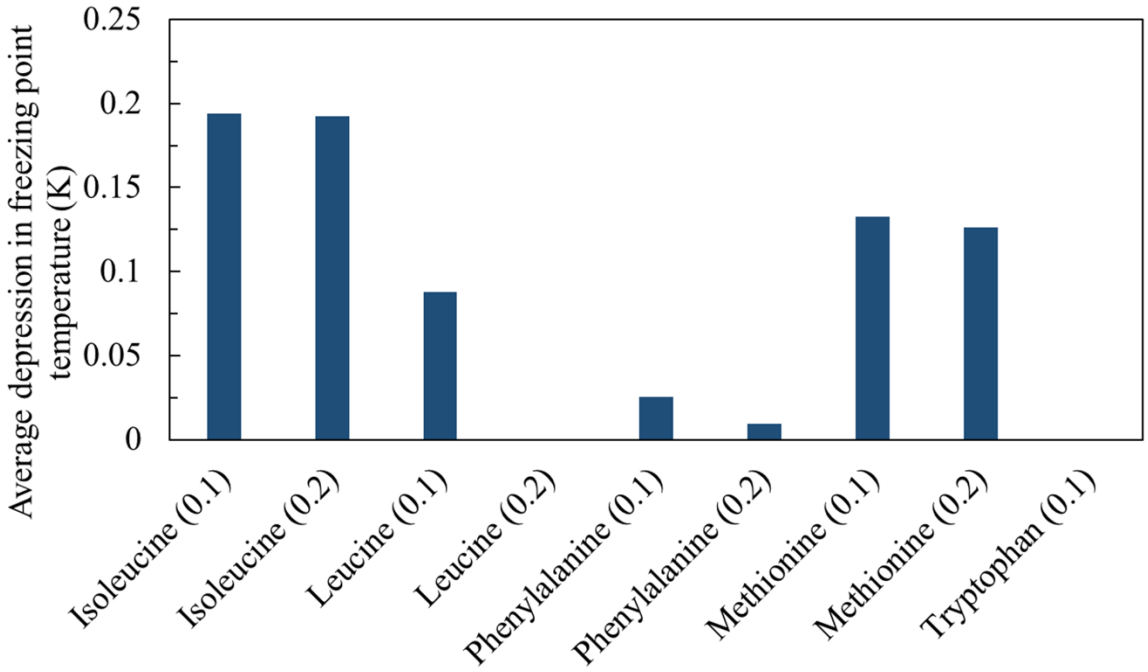

Figure 4.8 Average depression in freeing point temperature for the amino acids considered in the present study. Molar concentrations are denoted in mol% in brackets.

5.4 CONCLUSIONS

The kinetics and thermodynamics of CO_2 hydrate formation in the presence of five amino acids consisting of a non-polar side chain have been investigated in this chapter. All the amino acids were observed to inhibit the kinetics of hydrate formation, with the inhibition being the highest for tryptophan (nucleation rate: 0.0316 min^{-1}), and least for leucine and isoleucine (0.048 min^{-1}), with pure water droplets having the highest nucleation rate (0.0739 min^{-1}). The droplet-based configuration was also used to study the thermodynamic inhibition behavior: it was observed that isoleucine and methionine exhibit the highest inhibition with average depression in freezing point temperature corresponding to 0.2 and 0.12 K, respectively. The inhibition effect was trivial for other

amino acids, which can be attributed to a combination of its non-polar side chain and low molar concentrations (owing to low inherent solubilities) used in the present work.

Chapter 5: Thermodynamic features-driven machine learning-based prediction of clathrate hydrate equilibria[4]

This chapter discusses multiple advancements in the use of machine learning (ML) for prediction of hydrate formation/dissociation conditions. ML has been used to train and evaluate the performance of three algorithms on an experimental database (> 1800 data points) to predict hydrate dissociation temperatures as a function of the constituent hydrate precursors and inhibitors. Importantly, and in contrast to most previous studies, fundamental thermodynamic variables such as the activity-based contribution due to electrolytes, partial pressure of individual gases, and specific gravity of the overall mixture have been used as input features in the prediction algorithms. Using such features results in more physics-aware ML algorithms, which can capture the individual contributions of gases and electrolytes in a more fundamental manner. Three ML algorithms, Random Forest (RF), Extra Trees (ET), and Extreme Gradient Boosting (XGBoost) have been employed and demonstrate excellent accuracy in their predictions of hydrate equilibrium conditions. The overall coefficient of determination (R^2) percentage is greater than 97% for all the ML models. XGBoost outperforms RF and ET with the highest overall coefficient of determination (R^2) and the lowest overall Average Absolute relative deviation (AARD) of 99.56% and 0.086% respectively.

5.1 METHODOLOGY OF THE PRESENT STUDY

The first step in this study involved an in-depth literature survey and development of an extensive databank covering a wide range of hydrate formation conditions for different gaseous mixtures in the presence/absence of electrolytes. This database of

[4] The contents of this chapter have been published in the following journal article: Acharya, P.V. and Bahadur, V., 2021. Thermodynamic features-driven machine learning-based predictions of clathrate hydrate equilibria in the presence of electrolytes. *Fluid Phase Equilibria*, 530, p.112894. P.V.A. conceptualized the work, performed research, collected and analyzed the data.

experimental data was used to train the ML algorithm. Various advancements were then introduced to generate physics-aware ML models for prediction of hydrate formation/dissociation conditions. Firstly, the contribution of every gas was individualized by calculating partial pressures and using them as features in ML models. This enabled the algorithm to map hydrate dissociation temperatures directly to the fundamental parameters affecting the physics of the problem. When paired up with models such as SHAP [169], [170], such algorithms can track the amount of contribution of every gas and salt towards hydrate dissociation temperature. This can provide valuable insights for designing processes in applications involving gas hydrates.

Secondly, the contribution of the activity of water due to the presence of various electrolytes was calculated and used as a feature in the ML model. The inhibiting influence of electrolytes on hydrate dissociation temperatures in thermodynamic models was captured via the activity of water which is defined as the ratio of the vapor pressure of a water sample and the vapor pressure of pure water at the same temperature [171], [172]. Since activity was used as a feature, the influence of both molality and ionic strength could be captured while considering various intermolecular interactions. Another advantage of this approach stems from the fact that the weight percentages of different salts were fused into a single activity term. The activity term of another salt would compensate for the lack or discontinuity in experimental data for any particular salt, thereby making the databank more efficient and continuous. Furthermore, activity being a more fundamental parameter, it could then be ascribed to reflect the presence of any salt or a combination of salts depending on the weight percentage leading to the same activity. In essence, this allows meaningful predictions of HDT from the use of a salt or a combination of salts.

Thirdly, specific gravity has been used as a feature to capture the influence of average molecular weight on the HDT. Overall, *ML models have been developed using fundamental thermodynamic parameters of the constituent gases or chemicals in the system*. In doing so, the ML models have used a low number of features to backtrack individual contributions of gases or salts; this would not be possible from the previously used approaches involving total pressures and weight percentages.

The prediction performance of three different ensemble-based ML methods: Random Forest (RF) [173], Extremely randomized trees (ET) [174], and Extreme Gradient Boosting (XGBoost) [175] has been evaluated. Their relative performance has been assessed to predict HDT using activity, partial pressure and specific gravity as input features. While prior studies have used gradient boosting (GB) algorithms, this is the first reported use of Extreme Gradient Boosting [175] (which is a computationally efficient variant of gradient boosting algorithm) for hydrates-related predictions. It is noted that due to its efficiency and ease of use, XGBoost (since its inception in 2015) has been widely used in Kaggle competitions and a variety of ML and data mining challenges.

5.2 DESCRIPTION OF MACHINE LEARNING MODELS

Ensemble-based techniques combine several base models to produce one optimal prediction model by decreasing variance and bias via bagging (bootstrap aggregating) and boosting. Among ensemble models, decision tree-based methods have become widely popular due to their ease of implementation, versatility, and intuitive interpretation.

5.2.1 Random Forest and Extra Trees

A typical decision tree stratifies or segments a predictor space into several simple regions based on a set of splitting rules to optimize a specific objective function. The value of a prediction for a particular observation would be the mean or mode of the trained observations in the region/branch where it belongs (usually denoted as the terminal node or leaves of the tree) based on the splitting rules defining that particular observation. Since the set of splitting rules used to divide the predictor space can be displayed graphically as a tree (Figure 5.1), such methods are called decision tree-based methods.

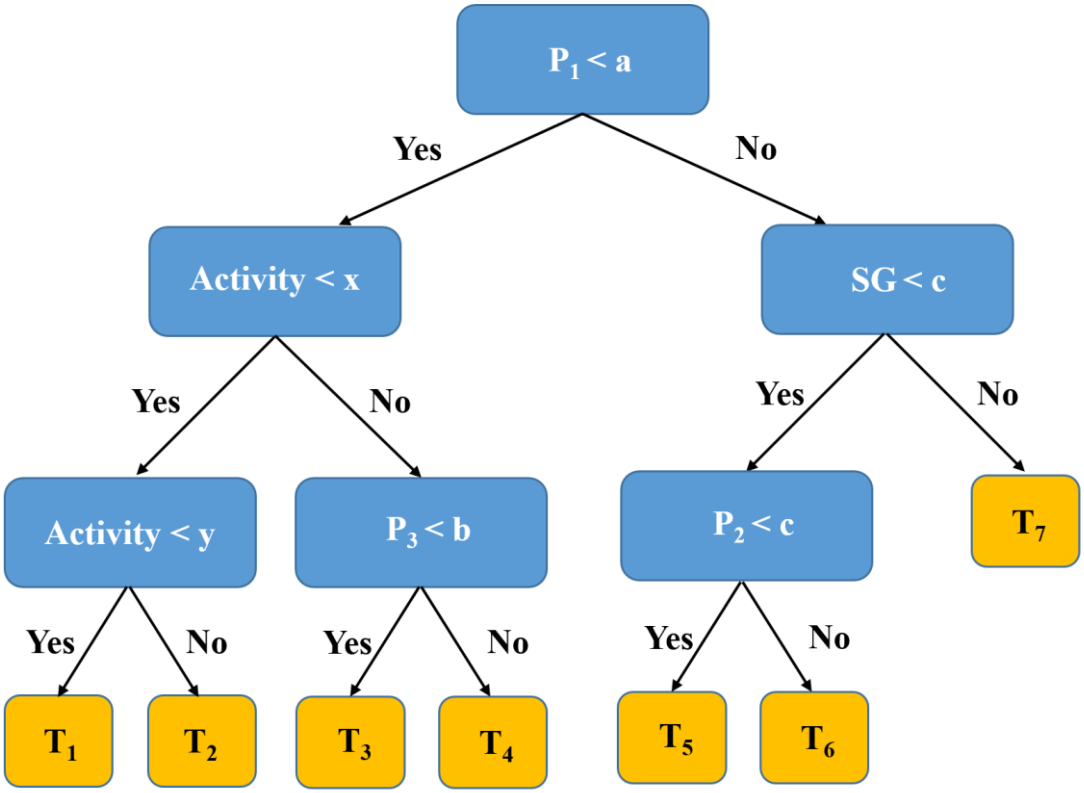

Figure 5.1. An illustrative decision tree associated with hydrate dissociation temperature predictions.

When a single decision tree trained on a particular data set is used for prediction, it can exhibit a very high variance; wherein the model performs poorly for data sets other than the ones used for training the model. In order to reduce variance and increase the robustness of the model, two powerful ML techniques – bagging or bootstrap aggregation, [176] and random feature selection [177] are implemented in a decision tree-based method. The fundamental idea is to fit multiple decision trees on several training data sets and average the resulting observations to decrease the overall variance of the machine learning model. To provide multiple training data sets from the available data, bootstrapping is carried out wherein the data set is resampled multiple times with replacements to create many simulated samples that have the same size as the original data set. Subsequently, N different trees are trained over N bootstrapped samples of data, and the results obtained from these trees are then averaged to obtain the final output. In random feature selection, only a tiny subset (m) of predictors is chosen out of all the predictors (p) every time a split decision is made in the internal node of a tree (m is typically chosen to be equal to $\sqrt{p}$), which decorrelates individual trees in the forest. Random forest combines both these techniques (bagging and random feature selection), to provide a very strong generalized prediction model.

Extremely randomized trees are similar to random forest-based methods, albeit with two key differences, i) the entire dataset is used to grow a tree instead of bootstrap sampling, ii) the internal cut point used to make a decision split is selected at random instead of searching for the most optimal split.

5.2.2 XGBoost (Extreme gradient boosting)

Boosting is a form of additive modeling based on building a sequence of multiple weak learning models and combining them into a single composite robust model. The

underlying ideology is that the resultant collective model becomes a stronger predictor as more weak learning models are sequentially added. While the weak learning models can be built independently, as in the case of random forest or extra trees, boosting relies on building these weak learners in a stage-wise fashion with each learner chosen to improve the overall model performance by optimizing a specific objective function.

In this study, XGBoost algorithm [175] (operating under the gradient boosting framework) has been implemented, which uses the first and second derivative of the loss function to converge to global optimality quicker while also improving the efficiency of the optimal solution of the model. The objective function minimized by XGBoost is as follows [175]:

$$obj(\theta) = \sum_i l(\hat{y}_i, y_i) + \sum_k \Omega(f_k) \tag{5.1}$$

$$\Omega(f_k) = \gamma' T + \frac{1}{2}\lambda' \|w\|^2 \tag{5.2}$$

In the above equation, l is a differentiable convex loss function that measures the difference between the prediction $\hat{y}_i$ and target y_i, and f_k is the k^{th} tree. The second term Ω helps to prevent overfitting by penalizing the complexity of the model in terms of the number of leaves in the tree T and vector of scores on leaves w. Here λ' is a regularized parameter and γ' is the learning rate, whose values lie between 0 and 1.

Since a tree ensemble model includes functions as parameters, it cannot be optimized using traditional optimization methods in Euclidean space and is therefore trained in an additive manner. The objective function to be minimized is then given by:

$$L^{(t)} = \sum_{i=1}^{k} \left[l\left(y_i, \hat{y}_i^{(t-1)}\right) + f_t(x_i) \right] + \Omega(f_t) \tag{5.3}$$

In the above equation, $\hat{y}_i^{\,t}$ is the prediction of the i^{th} instance at the t^{th} iteration, and k is the total number of predictions. Therefore, the loss function is represented as the sum

of the loss functions for the prediction till the *t-1*th iteration and a tree structure that, when added at the t^{th} iteration, most improves the model as per Equation 5.3. Accordingly, the objective function can be optimized by using the second-order Taylor's approximation of the loss function (instead of first-order in general gradient boosting), which is given by [175]:

$$L^{(t)} \simeq \sum_{i=1}^{k}\left[l\left(y_i, \hat{y}_i^{(t-1)}\right) + g_i f_t\left(x_i\right) + \frac{1}{2} h_i f_t^2\left(x_i\right)\right] + \Omega\left(f_t\right) \tag{5.4}$$

where, $g_i = \partial_{\hat{y}_i^{(t-1)}} l\left(y_i, \hat{y}_i^{(t-1)}\right)$ and $h_i = \partial^2_{\hat{y}_i^{(t-1)}} l\left(y_i, \hat{y}_i^{(t-1)}\right)$ represent the first and second derivatives of each sample. The sum of loss values determines the loss function in equation 5.4 for each data sample corresponding to every leaf node. Assuming that the loss function is the mean square error function for regression problems and removing the constants, the objective function can be written for regression tree-based problems as [175]:

$$L^{(t)} \simeq \sum_{j=1}^{T}\left[\left(\sum_{i\in I_j} g_i\right) w_j + \frac{1}{2}\left(\sum_{i\in I_j} h_i + \lambda'\right) {w_j}^2\right] + \gamma T \tag{5.5}$$

where, I_j represents all the data samples in the leaf node. During the process of building a tree, a particular node split will only be carried out if there is an improvement in the performance of the model as evaluated by this objective function.

5.3 DEVELOPMENT OF MACHINE LEARNING MODELS

5.3.1 Experimental database

The predictive utility of any data-driven ML model is highly dependent on the experimental dataset employed for training the model. In order to predict the HDT of gas

hydrates from pure gases and a mixture of gases in the presence of electrolytes, an extensive dataset comprising of more than 1800 phase equilibrium data points was collected from published literature. Table 5.1 summarizes the key details of the gathered experimental dataset. The dataset includes P-T data for varied combinations of seven gases and four salts.

The data used in the present study was obtained from the following sources: Dholobhai et al. [178], Englezos and Ngan [179], Dholabhai and Bishnoi [180], Mei et al. [181], Kang et al. [182], Tatsuo [183], Jager and Sloan [184], Kharrat and Dalmazzone [185], Atik et al. [186], Mohammadi et al. [187], Haghighi et al. [188], De Roo et al. [189], Maekawa et al. [190], Dholabhai et al. [191], Nakane et al. [192], Tohidi et al. [193], Holder and Grigoriou [194], Paranjpe et al. [195], Adisasmito et al. [196], Adisasmito and Sloan [197], Nixdorf and Oellrich [198], Ng and Robinson [199], Holder and Hand [200], Ghavipour et al. [121], Jhaveri and Robinson [201], Wu et al. [202], Deaton and Frost [203], Verma [204], Unruh and Katz [205], Ohgaki et al. [206], Fan and Guo [207], Seo et al. [208] and Ng et al. [209].

Table 5.1. Summary of the experimental database used in the present study.

Variable	Units	Min	Max	Average
P	MPa	0.13	72.26	6.92
T	K	247.52	303.48	278.35
CO_2	mol%	0	100	20.1
CH_4	mol%	0	100	51.59
C_2H_6	mol%	0	100	9.39
C_3H_8	mol%	0	100	12.67
n-C_4H_{10}	mol%	0	100	1.29
i-C_4H_{10}	mol%	0	88.8	1.26
N_2	mol%	0	100	3.69
NaCl	wt %	0	24.11	2.48
KCl	wt %	0	20	0.69
$CaCl_2$	wt %	0	25.75	1.14
$MgCl_2$	wt %	0	15	0.41

5.3.2 Calculations of activity and partial pressure

The contribution of electrolytes towards the activity of water is calculated using the Pitzer-Debye Huckel equation [210] and N-NRTL-NRF model [211] to capture the long and short-range interactions, respectively. Accordingly, the contribution due to electrolytes can be evaluated via an activity term as:

$$\ln a_{w,el} = \sum_{i}^{N_{el}} \upsilon_i m_i \ln a_{w,eli} \Big/ \sum_{i}^{N_{el}} \upsilon_i m_i \tag{5.6}$$

where υ is the stoichiometric number of ions in the i^{th} electrolyte and m_i is the molality of the i^{th} electrolyte in the mixed electrolyte solution.

$$a_{w,eli} = x_w \gamma_w \tag{5.7}$$

where the activity coefficient of water γ_w is calculated using a combination of short-range (SR) and long-range (LR) interaction terms:

$$\ln \gamma_w = \ln \gamma^{SR} + \ln \gamma^{LR} \tag{5.8}$$

The short range contribution can be calculated using N-NRTL-NRF model as [211]:

$$\ln \gamma^{SR} = x_{el}{}^{2}\left(\lambda_{el,w}\Gamma_{el,w}{}^{2} + \frac{\lambda_{el,w}\Gamma_{el,w}{}^{2}}{\beta_{w,el}} - \lambda_{el,w} - \lambda_{w,el} \right) \tag{5.9}$$

$$m_{eli} = \frac{1}{\upsilon_i}\sum_{j}^{N_{el}} \upsilon_j m_j \tag{5.10}$$

$$x_w = \frac{1000/M_w}{1000/M_w + \upsilon m_{eli}} \tag{5.11}$$

$$x_{el} = 1 - x_w \tag{5.12}$$

$$\upsilon = \upsilon_a + \upsilon_c \tag{5.13}$$

$$\Gamma_{w,el} = \frac{x_w \beta_{w,el}}{x_w \beta_{w,el} + x_{el}} \tag{5.14}$$

$$\Gamma_{el,w} = \frac{x_{el} \beta_{el,w}}{x_{el} \beta_{el,w} + x_w} \tag{5.15}$$

$$\beta_{w,el} = \exp\left(-\alpha \lambda_{w,el}\right) \tag{5.16}$$

$$\beta_{el,w} = \exp\left(-\alpha \lambda_{el,w}\right) \tag{5.17}$$

In the above equations, x_w & M_w denote the mole fraction and molecular weight of water, and m_{eli} is the molality of the i^{th} electrolyte in the single electrolyte solution. λ represents the optimized binary parameters for salt-water interactions (values for which have been taken from [212]), Γ denotes non-random factors and β is the Boltzmann factor. It is noted that the interactions between dissolved gas and electrolytes have not been considered while evaluating $a_{w,eli}$. For the LR contribution, the Pitzer Debye Huckel equation for the ionic species can be expressed as [210]:

$$\ln \gamma^{LR} = \frac{x_{el}}{x_w} A_\phi \left(\frac{1000}{M_w} \right)^{1/2} \left(\frac{\left| z_a z_c \right| I^{1/2} - 2I^{3/2}}{I + \rho I^{1/2}} \right) \tag{5.18}$$

$$I = \frac{1}{2}\left(x_a z_a{}^{2} + x_c z_c{}^{2} \right) \tag{5.19}$$

where I is the molar fraction ionic strength. The non-randomness factor α, Debye−Hückel constant A_ϕ, and closest approach ρ are equal to 0.125, 0.390947 and 14.90 respectively [211], [213].

It is noted that the influence of alcohol/s or other organic solvents on hydrate formation has not been considered in this study. It is noted that the activity calculated for alcohol/s using the commonly employed Margules equation [214] does not lead to the same extent of suppression in hydrate formation conditions when compared to electrolyte solutions with the same activity (calculated using Pitzer-Debye Huckel equation and N-NRTL-NRF model). This suggests that although the use of activity as a feature is an improvement over previous approaches, the models used to evaluate activity are also crucial to accurate prediction of hydrate forming conditions. To ensure consistency and obtain meaningful predictions from the present study, only electrolytes have been considered in this analysis. It is noted that partial pressures of individual gases were estimated using mole fractions and total pressure assuming ideal gas behavior.

Overall, the use of activity, specific gravity, and partial pressures as features instead of weight percentages and mole fractions make the current approach more firmly grounded in fundamental chemical thermodynamics and increases the generality and applicability of the developed predictive models.

5.3.3 Procedure for conducting ML analysis

The dataset was divided into training and test data using train_test_split function from Scikit-learn library [215], which randomly assigns 85% of the dataset for training the model and the remaining 15% for evaluating the accuracy and performance of the trained model. The performance of an ML model depends significantly on its hyperparameters, which define the model's complexity and thereby its capacity to learn

from any data. In tree-based models, typical hyperparameters include the number of trees to grow in the forest, maximum depth of each tree, number of samples to be considered for each split, minimum number of data points allowed in a leaf node etc. For XGBoost algorithm, additional hyperparameters come into play, such as the learning rate, minimum loss reduction required to make a split, subsample ratio of the training instances etc. It is noted that tuning the hyperparameters using the training dataset without cross-validation can lead to overfitting where the model performs really well on the training data set but rather poorly on the test data set.

Exhaustive grid search cross-validation (CV) has been employed with a two-step approach to carry out optimization. In the first step, a hyperparameter grid consisting of a wide range of parameter values was created, and combinations were sampled at random to narrow down a range of values by evaluating their results using 5-fold cross-validation. Following this, an extensive grid search was conducted on the concentrated parameter space by evaluating all possible combinations in the hyperparameter grid to arrive at the combination yielding the best results. It is noted that the hyperparameters were evaluated to avoid overfitting the data set to provide the best fit for a broad spectrum of data points. To carry out grid search cross-validation and implement the ML algorithms in Python, an open-source ML library Scikit-learn was used [215].

5.4 RESULTS AND DISCUSSIONS

5.4.1 Validity of the model

After estimating optimum hyperparameters, ML algorithms were trained using thermodynamic variables (partial pressure, specific gravity and activity) as features. Subsequently, their prediction performance was evaluated on the test data set. In order to evaluate the reliability and accuracy of the developed ensemble models, two key

statistical metrics were used, namely coefficient of determination percent (R^2 %) and average absolute relative deviation percent (AARD %), as defined below:

$$R^2\% = 100\left(1 - \frac{\sum_{i=1}^{n}\left(T_{pred} - T_{\exp}\right)^2}{\sum_{i=1}^{n}\left(T_{pred} - average(T_{\exp})\right)^2}\right) \tag{5.20}$$

$$AARD\% = 100\sum_{i=1}^{n}\left|\frac{T_{pred} - T_{\exp}}{T_{\exp}}\right| / n \tag{5.21}$$

Table 5.2 summarizes the performance metrics for Random forest, Extra Trees, and XGBoost models with the previously described experimental dataset of more than 1800 data points. It is evident that the XGBoost algorithm outperforms Random Forest and Extra Trees algorithms with R^2 accuracies of 99.85% (training data), 98.06% (test data) and 99.56% (overall). Random Forest and Extra Trees models exhibited almost similar prediction accuracies. Compared to the other two algorithms, the XGBoost algorithm results in a noticeably improved prediction accuracy for the test data (an improvement of about 4%). These results are in line with previous observations wherein boosting methods have improved predictions compared to traditional models [216]. Importantly, all three ML models provide excellent prediction accuracies while using fundamental thermodynamic variables of the constituent gases and salts (activity, partial pressures, and specific gravity). This shows that setting up ML models in terms of fundamental thermodynamic parameters instead of specifying compositions does not compromise the accuracy of the predictions.

Table 5.2 Accuracy of predictions obtained by ML algorithms employed in the present study.

	Random Forest			Extra Trees			XGBoost		
	Train	**Test**	**Total**	**Train**	**Test**	**Total**	**Train**	**Test**	**Total**
R^2 %	97.84	94.35	97.53	98.45	94.08	98.01	99.85	98.06	99.56
AARD %	0.210	0.363	0.233	0.184	0.383	0.214	0.064	0.212	0.086

Figure 5.2 compares the predicted HDT for training and test data sets (combined) versus experimental data, the dashed line being the identity line, y=x. The distance of a point from the identity line is a measure of the prediction accuracy of the particular model. A distribution of points closely clustered to the identity line is a visual indicator of good predictions. It is seen from Figure 5.2c that XGBoost results in better predictions, as evident by a majority of data points very closely clustered around the identity line. The relative error is highest for two data points having the highest deviation from the identity line. These correspond to T_{exp} of 247.52K [for $P_{methane}$=2.56MPa (97.07 mol%) and $P_{propane}$=0.077MPa (2.93 mol%)] and T_{exp} of 296.07K [for $P_{carbon\ dioxide}$=1.91 MPa (8.09 mol%), $P_{methane}$=21.07 MPa (89.4 mol%) and P_{ethane}=0.587 MPa (2.49 mol%)]. Deviations for these points can be very clearly noticed in the plots for Random Forest (Figure 5.2a) and Extra Trees (Figure 5.2b) methods. The deviation for the point T_{exp}=247.52 K belonging to the training data set can be attributed to a lack of experimental data around lower temperature ranges, resulting in poorer predictions compared to other points. The deviation for the point T_{exp}=296.07 K belonging to test data set at very high partial pressures of CH_4 can be explained either by a lack of experimental data points at higher pressures or possible local overfitting due to random allocation of test train data. It is noted that XGBoost results in better predictions at these two most deviant points as well. The relative deviation resulting from the use of XGBoost (1.12% and -2.23%, respectively) is much lower than the relative deviations resulting from the prediction of

the Random Forest (5.98% and -4.40%, respectively) and Extra Trees (5.17% and -4.79%, respectively) methods. This highlights the robustness and superior predictive capabilities of the XGBoost model. It is noted that two data points corresponding to HDT of 242.09 K and 252.8 K, which belong to the lower end of the temperature spectrum, yielded absolute relative errors greater than 10% and have been considered as outliers in the present study.

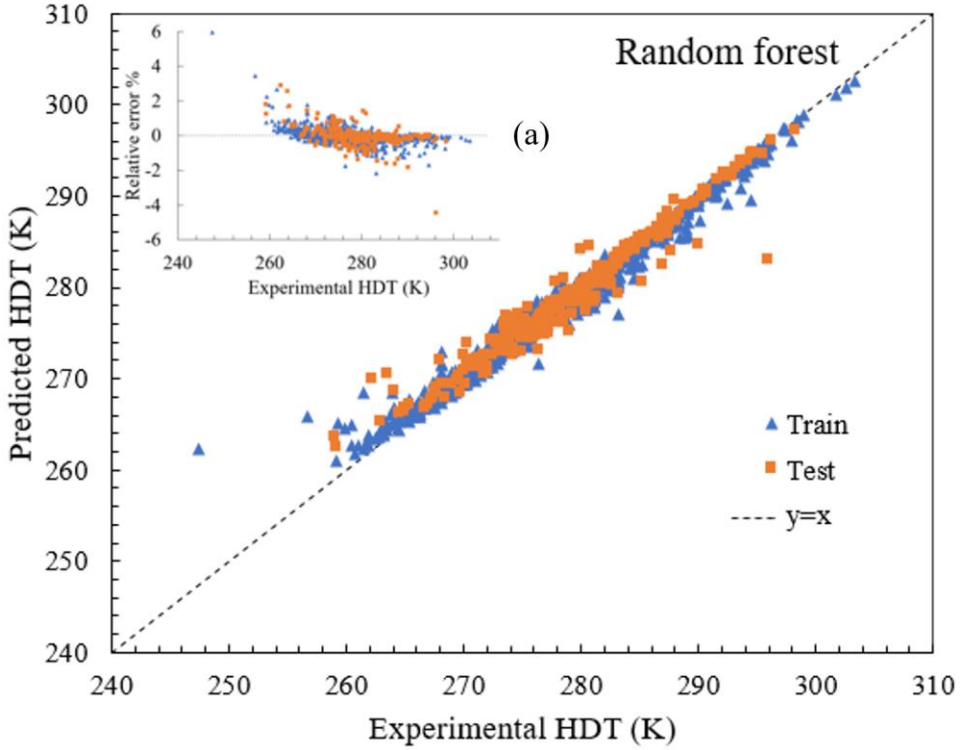
Random forest
(a)
Relative error %
Experimental HDT (K)
Predicted HDT (K)
Experimental HDT (K)
Train
Test
y=x

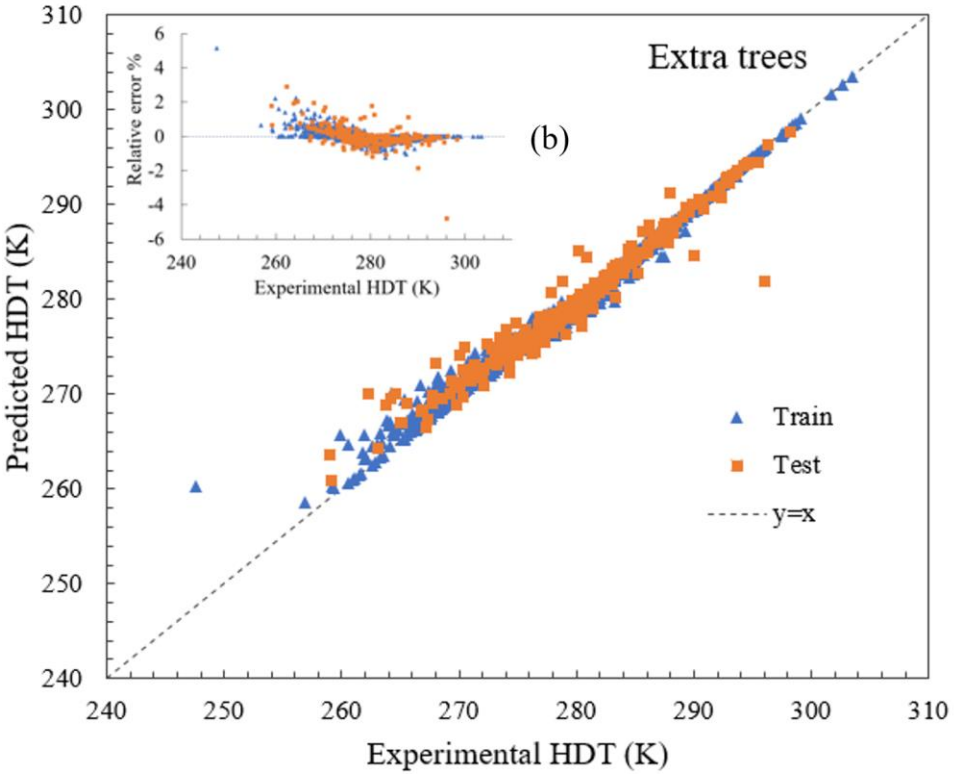
Extra trees
(b)
Relative error %
Experimental HDT (K)
Predicted HDT (K)
Experimental HDT (K)
Train
Test
y=x

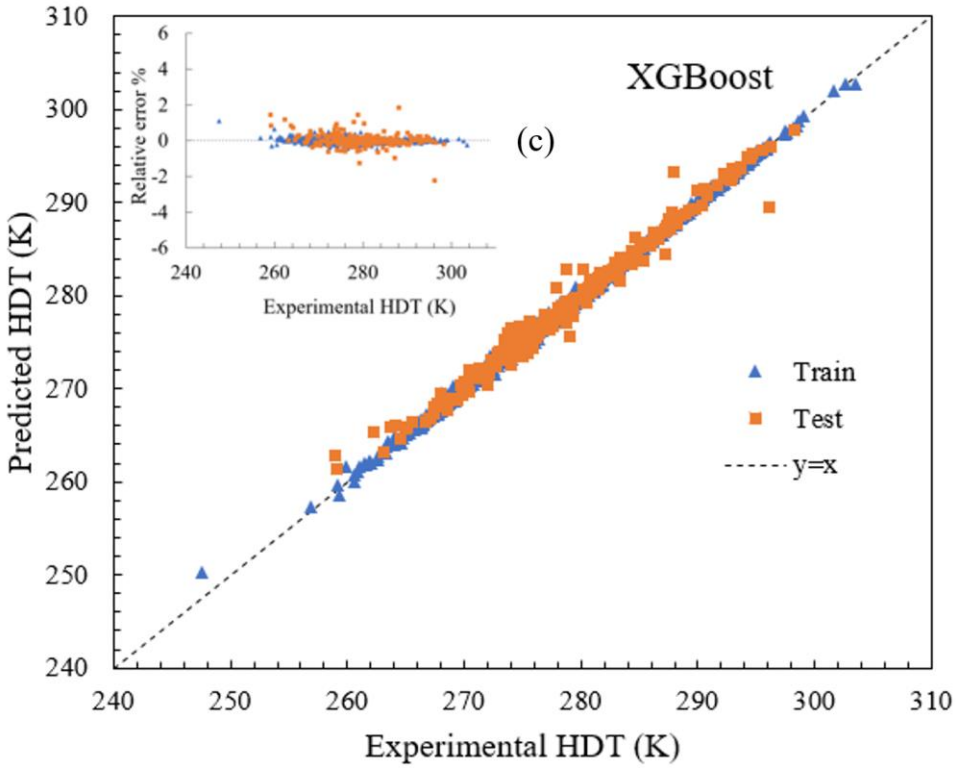

Figure 5.2. Comparison of experimental hydrate dissociation temperatures versus predictions obtained from three ML models, (a) Random Forest, (b) Extra Trees, and (c) XGBoost.

Further insights on the relative performance of the models is obtained by analyzing the distribution of the absolute relative error between the experimental and predicted HDTs for training and test data sets, as shown in Figure 5.3. and the distribution of relative error, as shown in the inset of Figure 5.2. The concentration of a large number of data points in low absolute relative error regions for training and test data sets indicates the superior prediction performance of the XGBoost algorithm. A majority of the data points exhibited relative errors less than 0.5% for all three methods. XGBoost has the highest overall number of data points (1802) with absolute relative errors lower than 0.5%, implying that it can predict about 98.3% of the entire (training + test) data set with greater than 99.5% relative accuracy. This is followed by Random

Forest (1608 data points) and Extra Trees methods (1656 data points) corresponding to 87.67% and 90.29% of the data points with absolute relative errors less than 0.5%. As can be inferred from the R^2 plot (Figure 5.2), the highest relative errors for the two temperatures (247.52 and 296.07 K belonging to the training and test data set, respectively) correspond to the two points towards the right end of the histogram.

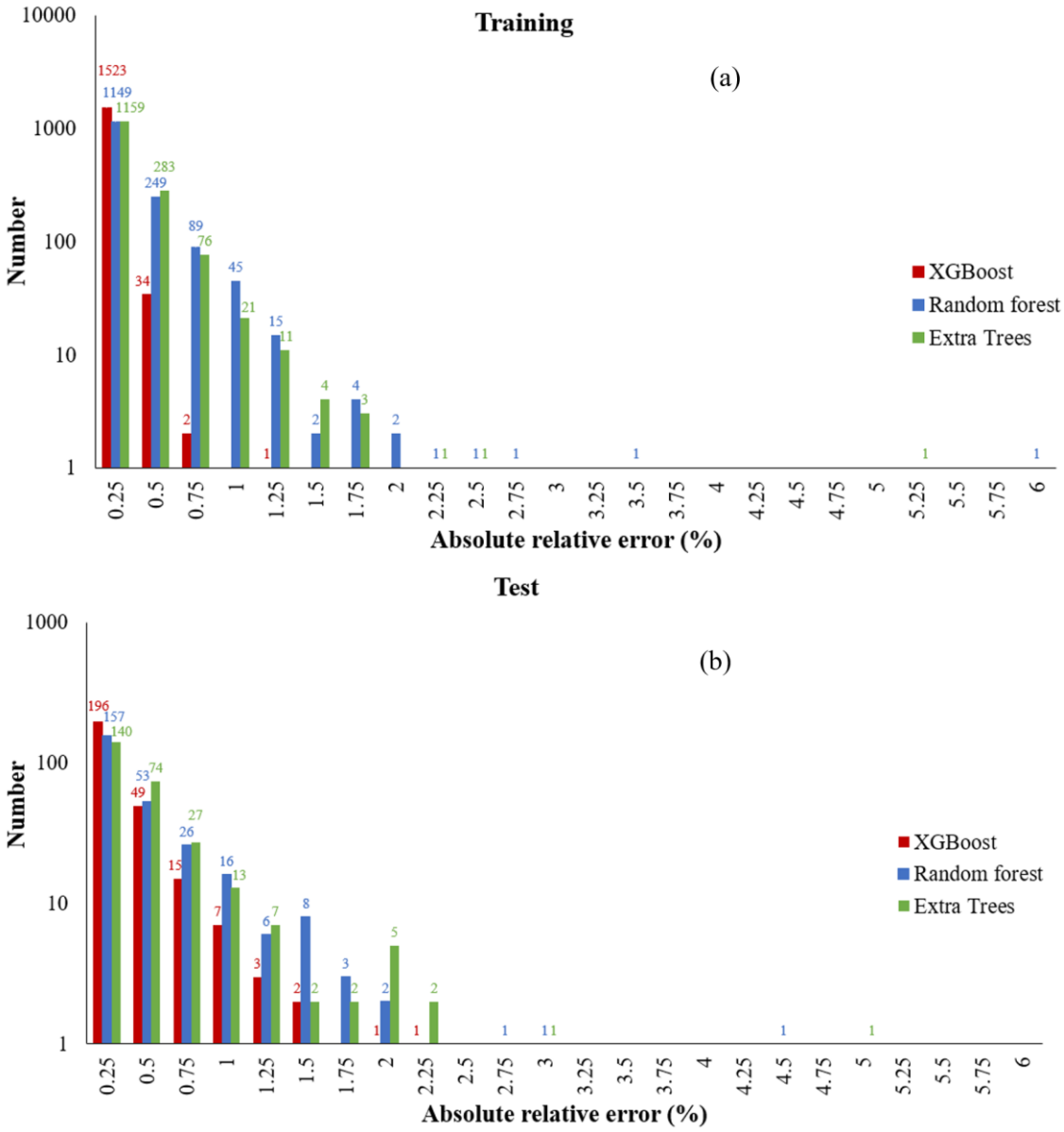

Figure 5.3. Distribution of the absolute relative error in predicting hydrate dissociation temperature (logarithmic y-axis) for (a) training and (b) test data sets obtained using XGBoost, Random Forest and Extra Trees algorithms.

Next, the utility of the XGBoost model in predicting the inhibition influence of salts on hydrate formation has been illustrated. Figures 5.4. (a-b) show the experimentally obtained [185], [189] pressure-temperature curves (non-solid symbols) associated with

the formation of methane hydrates in the presence of NaCl and $CaCl_2$, respectively. It is seen that the addition of salts pushes the hydrate formation region to the left (higher pressures and/or lower temperatures needed for hydrate formation). Experimentally provided weight concentrations were used to estimate the activity feature used in the ML models. From a chemical thermodynamics perspective, increased salt concentrations reduce activity, which will push the P-T curve to the left. Figures 5.4 (a-b) show the predictions of the XGBoost model; an excellent match is seen in the majority of the range of temperatures and pressures studied. There is a notable deviation for data points in lower temperatures (259.9-264 K) at 25.75 wt% $CaCl_2$ which can be attributed to a lack of experimental data points used for training the ML models at lower temperature ranges. Overall, the model can effectively capture the inhibition influence of salts containing monovalent as well as divalent cations in the solution.

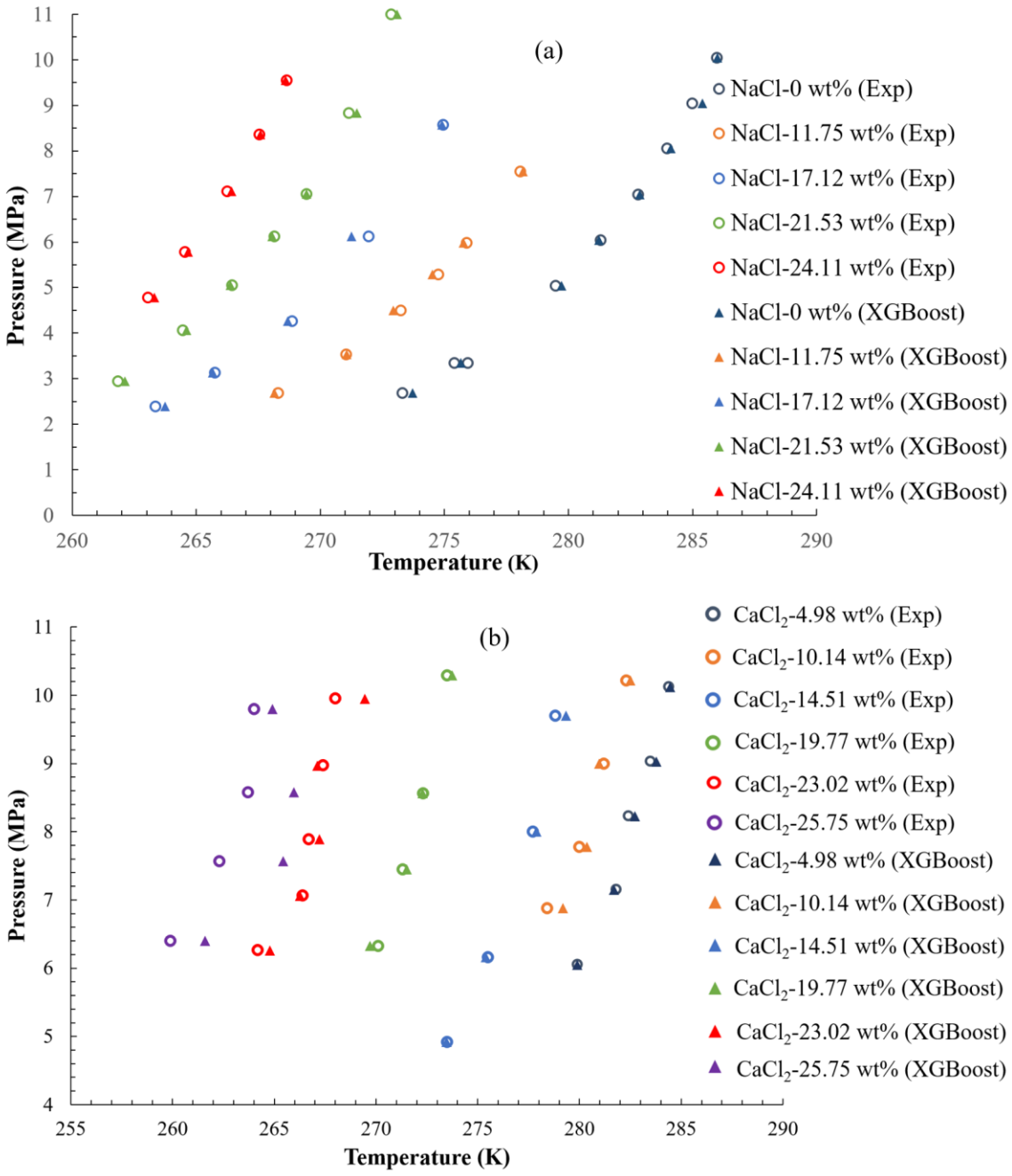

Figure 5.4. Pressure-Temperature data associated with the formation of methane hydrates in the presence of (a) NaCl and (b) $CaCl_2$ (varying weight percentages). Solid symbols represent the predictions from XGBoost model, while non-solid symbols represent experimental data [185], [189].

Finally, the predicted HDTs (from Random Forest, Extra Trees and XGBoost algorithms) and the relative errors against experimental data reported in two detailed studies, are discussed. The first study was by Dholabhai and Bishnoi [180], who studied hydrate formation in a mixture of CO_2 and CH_4 of varying compositions in the presence of various salts in water at varying weight percentages as outlined in Table 5.3. It is evident that while all the three ML models capture the hydrate forming conditions reasonably well (low error), the relative error exhibited by XGBoost is less than that of Random Forest (RF) and Extra Trees (ET) in most cases. The overall relative error predicted using XGBoost is predominantly less than 0.1% for most of the data points in Table 5.3. While the relative error of XGBoost is lesser than Random Forest and Extra Trees in a vast majority of the dataset, there are very few exceptions (CO_2/CH_4 at 16.1/83.9 mol% with 5.02 wt% NaCl; CO_2/CH_4 at 19.7/80.3 mol% with 9.91 wt% $CaCl_2$) where ET or RF exhibit slightly better performance. The highest relative errors occur for a gas composition consisting of CO_2/CH_4 at 49.7/50.3 mol% with NaCl and $CaCl_2$ at 10 wt% each.

Table 5.3 Comparison between predictions (3 ML models) and experimental data [47] for hydrate formation under varying salt concentrations.

Gas composition (mol%)		**Salt composition (wt%)**			**Experiments**		**Prediction**			**Relative error (%)**		
CO_2	**CH_4**	**NaCl**	**KCl**	**$CaCl_2$**	**P (MPa)**	**T (K)**	**RF**	**ET**	**XGBoost**	**RF**	**ET**	**XGBoost**
15.3	84.7	0	0	0	3.41	277.6	277.8	277.5	277.5	0.08	-0.02	-0.01
16.7	83.3	0	0	0	5.14	281.5	280.8	280.7	281.5	-0.24	-0.28	0.00
16.4	83.6	0	0	0	2.36	274.1	276.0	274.5	274.0	0.70	0.15	-0.03
17.9	82.1	0	0	0	7.53	284.8	284.6	283.9	284.7	-0.07	-0.32	-0.04
17.7	82.3	5.02	0	0	6.98	282.0	281.4	281.3	282.1	-0.23	-0.24	0.03
17.2	82.8	5.02	0	0	5.08	279.2	278.6	278.6	279.1	-0.23	-0.22	-0.06
16.1	83.9	5.02	0	0	3.26	275.0	273.0	274.2	273.5	-0.72	-0.30	-0.54
15.2	84.8	5.02	0	0	2.3	271.6	271.9	272.4	271.1	0.13	0.30	-0.17

Table 5.3 (continued)

17.4	82.6	9.99	0	0	6.56	279.0	277.9	278.6	279.1	-0.38	-0.15	0.02
16.1	83.9	9.99	0	0	3.1	272.1	271.2	272.1	272.0	-0.32	0.00	-0.04
19.4	80.6	9.99	0	0	4.66	276.1	275.1	275.4	276.2	-0.37	-0.29	0.01
19.3	80.7	9.99	0	0	2.03	268.5	268.8	269.5	268.4	0.14	0.37	-0.01
18.9	81.1	15	0	0	7.31	277.2	275.5	275.7	277.2	-0.59	-0.53	0.03
19.4	80.6	15	0	0	2.88	269.1	268.8	269.3	268.9	-0.10	0.08	-0.08
18.2	81.8	15	0	0	7.37	276.8	276.1	276.6	276.9	-0.27	-0.09	0.05
19.8	80.2	15	0	0	4.4	273.1	272.2	272.8	273.2	-0.35	-0.14	0.03
17.3	82.7	15	0	0	1.86	264.8	266.2	266.3	264.7	0.54	0.56	-0.03
19.3	80.7	20	0	0	5.42	270.4	272.0	272.6	269.6	0.60	0.80	-0.27
19.1	80.9	20	0	0	2.12	262.0	264.0	263.2	262.2	0.80	0.48	0.08
19.8	80.2	20	0	0	3.86	267.5	267.7	267.5	267.3	0.09	0.01	-0.06
19.9	80.1	20.01	0	0	9.15	274.3	274.6	274.4	274.3	0.09	0.04	-0.01
19.7	80.3	0	5	0	2.04	271.4	272.1	271.7	271.5	0.28	0.11	0.04
19.8	80.2	0	5	0	4.46	278.8	278.0	278.3	278.6	-0.28	-0.19	-0.08
19.8	80.2	0	5	0	2.96	275.0	274.1	274.5	274.6	-0.31	-0.17	-0.12
19.8	80.2	0	5	0	6.43	282.0	281.4	281.5	282.0	-0.21	-0.18	0.00
19.6	80.4	0	10	0	3.94	275.9	274.3	274.9	275.7	-0.57	-0.35	-0.09
19.7	80.3	0	10	0	1.83	269.2	269.5	269.9	269.3	0.12	0.26	0.03
19.8	80.2	0	10	0	2.59	272.2	271.3	272.0	272.2	-0.32	-0.07	0.01
19.8	80.2	0	10	0	5.66	279.0	277.5	278.6	278.9	-0.52	-0.14	-0.02
18.4	81.6	0	15	0	1.89	267.0	267.3	268.3	266.8	0.12	0.50	-0.06
19	81	0	15	0	2.62	270.1	269.3	270.2	270.2	-0.27	0.06	0.04
19.5	80.5	0	15	0	3.45	272.7	271.2	272.0	272.9	-0.54	-0.26	0.07
19.7	80.3	0	15	0	5.63	277.1	274.8	276.2	277.0	-0.81	-0.33	-0.01
18.7	81.3	0	0	9.91	1.96	268.6	270.0	270.0	268.8	0.51	0.53	0.07
19.7	80.3	0	0	9.91	4.32	276.0	276.0	275.9	275.8	-0.03	-0.05	-0.07
19.4	80.6	0	0	9.91	2.8	272.0	272.0	272.0	271.9	-0.01	0.00	-0.03
19.7	80.3	0	0	9.91	6.08	279.1	279.4	278.9	279.7	0.08	-0.08	0.20
19	81	0	0	15	4.61	273.1	273.5	273.4	273.3	0.14	0.10	0.05
19.7	80.3	0	0	15	3	269.1	269.4	270.4	269.2	0.10	0.47	0.02
19.6	80.4	0	0	15	1.88	266.7	267.8	268.5	266.4	0.43	0.67	-0.08
19.7	80.3	0	0	15	7.09	276.9	276.8	278.2	277.9	-0.04	0.47	0.36
19.8	80.2	0	0	20	2.89	263.8	266.1	267.3	264.1	0.86	1.32	0.11
19.9	80.1	0	0	20	7.24	271.3	272.9	272.3	271.6	0.58	0.34	0.08
19.8	80.2	0	0	20	4.3	267.6	269.4	269.7	267.6	0.67	0.78	-0.02
19.9	80.1	0	0	20	9.46	273.7	275.0	274.1	273.8	0.46	0.16	0.04

Table 5.3 (continued)

19.6	80.4	0	0	15	1.88	266.7	267.8	268.5	266.4	0.43	0.67	-0.08
19.7	80.3	0	0	15	7.09	276.9	276.8	278.2	277.9	-0.04	0.47	0.36
19.8	80.2	0	0	20	2.89	263.8	266.1	267.3	264.1	0.86	1.32	0.11
19.9	80.1	0	0	20	7.24	271.3	272.9	272.3	271.6	0.58	0.34	0.08
19.8	80.2	0	0	20	4.3	267.6	269.4	269.7	267.6	0.67	0.78	-0.02
19.9	80.1	0	0	20	9.46	273.7	275.0	274.1	273.8	0.46	0.16	0.04
19.4	80.6	5.01	0	10	5.04	273.7	273.9	274.1	273.7	0.08	0.15	0.00
19.8	80.2	5.01	0	10	3.12	269.4	268.8	269.8	269.4	-0.20	0.18	0.02
19.7	80.3	5.01	0	10	2.06	265.5	267.3	269.1	266.4	0.68	1.34	0.32
19.9	80.1	5.01	0	10	7.14	276.7	275.4	276.8	276.3	-0.49	0.01	-0.15
19.8	80.2	0	10	5	1.65	265.1	266.2	266.9	265.1	0.41	0.69	0.03
19.9	80.1	0	10	5	4.6	274.8	273.7	274.2	274.7	-0.38	-0.20	-0.04
19.8	80.2	0	10	5	2.46	269.4	268.5	269.7	269.0	-0.31	0.12	-0.13
19.9	80.1	0	10	5	10.61	281.6	279.5	281.1	281.6	-0.74	-0.16	0.03
19.2	80.8	5	10	0	2.59	269.3	269.0	269.6	269.4	-0.09	0.13	0.03
19.8	80.2	5	10	0	10.41	281.3	278.3	279.3	281.2	-1.04	-0.72	-0.02
19.7	80.3	5	10	0	4.99	275.2	274.5	274.9	275.4	-0.27	-0.10	0.07
20.3	79.7	5	10	0	1.66	265.1	266.7	267.1	265.9	0.60	0.74	0.29
19.5	80.5	10.17	0	5.08	6.07	275.1	275.0	275.3	275.0	-0.06	0.06	-0.05
20.1	79.9	10.17	0	5.08	2.11	266.5	267.0	267.6	266.1	0.19	0.41	-0.16
20	80	10.17	0	5.08	3.1	269.2	269.1	269.5	269.1	-0.04	0.12	-0.04
19.4	80.6	10.17	0	5.08	9.71	278.7	277.2	278.8	278.3	-0.54	0.04	-0.14
48.6	51.4	10	0	10	3.53	268.1	269.2	268.5	268.4	0.40	0.17	0.11
49.7	50.3	10	0	10	2.15	264.1	268.7	269.5	266.1	1.73	2.02	0.75
49.4	50.6	10	0	10	5.16	270.8	271.4	271.2	271.1	0.21	0.13	0.11
49.7	50.3	10	0	10	3.52	268.2	269.4	269.6	269.0	0.44	0.51	0.28
46.5	53.5	10	5	0	4.59	275.5	273.6	275.2	275.4	-0.69	-0.09	-0.03
49.5	50.5	10	5	0	2.78	271.6	270.4	271.6	271.4	-0.44	-0.01	-0.05
49.8	50.2	10	5	0	1.82	268.0	268.1	268.6	267.7	0.01	0.19	-0.13
50	50	10	5	0	1.38	265.8	266.8	266.5	266.0	0.41	0.28	0.08

The second study against which the ML-based predictions are benchmarked is by Nixdorf and Oellrich [198], who studied hydrate dissociation conditions for various binary and ternary gas mixtures. The highest relative errors are observed for data points containing CH_4/C_3H_8 at 97.07/2.93 mol%, respectively. One of the primary reasons underlying the poor prediction performance is the lack of data points at lower temperatures (247-261K) over which these data points have been evaluated. Furthermore, the relative error increases slightly for predictions by Random Forest model when a third gas component is introduced.

Table 5.4 Comparison between predictions (3 ML models) and experimental data [186] for hydrate formation from binary and ternary gas mixtures

Gas composition (mol%)	**Experiments**		**Prediction**			**Relative error (%)**		
	P (MPa)	**T (K)**	**RF**	**ET**	**XGBoost**	**RF**	**ET**	**XGBoost**
CH_4: 89.26 N_2: 10.74	4.94	278.7	279.2	278.6	278.9	0.18	-0.04	0.09
	6.94	282.0	282.1	281.2	282.0	0.02	-0.28	-0.02
	10.4	285.6	285.9	285.0	285.8	0.07	-0.22	0.05
	14.98	288.7	288.5	288.4	288.5	-0.05	-0.10	-0.07
	20.02	291.0	291.0	290.6	290.9	0.02	-0.12	-0.04
	24.43	292.4	292.1	292.1	292.5	-0.12	-0.11	0.01
CH_4: 90.47 C_2H_6: 9.53	2.25	278.2	277.8	277.8	278.1	-0.14	-0.17	-0.06
	2.63	279.6	279.0	278.9	279.8	-0.21	-0.24	0.08
	4.19	283.7	283.1	282.7	283.4	-0.22	-0.34	-0.09
	7.21	288.1	287.4	287.3	288.1	-0.26	-0.29	-0.02
	9.99	290.4	290.1	290.3	290.4	-0.11	-0.05	-0.01
	14.85	293.0	292.4	292.3	292.8	-0.19	-0.21	-0.05
	19.89	294.6	294.3	294.6	294.6	-0.13	-0.02	-0.03
	23.2	295.5	294.7	294.5	295.5	-0.29	-0.34	0.01
CH_4: 97.07 C_3H_8: 2.93	2.64	247.5	262.3	260.3	250.3	5.99	5.17	1.12
	9.2	256.9	265.8	258.6	257.3	3.46	0.66	0.18
	14.97	259.3	265.2	260.1	258.6	2.26	0.31	-0.28
	19.81	260.6	265.0	260.6	260.1	1.68	0.00	-0.20
	24.36	261.5	268.5	261.5	262.0	2.68	0.00	0.16

Table 5.4 (continued)

CH_4: 94.97 N_2: 0.03	3.45	276.9	278.4	277.1	277.4	0.55	0.08	0.18
	4.87	280.0	280.2	279.9	279.9	0.10	-0.04	-0.03
	7.04	283.5	283.8	283.3	283.5	0.11	-0.07	0.01
	10.94	287.4	288.3	287.2	287.5	0.29	-0.08	0.03
	16.83	290.8	290.9	290.5	290.7	0.06	-0.10	-0.02
	23.98	293.4	292.9	293.4	293.2	-0.19	0.00	-0.06
C_2H_6: 85.15 C_3H_8: 14.85	0.83	276.7	277.0	276.3	276.9	0.12	-0.12	0.08
	1.09	278.9	278.7	278.9	278.9	-0.08	-0.01	0.00
	1.51	281.5	281.4	281.4	281.5	-0.05	-0.02	0.01
	1.94	283.3	282.8	282.9	283.3	-0.20	-0.16	-0.03
	1.12	279.1	278.9	279.0	279.0	-0.09	-0.03	-0.04
	1.5	281.4	281.3	281.3	281.5	-0.02	-0.04	0.04
CH_4: 90.93 C_2H_6: 4.89	2.58	277.4	277.3	277.2	277.2	-0.03	-0.08	-0.05
	3.8	280.9	280.4	279.7	280.8	-0.20	-0.43	-0.06
	6.1	284.9	284.6	284.6	284.9	-0.12	-0.10	0.01
	8.36	287.5	287.1	287.2	287.3	-0.11	-0.08	-0.04
	13.81	290.9	290.6	290.6	290.9	-0.12	-0.11	-0.01
	18.82	292.8	292.8	292.6	292.8	-0.02	-0.09	-0.01
	23.83	294.2	293.7	294.2	294.2	-0.18	0.00	-0.01
CH_4: 84.52 C_2H_6: 12.55 C_3H_8: 2.93	1.2	277.1	277.2	277.1	277.0	0.04	-0.01	-0.05
	1.98	281.6	279.9	280.8	281.7	-0.59	-0.29	0.04
	4	287.4	285.9	287.0	287.6	-0.53	-0.14	0.06
	6.92	291.5	290.0	291.5	291.6	-0.51	0.00	0.02
	11.21	294.3	292.7	294.3	294.1	-0.54	0.00	-0.08
	17.03	296.1	294.7	296.1	296.5	-0.49	0.00	0.13
	24.47	298.1	296.0	298.1	298.0	-0.72	0.00	-0.05
CH_4: 95.02 C_2H_6: 3.98 C_3H_8: 1	2.16	279.1	275.3	276.4	275.7	-1.35	-0.98	-1.23
	3.99	284.3	282.2	282.9	284.0	-0.73	-0.49	-0.10
	6.96	288.6	287.0	288.2	288.5	-0.55	-0.12	-0.02
	10.94	291.6	290.1	291.5	291.5	-0.52	-0.02	-0.02
	17.36	294.0	292.3	294.0	294.2	-0.58	0.00	0.04
	24.15	295.8	293.9	295.8	295.8	-0.64	0.00	0.01
CO_2: 8.09 CH_4: 89.4 C_3H_8: 2.49 N_2: 0.02	1.69	279.2	277.5	278.4	279.0	-0.61	-0.27	-0.08
	3.47	285.1	282.3	283.9	285.0	-0.97	-0.44	-0.02
	6.91	290.2	287.3	289.5	290.2	-0.99	-0.23	0.02
	10.47	292.6	289.3	292.2	292.5	-1.13	-0.11	-0.03
	16.95	294.6	289.7	294.6	294.7	-1.68	-0.02	0.02
	23.57	296.1	283.0	281.9	289.5	-4.40	-4.80	-2.23

Table 5.4 (continued)

CO_2: 5.25 CH_4: 89.6 C_3H_8: 5.13 N_2: 0.02	2.96	279.0	278.6	278.3	279.0	-0.16	-0.27	-0.02
	5	283.5	282.8	282.8	283.4	-0.26	-0.25	-0.07
	7.74	287.1	286.9	287.0	287.0	-0.06	-0.04	-0.03
	11.88	290.0	289.8	289.9	290.0	-0.07	-0.06	0.00
	17.52	292.3	292.4	290.8	293.0	0.03	-0.50	0.25
	24.33	294.2	293.9	294.2	294.4	-0.12	0.00	0.06

5.5 CONCLUSIONS

In summary, a set of thermodynamic features such as partial pressures, specific gravity of hydrate precursor mixtures and the activity contribution due to salts were used in three ML-based models to predict HDTs. Using such physics-based features in ML frameworks enables the models to track individual contributions of gases towards hydrate formation. Importantly, it extends the utility of the model to predict the inhibition effect for any other salt via the calculation of an activity term. An extensive databank comprising more than 1800 experimental data points was employed to train and evaluate the prediction accuracies of the ML models. While the use of Random Forest (RF) and Extra Trees (ET) has been reported previously, extreme gradient boosting (XGBoost) has been used to predict hydrate equilibria for the first time and a considerable improvement in prediction accuracies is observed when compared to RF and ET. The overall coefficient of determination (R^2) percentage is greater than 97%, and the overall average absolute relative deviation (AARD) is lower than 0.25% for all three models. XGBoost exhibits the highest R^2 accuracy and the lowest AARD for training and test data, highlighting its superior ability to predict hydrate equilibrium conditions.

Chapter 6: Techno-economic analysis of hydrates-based carbon capture system for landfill gases in Texas

This chapter analyzes the techno-economic factors associated with the production of blue H_2, and hydrates-based capturing of CO_2 produced by sorption-enhanced steam methane reforming (SESMR) of methane from landfill gas (LFG) across various counties in Texas. Landfills account for ~18% of the greenhouse gas emissions in the US, and SMR converts CH_4 in LFG into CO_2 (which is a less potent greenhouse gas) and hydrogen (that can be used as fuel). The utility of CO_2 hydrates as an effective carbon capture and sequestration tool stems from its high storage capacity, mild to moderate formation conditions (requiring less storage energy than more energy-intensive liquefaction processes), and long-duration stable storage in the form of solids.

In order to evaluate the techno-economics underlying the SESMR process, results from previously reported ASPEN simulations are adopted for estimating hydrogen and carbon dioxide yields based on the amount of LFG in various counties. Subsequently, the capital and operating costs are scaled up depending upon the hydrogen production capacity. The cost of producing hydrogen (without the carbon capture system) from this analysis is estimated at \$0.5/kg of H_2 (remaining more or less constant for all the counties considered in the present study) and increases to \$1.5/kg of H_2 when the cost of natural gas is factored in the analysis.

Additionally, the SESMR system is coupled with a hydrates-based carbon capture system, and the energy and cost of setting up and running such a hydrates-centered capture facility have been estimated. In doing so, the amount of water required, energy required to compress and refrigerate the gas down to hydrate forming conditions, and the capital and operating costs involved in setting up and running such a facility are evaluated in detail. The total cost (CAPEX+OPEX) for capturing one metric ton of CO_2

ranges from $96 (Harris county) to $145 (Brazoria county), demonstrating that the cost goes down as the production capacity scales up. Interestingly, the addition of tetrabutylammonium bromide (TBAB) to the hydrate precursor mixture to achieve favorable thermodynamic formation conditions increases the overall cost ($107-$137/metric ton of CO_2 captured). This can be attributed to the increased water requirement necessitating a higher number of reactors, higher refrigeration capacity, and labor costs.

Additional analysis was carried out to estimate the minimum hydrogen cost required to result in a positive combined net present value (NPV) for a coupled SESMR + hydrate-based carbon capture system for a 30-year project duration. This cost turns out to be $0.9/kg and $2.4/kg of H_2 for Harris and Brazoria county, respectively. Furthermore, a 5-year payback period would require a minimum cost corresponding to $1.35/kg (Harris) and $4.95/kg (Brazoria) of H_2, demonstrating that the coupled system would be economical only for counties that have a significant hydrogen production potential.

6.1 TECHNICAL ANALYSIS

6.1.1 LFG data

The landfill methane outreach program (LMOP) database contains data on the location and the amount of landfill gas (LFG) collected for more than 2600 municipal solid waste landfills; this can be accessed from the EPA website [217]. This databank (as outlined in Table 6.1) is used to estimate the amount of LFG collected across various counties (that have a functioning landfill site and an active gas collection system in place) across Texas. For the present analysis, the top 10 counties collecting about 75% of the total LFG in Texas (4.5 million m^3/day) have been considered.

Table 6.1 Details of landfills and the amount of gas collected across different counties in Texas. Data obtained from EPA website [217].

Sr no	County	Landfill ID	LFG collected (MMSCFD)
1	Harris	1479	9.05
		1465	13.82
		1811	1.18
2	Dallas	11761	2.61
		1475	1.08
		1459	11.38
		1456	5.68
3	Bexar	1509	9.19
		1820	6.59
4	Fort Bend	1812	10.49
		12101	5.08
5	Denton	1480	2.84
		1805	1.29
		1461	9.10
6	Tarrant	1467	4.13
		1463	3.43
7	Galveston	1808	2.77
		1810	3.96
8	Collin	12201	5.87
	Travis	1464	4.32
9		1511	1.33
10	Brazoria	1497	3.87

6.1.2 Sorption enhanced steam methane reforming

Steam methane reforming is a very commonly used procedure for generating hydrogen from methane (termed as blue hydrogen when paired with a carbon capture system) and currently accounts for about 48% of the hydrogen that is produced globally [218], [219]. The hydrogen produced from the SMR reaction can be used in fuel cells to generate electricity for a wide range of applications, including transportation, in refineries for hydrocracking and hydro-desulfurization (HDS) operations, and production of

fertilizers. However, SMR results in significant CO_2 emissions, which is addressed in the present analysis by coupling the sorption enhanced membrane reactor (SESMR) system with a hydrates-based carbon capture system, as illustrated in Figure 6.1.

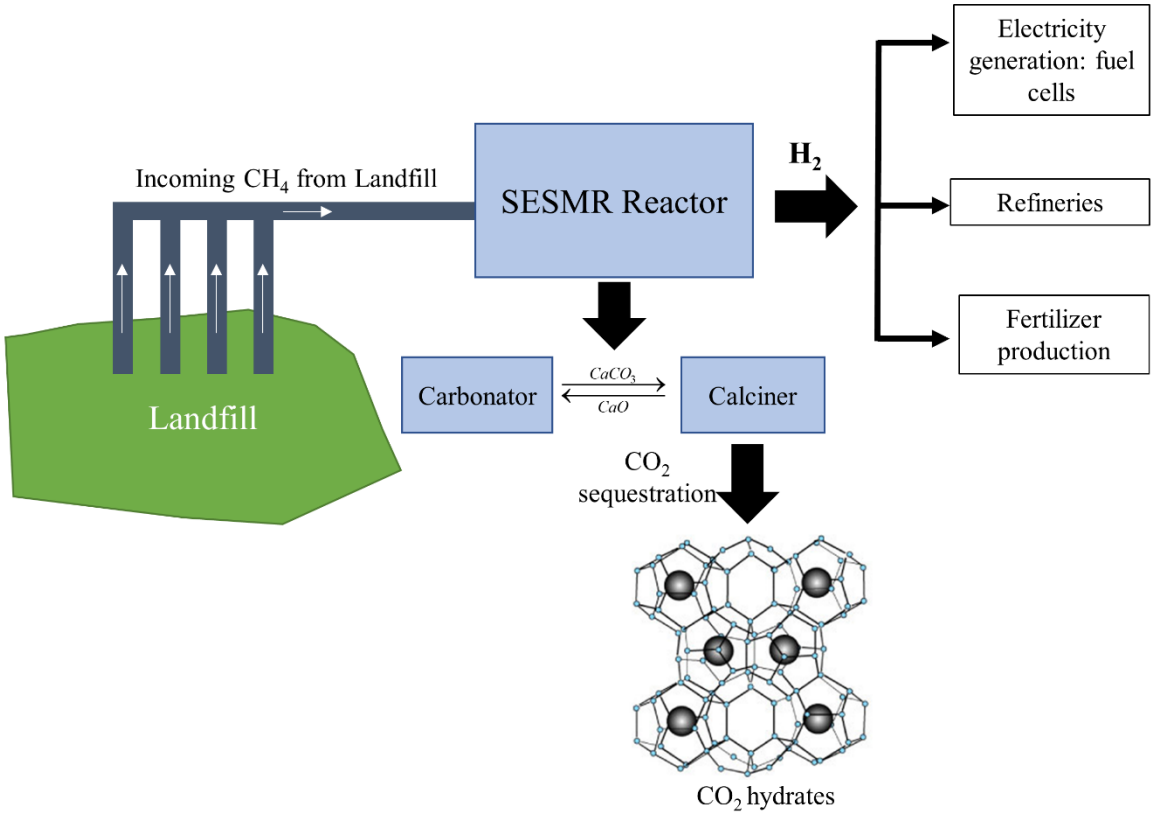

Figure 6.1 Illustrative concept of LFG-based blue hydrogen generation via SESMR and CO_2 capture via hydrates.

The chemical reactions taking place during a typical SESMR process are:

$$CH_4 + H_2O \rightarrow CO + 3H_2 \quad \Delta H^0_{298} = 206 kJmol^{-1} \tag{6.1}$$

$$CO + H_2O \rightarrow CO_2 + H_2 \quad \Delta H^0_{298} = -41 kJmol^{-1} \tag{6.2}$$

$$CH_4 + 2H_2O \rightarrow CO_2 + 4H_2 \quad \Delta H^0_{298} = 165 kJmol^{-1} \tag{6.3}$$

$$CO_2 + CaO \rightarrow CaCO_3 \quad \Delta H^0_{298} = -177.9 kJmol^{-1} \tag{6.4}$$

Sorption enhanced reforming reaction is a technique that simultaneously produces hydrogen while capturing carbon dioxide and includes catalytic SMR, water gas shift and a CO_2 chemical sorption system using a solid sorbent that aids in improving hydrogen production yields. The carbon dioxide produced during the reaction is captured using CaO adsorbent in a carbonator which is regenerated back in a calciner. In the present analysis, this system is coupled with a CO_2 hydrates-based CCS system wherein the CO_2 emitted by the calciner is further processed to be captured in the form of hydrates. In order to evaluate the amount of CO_2 and H_2 that can be produced via SMR of landfill gases in Texas, results from a previously reported ASPEN Plus process simulation [220] have been used. In this study, production yields of 1.2 mol H_2/mol CH_4 and 0.2 mol CO_2/mol CH_4 have been reported at a process temperature of 773K [220].

6.1.3 Hydrates-based carbon capture

The CO_2 emitted by the calciner could either be collected and stored in tanks following which it has to be subjected to a compression and refrigeration process along with water in order to store it in the form of hydrates. To estimate the amount of water required to convert this CO_2 into hydrate, gas uptake capacity, as reported in the work of Mohammadi and Jodat [221], has been used. It was observed that at a thermodynamic formation condition of 3.2 MPa and 276.15 K, a gas uptake capacity of about 60 mmol of gas/mol of water was obtained at about 120 mins which is one of the best in class reported values. It is noted that the maximum theoretical uptake rate that can be obtained for CO_2 hydrates, assuming that all the cages will be occupied, is about 174 mmol of gas/mol of water. However, the numbers achieved in practical conditions are lower than this value due to inefficient cage filling process during hydrate formation. The present analysis assumes that CO_2 capture via hydrate formation will occur as batch processes

comprising two hours each. A duration of two hours was used since the hydrate formation rate was observed to saturate around this time [221].

6.1.4 Energetics of hydrate formation process: Compression

The calculation procedure to compress the gas to CO_2 hydrate forming conditions (3.2 MPa and 3 ^oC) is detailed in this section. A compression time of ten minutes is assumed to compress the gas available in two hours from atmospheric pressure (it is assumed that the collected gas will be available at ambient pressure and temperature conditions) to 3.2 MPa. The compression time has been decided while considering the inlet flow rate constraints for a centrifugal compressor. The compression head (H_{is}) is calculated using [222]:

$$H_{is} = \frac{R}{M}\frac{Z_{avg}T_1}{(k-1)/k}\left[\left(\frac{p_2}{p_1}\right)^{\frac{k-1}{k}} - 1\right] \tag{6.5}$$

In the above equation, R is the universal gas constant 8.314 kJ/(kmol.K), M is the molecular mass in kg/kmol, Z_{avg} is the average compressibility factor (Z_s+Z_d/2) evaluated at the suction and discharge conditions using Peng-Robinson equation of state, T is the absolute temperature in K, k is the isentropic exponent (C_p/C_v) and p is the absolute pressure in kPa. An isentropic compression process with an isentropic efficiency (η_s) of 0.83 has been used to evaluate the actual compression power (Ghp) in kW as a function of the inlet mass flow rate (w) and compression head (H_{is}) using:

$$Ghp = \frac{wH_{is}}{3600\eta_{is}} \tag{6.6}$$

The inlet mass flow rate is evaluated using:

$$w = \frac{QMp_1}{8.314 T_1 Z_1} \tag{6.7}$$

In the above equation, Q is the inlet volumetric flow rate in m^3/h.

Since the gas in the present analysis has to be compressed to very high hydrate forming pressures (translating to a very high overall compression ratio), the compression process is carried out in multiple stages based on the guidelines for designing compressors as detailed ahead [222]:

1. The overall compression ratio is divided into an equal number of stages such that the compression ratio per stage is lesser than four (r<4) while considering intercooler pressure loss (10 psi).
2. At the end of every stage, the outlet pressure and temperature are evaluated for the calculated compression ratio assuming an isentropic process (η_s=0.83).
3. The compression power per stage is calculated using equations 6.5 and 6.6.
4. The gas will be subjected to an intercooling process to bring the temperature at the discharge stage down to ambient conditions before it enters the next stage.
5. The electrical energy requirements are evaluated using a COP of 4.

Figure 6.2 illustrates the multistage compression process adopted for compressing the gas to 3.2 MPa in the present study.

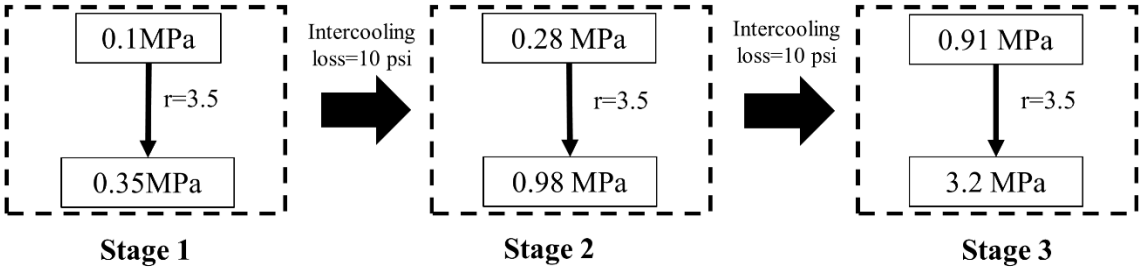

Figure 6.2. Three-stage compression process for compressing the gas to hydrate forming conditions (3.2 MPa).

6.1.5 Energetics of hydrate formation process: Refrigeration

Refrigeration energy accounts for the energy required to cool the reactor down to hydrate formation temperatures (considered as 3 ^{o}C in the present study). This occurs in three stages: Stage 1 consists of sensible heating, the energy required to bring the reactor vessel + water + gas mixture to hydrate forming temperatures (HFT). Stage 2 comprises the dissociation energy, which accounts for the latent heat released when the water molecules rearrange to form solid hydrate structures in the reactor vessel. Stage 3 is related to the energy required to maintain the system at HFT, which would account for the heat losses in the system.

In order to evaluate the energy required for sensible cooling, it is crucial to determine the reactor volume and thickness that would contribute to the thermal mass of the system. To do so, it is assumed that the maximum diameter and height of the reactor is 3m and 6m (aspect ratio=2), respectively, and in cases where the volume of CO_2 + water exceeds this volume, a system of parallel reactors would be used. It is noted that the reactor dimensions are similar to the one used in a previous study analyzing CO_2 capture by hydrate formation for gas emission in the steelmaking industry [223]. The reactor wall thickness should be sufficient to withstand hoop and longitudinal stresses for the working design pressures (considered as 10 MPa, which is three times the hydrate forming pressures considered in this study). Accordingly, the wall thickness was evaluated using the following equation as per ASME Section VIII, paragraph UG-27 (used for calculating the thickness of thin-walled pressure vessels):

$$t_1 = \frac{PD}{2SE - 1.2P} \tag{6.8}$$

$$t_2 = \frac{PD}{4SE + 0.8P} \tag{6.9}$$

In the above equations, t_1 and t_2 are the thicknesses corresponding to longitudinal and circumferential stresses, respectively. P is the pressure (design pressure=10 MPa), D is the diameter, S is the maximum allowable stress for the reactor material (considered as T316 SS in this study), and E is the welded joint efficiency. The thicker value of the two is taken as the wall thickness, and 0.125 inches is added to this value to account for corrosion over time as per standard practice. Welding factor (E) is 1 and 0.85 for a seamless and welded pipe, respectively. While evaluating S, a safety factor of 4 has been assumed, so the maximum allowable stress for the reactor material is $1/4^{th}$ times the maximum tensile strength (T_{max}) for reactor material (T_{max} for T316SS typically lies around 80,000 psi).

Once the reactor dimensions and the amount of water + gas in each system are determined, the number of reactors required for every county and the sensible energy required to bring this system down to hydrate forming temperatures is evaluated. Heat losses are calculated for this reactor system using a thermal resistance circuit analogy and assuming a natural convection boundary condition around the reactor walls. Dissociation energy is evaluated using a value of 60kJ/mol [224] for CO_2 hydrates. The final refrigeration energy is evaluated by summing up the sensible and dissociation heat requirements and heat losses; the electrical energy is evaluated using a COP of 4.

6.2 Economic Analysis

The economic analysis was carried out using an itemized cost estimation to evaluate the unit production cost ($/kg$H_2$) for the SESMR and carbon capture cost ($/metric ton of CO_2) for the hydrates-based carbon capture facility. The economics for setting up and running the facility were classified as capital expenditure (CAPEX) and operating expenditure (OPEX), respectively.

The capital cost and the operating cost for the SESMR process have been adopted from the work of Lee et al. [220], wherein a detailed techno-economic investigation was carried out using an Aspen plus process simulation and itemized cost estimation. CAPEX consists of the equipment costs involved in each process. For the SESMR process, the capital costs include the reactor, compressor, carbonator, calciner and supplement cost (assumed as 20% of the total CAPEX in this analysis). The operating cost includes electricity, labor, membrane, maintenance and other costs. In order to scale up the CAPEX, an exponent of 0.6 is used with the annual hydrogen production capacity (six-tenth rule), whereas operating cost is assumed to increase proportionally with the production capacity [220]. It is noted that the values for electricity cost, discount rate and project year to estimate the annual CAPEX and OPEX used in the analysis of Lee et al. [220] have been modified to reflect the cost of electricity in Texas and the discount rate and project year used in the present analysis.

An itemized cost estimation for evaluating the capital cost for a hydrates-based carbon capture system would include compressors, reactors, refrigeration systems and supplement cost (assumed as 20% of the total CAPEX). The investment cost for the compressors is estimated using the following Douglas correlation [225]:

$$\text{Cost} = \left(\frac{M\,\&\,S}{280} \right) 517.5 \left(bhp \right)^{0.82} \left(2.11 + F_c \right) \tag{6.10}$$

In the above equation, M&S is the Marshall and Swift equipment cost index (2171.6 for 2020), bhp is the brake horsepower and F_c is the correction factor equal to 1.15 for a centrifugal compressor [223].

The investment cost for the reactor (pressure vessel) is estimated using the following [225]:

$$\text{Cost} = \left(\frac{M\,\&\,S}{280}\right) 101.9 D^{1.066} H^{0.802} \left(2.18 + F_c\right) \tag{6.11}$$

In the above equation, D and H are the diameter and height of the reactor vessel (in feet), respectively. F_c is the correction factor for pressure vessel reactors, which would depend on the material of the vessel and the operating pressure. In order to estimate the capital cost of refrigeration systems, values reported in the work of Luyben [226] for a single-stage ammonia-based refrigeration system have been used, and a scaling factor of 0.6 with the refrigeration load has been used to scale up the capital cost for industrial-scale systems considered in the present study.

To convert the capital cost into an annual cost, it has to be multiplied by a capital recovery factor (CRF). In order to evaluate the CRF, a discount rate of 10% was used, which is consistent with established practices on valuations of energy and water-related projects [227], [228]. A project period of 30 years was used, which is consistent with the 3+ decades of steady emissions from landfills [228], [229]. Accordingly, a capital recovery factor of 0.106 was used to evaluate the annual capital cost/metric ton of CO_2 captured, as per the following:

$$Capital\ cost \left[\frac{\$}{metric\ ton_{CO_2}}\right] = \frac{CRF\ x\ Total\ Capital\ cost}{Amount\ of\ CO_2\ produced\ annually} \tag{6.12}$$

An average electricity price of \$22/MWh (based on the average wholesale electricity price in 2020 (as per EIA data) [230]) was used to evaluate the operating electrical energy costs for compression and refrigeration processes. Maintenance and other costs were assumed to be 2% and 1% of the total CAPEX, respectively [220]. To evaluate the labor cost for the hydrates-based capture system, it was assumed that one operator could handle two machines and a labor rate of \$20/hr was used [231].

The overall unit cost for the production/capture system was evaluated using the following:

$$Unit\ gas\ capture/production\ cost = \frac{\sum_i CAPEX_i\left(\$y^{-1}\right)+\sum_j OPEX_i\left(\$y^{-1}\right)}{Amount\ of\ gas\ produced/captured\ annually} \quad (6.13)$$

The overall economics of combining an SESMR system with a hydrates-based carbon capture system have been evaluated using two commonly used metrics: PayBack Period (PBP) and Net Present Value (NPV). NPV is a measure of the time-adjusted returns from a project, whereas PBP provides the time required to recover the investment in a project. The NPV of the combined SESMR+CCS can be evaluated using the following:

$$NPV = \sum_{j=1}^{n} \frac{I_{t=j}}{(1+r)^j} - \left[C_0 + \sum_{j=1}^{n} \frac{OC_{t=j}}{(1+r)^j}\right] \quad (6.14)$$

In the above equation, I is the income that could be obtained via hydrogen every year, r is the discount rate, n is the project period, C_0 is the capital expenditure and OC is the operating cost. Payback period can be obtained from the time when NPV becomes equal to 0. A net positive NPV indicates that the projected earnings for a project is higher than the anticipated costs in present dollars. It is assumed that positive and negative NPV values indicate investments that would be profitable and those that would incur a net loss, respectively. Higher values of NPV indicates a higher value for a particular long-term investment whereas a shorter PBP is indicative of a shorter payback or breakeven period.

6.2 RESULTS AND DISCUSSIONS

Figure 6.3 illustrates the amount of CO_2 and H_2 (in million metric tons) that can be captured/produced via steam methane reforming of LFG collected from the top 10

counties in Texas. The highest CO_2 capture and H_2 production potentials are for Harris County, which generates the highest amount of landfill gas (Table 6.1), yielding about 0.05 and 0.01 million metric tons of CO_2 and H_2 every year. The collective annual CO_2 capture and H_2 production potential for all the counties are about 0.24 and 0.07 million metric tons, respectively. It is noted that the amount of CO_2 captured via SMR of LFG in Texas is a small percentage of the annual CO_2 emissions in the United States, amounting to about 5256 million metric tons in 2019 [232].

The collective amount of hydrogen produced from the top 10 landfills collecting counties in Texas, when used in a fuel cell with 60% efficiency (HHV=39.7 kWh/kg), would produce enough energy (~160 GWh) to power about 15,000 homes every year based on the average annual electricity consumption for a US residential utility customer in 2020 [233]. A preliminary techno-economic analysis for the SESMR technology in Texas suggests a hydrogen production cost of \$0.5/kg of H_2 for all the counties considered in the present analysis. It is noted that this does not include the cost of natural gas in the operating cost as it would be available essentially free from the landfill gas. However, if the LFG production is low for certain counties, natural gas can be purchased externally and converted into H_2 to keep the reactor running, or to scale up the production to reduce overall costs. When the cost of natural gas is factored in OPEX, the cost becomes \$1.5/kg of H_2 which is in line with the numbers reported in literature wherein hydrogen production cost from steam methane reforming ranges from \$1.25/kg for large systems to \$3.5/kg for small systems [234]. It is noted that these numbers have been evaluated for the SESMR process alone. An in-depth analysis where SESMR is coupled with a carbon capture system is detailed ahead.

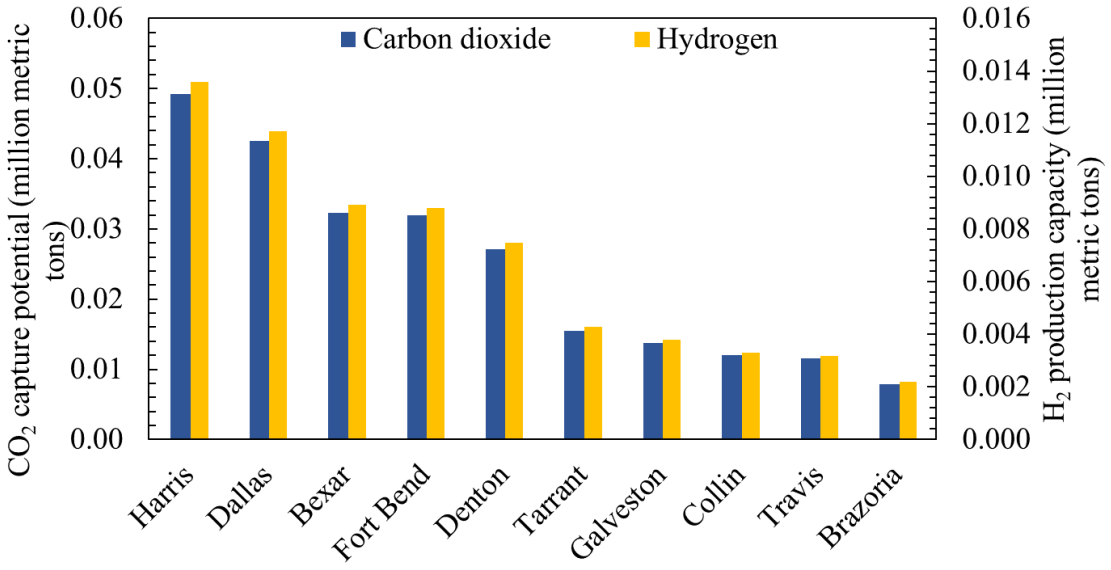

Figure 6.3. Total amount of CO_2 and H_2 that can be collected/produced annually (in million metric tons) for the top 10 counties in Texas.

Figure 6.4 quantifies the amount of water that would be required every day to capture all the CO_2 in the form of hydrates for two different test cases. Test case 1 corresponds to a gas uptake rate of 60mmol of CO_2/mol of water, as reported in the work of Mohammadi and Jodat [221]. Test case 2 corresponds to the theoretical maximum gas uptake capacity (174 mmol of CO_2/mol of water) that can be achieved for pure CO_2 hydrates. While a 100% capture efficiency is difficult to achieve in practice, the gas uptake rate can be enhanced by using various mechanical agitation methods and the use of nanoparticles or surfactants such as SDS to increase the gas-water contacts. The highest water requirement is for Harris county (0.92 million liters/day); this is about 0.05% of the water (1700 million liters/day) that is treated by the city of Houston every day [235].

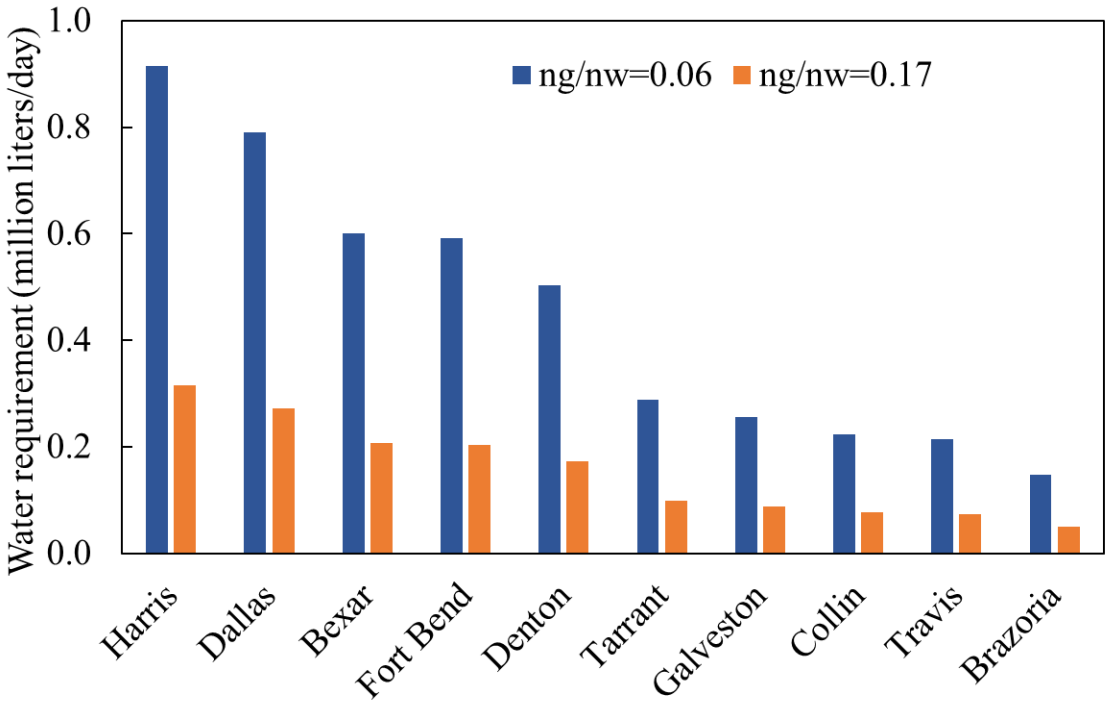

Figure 6.4. Amount of water required daily for capturing all the CO_2 collected as hydrates.

Figure 6.5 outlines the total electrical energy required daily to compress, refrigerate and maintain the gas at thermodynamic hydrate formation conditions (3.2 MPa @ 3 ^{o}C for CO_2 hydrates). The refrigeration process takes up most of the energy, accounting for about 64% of the electrical energy. The collective daily total electricity requirements for all the counties (145 MWh) corresponds to 0.01% of the total net electricity generated every day in Texas during the month of June [236].

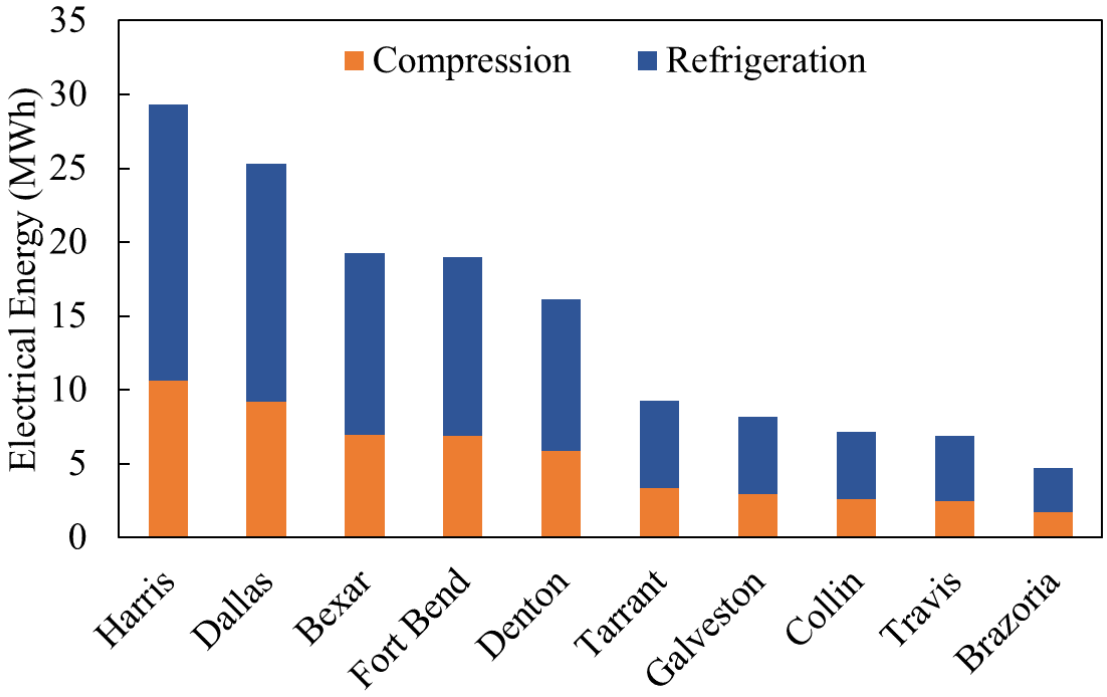

Figure 6.5. Electrical energy requirements for compression and refrigeration process.

Figure 6.6 outlines the capital cost requirements for compressors, pressure vessel reactors and refrigeration systems to set up CO_2 capture facilities across various counties in Texas. Compressors account for a majority of the capital costs (average contribution ~67%). Similar trends have been reported in past studies where compressor groups have accounted for about 83% of the total investment cost [223].

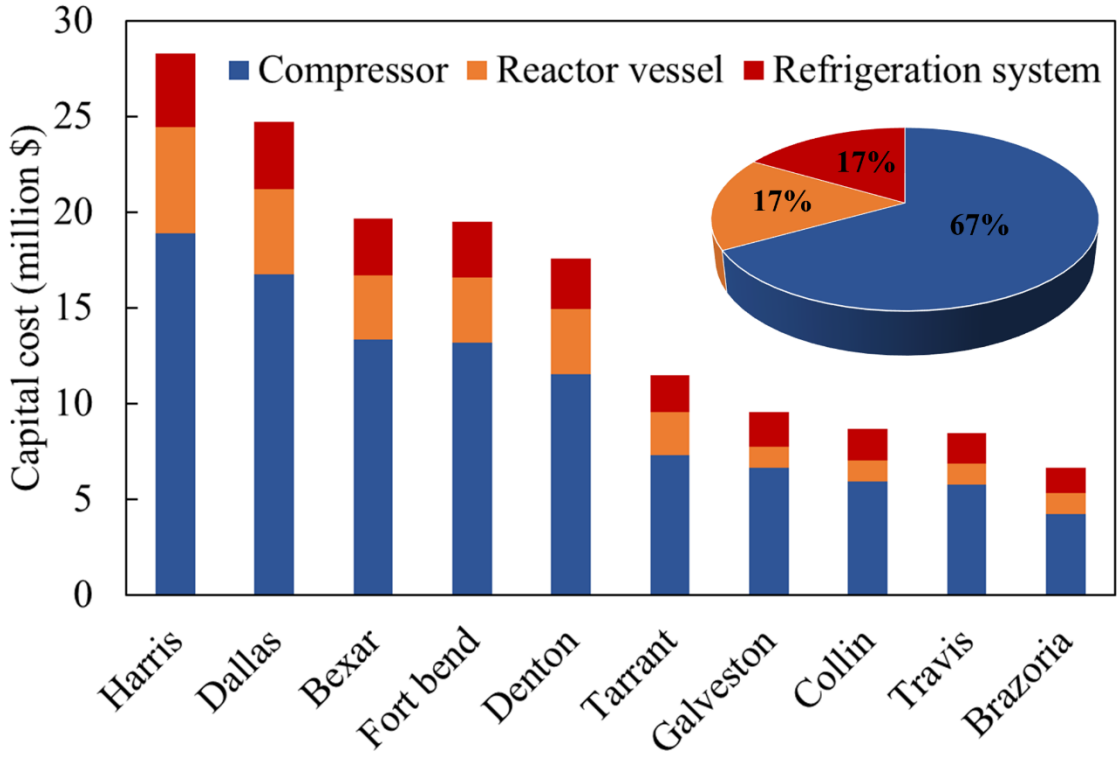

Figure 6.6. Capital cost for compressors, reactor vessels and refrigeration system.

Table 6.2 outlines the itemized cost estimations for the annual capital and operating cost to set up hydrate-based carbon capture centers across the top 10 counties in Texas. Annual capital costs are at least three times higher than the operating costs, and therefore one approach to lowering the carbon capture cost would be to bring down the capital costs (compressors which account for a majority of the CAPEX) while keeping the operating costs constant. The high capital cost due to compressors could potentially be decreased if the hydrate forming conditions could be brought down to lower pressures using thermodynamic promoters such as TBAB (Tetrabutylammonium bromide), TBAF (Tetrabutylammonium fluoride) and TBPB (Tetrabutylphosphonium bromide) [237]–[239]. Such tetraalkylammonium halide salts form hydrates under atmospheric conditions and are termed semiclathrate hydrates since their cage structures are composed of water

and the relatively large salt molecule (water-anion framework encapsulating the cation inside the cage that keeps the structure stable) and dodecahedral empty cages capable of storing small sized gas molecules like CO_2. This inherently translates to a very low gas uptake capacity than the pure sI hydrates, wherein gas molecules could potentially occupy all the cages. It is noted that while such tetraalkylammonium halide-based semiclathrate hydrates could bring down hydrate forming pressures, the increase in the amount of water required to capture the same amount of gas when compared to sI hydrates could potentially translate to higher capital cost for reactor vessels and operating costs for refrigeration and labor expenses.

Table 6.2 Itemized cost estimation for annual capital and operating cost (in million $) for 10 counties in Texas.

CAPEX (million $/year)					
County	**Compression**	**Refrigeration**	**Reactor vessel**	**Supplement**	**Total**
Harris	2.00	0.41	0.59	0.60	3.60
Dallas	1.77	0.37	0.47	0.52	3.14
Bexar	1.42	0.32	0.36	0.42	2.50
Fort Bend	1.40	0.31	0.36	0.41	2.48
Denton	1.23	0.28	0.36	0.37	2.24
Tarrant	0.77	0.20	0.24	0.24	1.46
Galveston	0.70	0.19	0.12	0.20	1.21
Collin	0.63	0.17	0.12	0.18	1.11
Travis	0.61	0.17	0.12	0.18	1.08
Brazoria	0.45	0.14	0.12	0.14	0.84
OPEX (million $/year)					
County	**Electricity**	**Maintenance**	**Other cost**	**Labor**	**Total**
Harris	0.69	0.05	0.03	0.35	1.12
Dallas	0.59	0.05	0.02	0.35	1.01
Bexar	0.45	0.04	0.02	0.35	0.86
Fort Bend	0.44	0.04	0.02	0.35	0.85
Denton	0.38	0.03	0.02	0.35	0.78
Tarrant	0.22	0.02	0.01	0.18	0.43
Galveston	0.19	0.02	0.01	0.18	0.39
Collin	0.17	0.02	0.01	0.18	0.37
Travis	0.16	0.02	0.01	0.18	0.36
Brazoria	0.11	0.01	0.01	0.18	0.31

Figure 6.7 quantifies the cost required to capture one metric ton of CO_2 across different counties in Texas. The lowest carbon capture cost corresponds to Harris county ($96/metric ton of CO_2). Brazoria county has the highest carbon capture cost at $145/metric ton of CO_2. This contrast in costs shows that scaling up of this technology could further bring down costs in the future. It is noted that this cost captures both the

capital and operating cost for a model hydrate-based carbon capture system, and CAPEX accounts for a significant portion (~75%) of the overall cost.

In order to investigate the effect of using TBAB on the economics of the carbon capture process, the entire analysis was repeated to account for the modified thermodynamic formation conditions and the water/energy requirements for the revised process in the presence of TBAB. The thermodynamic formation conditions in the presence of 10 wt% TBAB correspond to about 11 ^{o}C at 1 MPa, and therefore the CAPEX and OPEX were reanalyzed for the CO_2 capture system running at 6 ^{o}C (corresponding to 5 ^{o}C overcooling) at 1 MPa. It is noted that the system has been subjected to overcooling instead of over-pressurization to reduce the capital cost requirement for compressors. Pressurization, in this case, could be achieved by using two out of three stages for the compression system, as illustrated in Figure 6.2. In order to estimate the gas uptake capacity, it was assumed that 50% of the uptake capacity reported in the work of Mohammadi and Jodat [221] (40 mmol of gas/mol of water) could be achieved, as the experiments reported in this paper in the presence of 10 wt% TBAB were carried out at higher pressures and lower temperatures (3.2 MPa and 3 ^{o}C).

Figure 6.7 quantifies the capital and operating costs in the presence of TBAB, wherein the overall cost is actually observed to increase ($107-$137/metric ton of CO_2) when compared to the pure CO_2 hydrates case. This finding seems counterintuitive and can be explained by analyzing the changes in CAPEX and OPEX as detailed ahead:

- CAPEX: An increase in the amount of water required due to lower gas uptake capacity in the presence of TBAB leads to an increase in the number of reactors required to accommodate the hydrate precursor mixture, leading to an increased capital cost for reactors and refrigeration systems. However, this is counterbalanced by a significant reduction in the capital cost for compressors, and

therefore the overall capital cost required to capture one metric ton of CO_2 decreases.

- OPEX: The increased number of reactors leads to an increased labor and electricity cost corresponding to refrigeration while decreasing the electricity costs for the compression process. The net result is an increase in the operating cost since compression energy contributes to a tiny percentage (4-8%) of the overall operating cost.

The combined impact of the above-mentioned changes is a net increase in the overall cost for capturing one metric ton of CO_2. However, it is notable that the increase in overall cost is significant (~12%) only for the top 4 counties producing the highest amount of CO_2. The percentage increase falls to around 4% for all the remaining counties except Brazoria, where the overall cost decreases by 6% when TBAB is used. This implies using a thermodynamic promoter such as TBAB might be beneficial only for small-scale carbon capture systems.

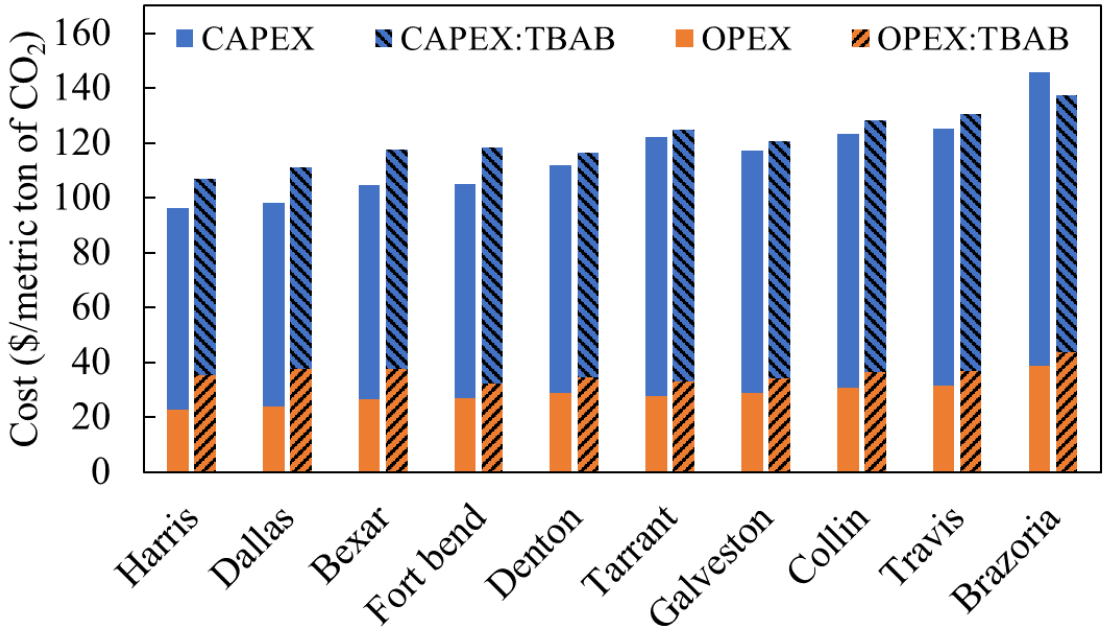

Figure 6.7. Cost (Capital + Operating) required to capture one metric ton of CO_2 across different counties in Texas.

Figures 6.8 (a) and (b) outline the NPV and PBP for a combined SESMR+CCS system set up at Harris and Brazoria county. A minimum cost of \$0.9/kg of H_2 would be required to have a positive 30-year NPV for Harris county, whereas the number increases to \$2.4/kg of H_2 for Brazoria county. This accounts for both the carbon capture cost and the cost for producing H_2 via SESMR. The payback period depends on the cost of producing hydrogen, with a 5-year payback period requiring hydrogen costs of \$1.35 /kg and \$4.95/kg for Harris and Brazoria county, respectively. It is evident that producing blue hydrogen from LFG look attractive from a business standpoint only for counties like Harris county that could potentially produce significant amounts of H_2 and CO_2 due to the economics of scale. To make this technology viable, the H_2 production capacity at counties like Brazoria county would need to be scaled up, with the additional capacity being used for SMR of natural gas.

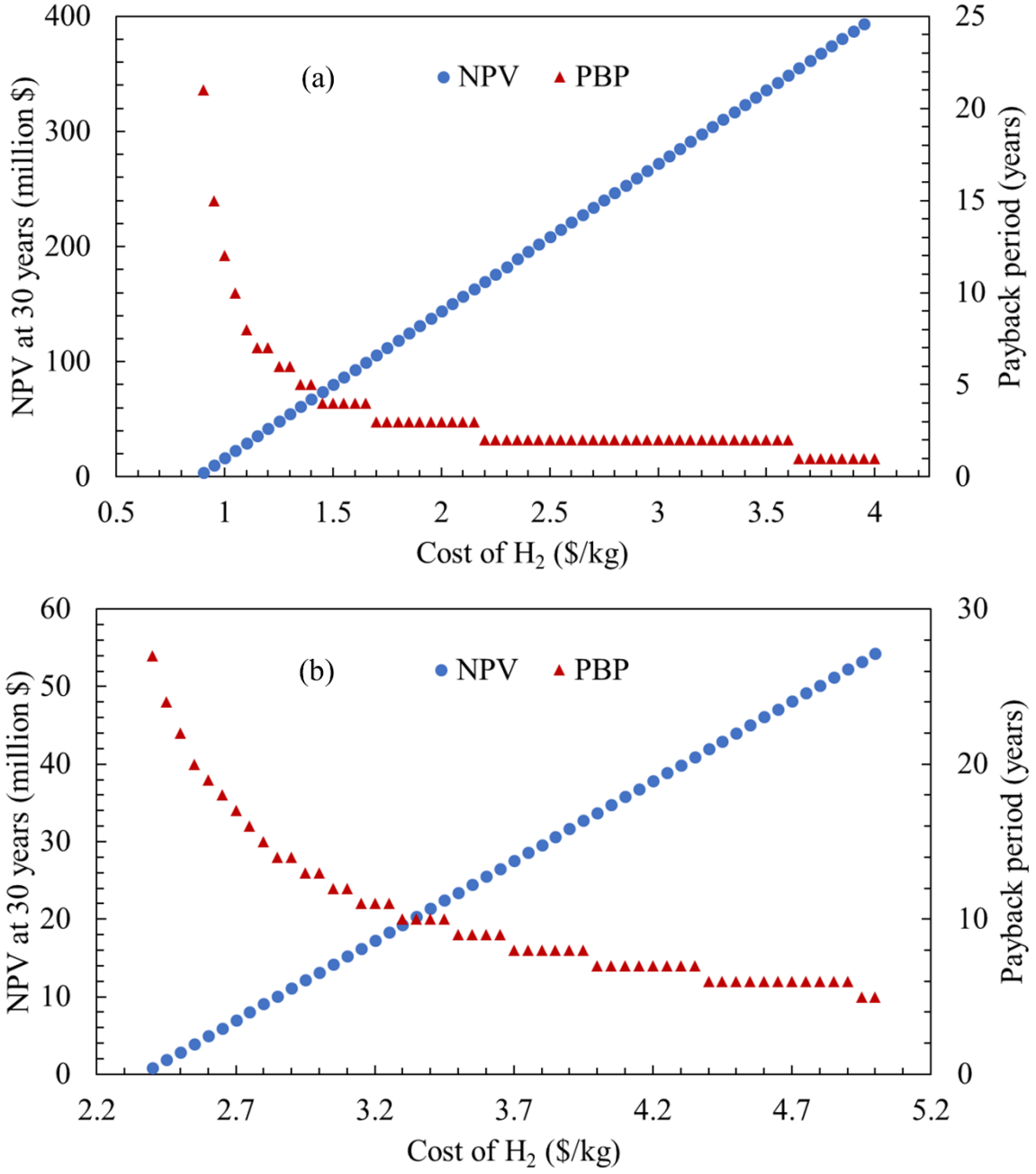

Figure 6.8 Net present value at 30 years and payback period for a combined SESMR + hydrates-based carbon capture system for producing hydrogen using steam reforming of LFG in (a) Harris county and (b) Brazoria county.

6.3 CONCLUSIONS

In summary, this chapter has analyzed the techno-economic factors involved in producing H_2 and capturing CO_2 produced by sorption enhanced steam methane reforming of landfill gas across different counties in Texas. The capital and operating costs for the SESMR process for Texas counties are scaled up from previously reported numbers obtained from ASPEN process simulation and itemized cost estimation analysis. The combined hydrogen production potential is about 0.07 million metric tons (enough to power 15,000 homes every year in US), and the cost of producing this H_2 from LFG stands at \$0.5/kg of H_2 for all the counties considered in the present analysis. This number increases to \$1.5/kg of H_2 if the natural gas for producing hydrogen is purchased externally.

This SESMR system has been used in combination with a hydrates-based carbon capture facility, and the energetics and costs involved in setting up such a facility have been evaluated at length. In doing so, the amount of water required, the energy required for compression and refrigeration, and the capital and operating cost required to set up and run such a facility has been investigated. The collective carbon capture potential for all the counties analyzed in the present chapter amounts to 0.24 million metric tons of CO_2 every year. The water requirements are not significant, with Harris county (which has the highest water requirement amongst all the counties in Texas) requiring only about 0.05% of the total water treated at Houston to convert all the CO_2 gas into hydrates. A total electrical energy of 145 MWh would be required every day to compress and refrigerate the water and gas to hydrate forming conditions which translate to about 0.01% of the total electricity production in Texas. The total carbon capture cost (CAPEX+OPEX) lies in the range of \$96-\$145/metric ton of CO_2 captured and is expected to decrease with subsequent scaling up of the process. Adding a thermodynamic

promoter such as TBAB results in a net increase in the overall cost to $107-$137/metric ton of CO_2 captured, except for Brazoria county. For Harris county, a minimum cost of $0.9/kg of H_2 would be required to produce a positive NPV over a 30-year period, whereas a 5-year payback period would require a minimum cost of $1.35/kg of H_2.

While the present analysis considers separate SESMR and hydrate-based carbon capture facilities for every county in Texas, an alternative approach could be to build a centralized facility to collectively convert all the CH_4 to H_2 while capturing CO_2 in the form of hydrates. Such a facility could utilize the existing natural gas pipelines in Texas to transport CH_4 to the centralized facility and could further bring down the cost of capturing CO_2 and producing H_2 due to economics of scale.

Chapter 7: Conclusions and suggestions for future work

This chapter summarizes the key findings and contributions emerging from this dissertation and outlines future research directions in the field of hydrate formation.

7.1 MAJOR SCIENTIFIC FINDINGS AND CONTRIBUTIONS OF THIS DISSERTATION

This dissertation has resulted in seminal scientific contributions in the fields of hydrates and interfacial sciences. Notably, the thermodynamic, as well as the kinetic aspects of hydrate formation have been addressed at length. Multiple ultralow power consuming and passive techniques for rapid nucleation of hydrates have been discovered. These techniques can enable multiple applications which require rapid production of hydrates. Furthermore, novel techniques for obtaining high throughput measurements of thermodynamic hydrate formation conditions in the presence of various additives have been proposed. The utility of physics-aware machine learning algorithms for predicting hydrate formation conditions is demonstrated. Finally, a techno-economic analysis sheds light on the various factors associated with a hydrates-centered carbon capture and storage system, when used in conjunction with a steam methane reforming system for producing H_2 (and capturing CO_2 as hydrates). Major scientific advancements emerging from this work are summarized ahead.

7.1.1 Role of electric field and aluminum foams in accelerating nucleation of THF hydrates

It was demonstrated aluminum foam-based electronucleation electrodes lead to ultrafast nucleation of THF hydrates. Major scientific findings include:

- When used as electronucleation electrodes, open-cell metal foam leads to a 150x reduction in induction time compared to non-foam electrodes.

- Induction time is voltage-dependent, with higher voltages leading to shorter nucleation times.
- Al-foam-based electronucleation is polarity dependent with the induction times reducing by 40x (at 5V) when polarity is switched from cathode to anode.
- Almost instantaneous nucleation is obtained with the use of Al foam as anode with average induction times spanning 20s for low voltages (20 V).
- Use of foams can decrease the inherent stochasticity of the nucleation process, reflected by a decrease in standard deviation value from 60% for the non-foam experiments to about 13-25% of the mean value for foam measurements.
- Hydrate formation time is reduced by foams that aid in rapid removal of the heat released during hydrate formation (by enhancing the effective thermal conductivity of the hydrate precursor solution).
- Different fundamental mechanisms are responsible for nucleation promotion. Bubbles act as nucleation sites when the foam is used as cathode. The promoting effect for the case of foam as anode is the formation of octahedral polynuclear coordination compound complexes that enhance hydrate nucleation to a greater extent than bubble-based mechanistic effects.

7.1.2 Role of aluminum in accelerating nucleation of CO_2 hydrates

This study reported the discovery of a simple, passive nucleation promotion technique wherein an aluminum surface was observed to significantly promote the nucleation of CO_2 hydrates. Major scientific conclusions from this study include:

- Al promotes the nucleation of CO_2 hydrates; no nucleation was observed on other surfaces such as copper, stainless steel or anodized aluminum.

- Mean induction times and the nucleation rates decrease and increase, respectively, with increasing droplet volumes. Droplet nucleation times on Al surface range from 8 mins to 22 hours.
- The nucleation-promoting effect of Al surfaces cannot be replicated by droplets containing salts of Al such as $Al_2(SO_4)_3$, $AlCl_3$ on an inert stainless-steel surface, indicating that surface chemistry plays a significant role.
- Al-based promotion is seen with saltwater as well, albeit with a 53% increase in mean induction time and a 34% reduction in the nucleation rate.
- Increasing the CO_2 dissolution time leads to much more vigorous hydrate growth, attributable to higher initial CO_2 concentrations inside the droplet, which enhance diffusion post-nucleation.
- Nucleation was observed to initiate at the two-phase (water-Al) area instead of the three-phase (CO_2-water-Al) contact line, highlighting the role of metal-water contacts for catalyzing nucleation.
- Al-enhanced nucleation can be attributed to Al-water reactions leading to the generation of H_2 bubbles, which likely act as nucleation sites.

7.1.3 Investigating inhibition effect of amino acids on CO_2 hydrate formation

The kinetic and thermodynamic inhibition effect of five amino acids have been investigated in this study using a newly developed high throughput measurement technique. Major scientific conclusions from this study include:

- Amino acids inhibit the nucleation kinetics of CO_2 hydrate formation. The inhibition effect directly correlates with the hydropathy index defining the hydrophobic behavior of the side chain.

- The highest and lowest kinetic inhibition was observed for Tryptophan and Isoleucine/Leucine, with nucleation rates corresponding to 0.032 min^{-1} and 0.048 min^{-1}, respectively.
- Al metal does not influence the thermodynamics of hydrate formation.
- Most amino acids (Leucine, Tryptophan and Phenylalanine) have a negligible thermodynamic inhibition effect owing to their low solubilities in water.
- Thermodynamic inhibition effect is maximum for isoleucine and methionine with average depression in freezing point temperatures corresponding to 0.2 and 0.12 K respectively at 0.1 and 0.2 mol% concentration.

7.1.4 Investigating the predictive utility of machine learning algorithms when combined with thermodynamic features to predict phase equilibrium conditions for hydrate formation

Machine learning models (using thermodynamically consistent variables as input features in the algorithm) have been trained, and their performance has been evaluated on an extensive experimental database consisting of more than 1800 data points collected from literature. Major scientific conclusions from this study include:

- Thermodynamic features such as partial pressure of individual gases, specific gravity of hydrate precursor mixtures and activity contribution due to salts have been used as input features in the ML algorithms.
- Using such physics-based features in ML frameworks enabled the models to track individual contributions of gases towards hydrate formation and couple the inhibition effect with the mechanisms underlying salt-water interactions.
- Extreme Gradient Boosting (XGBoost) algorithm has been used for the first time for prediction of thermodynamic phase equilibria for hydrates.

- XGBoost exhibits the highest prediction performance with R^2 accuracies of 99.85% (training data), 98.06% (test data) and 99.56% (overall data).
- Prediction accuracy of the ML models is lower in regions of low temperature and high pressure, which contain sparse experimental data points.
- ML algorithms trained with fundamental thermodynamic features as input variables can capture the inhibition effect of salts containing monovalent and divalent cations.

7.1.5 Studying the techno-economics associated with industrial sized hydrates-based carbon capture facility

The energetics and the economics of a facility intended to produce H_2 and capture CO_2 (as hydrates) produced by steam reforming of methane in landfill gas (LFG) across various counties in Texas have been evaluated. Major scientific conclusions from this study include:

- Collective hydrogen production and carbon capture opportunity for the top 10 landfill sites in Texas generating H_2 and CO_2 via SMR of LFG is 240,000 and 70,000 metric tons every year, respectively.
- Unit cost of producing hydrogen via SMR is \$0.5/kg of H_2 and \$1.5/kg of H_2 if the cost of natural gas is factored in OPEX for all the counties.
- Total electrical energy of 145 MWh would be required every day collectively for all these counties to meet the compression and refrigeration requirements for the carbon capture system.
- Compressors account for the highest percentage of capital costs corresponding to about 67% of total CAPEX.

- Total cost (capital + operating) lies in the range of \$96-\$145/metric ton of CO_2 captured, and is expected to decrease as production capacity scales up.
- Adding TBAB to the hydrate precursor mixture increases the total carbon capture cost to \$107-\$137/metric ton of CO_2.
- A minimum cost of \$0.9/kg and \$2.4/kg of H_2 would be required for Harris and Brazoria county, respectively, for a 30-year net positive value (NPV).
- A 5-year payback period (PBP) would require a minimum cost of \$1.35 and \$4.95/kg of H_2 for Harris and Brazoria county, respectively.

7.2 RECOMMENDATIONS FOR FUTURE WORK

The advancements reported in this dissertation have laid the groundwork for future studies related to kinetics and thermodynamic of hydrate formation, some of which are detailed ahead.

7.2.1 Role of electric field and acoustics for nucleation of cyclopentane hydrates

Cyclopentane (C_5H_{10}) forms a hydrate ($C_5H_{12}O$) with water (molar ratio of cyclopentane: water is 1:17) below 7.7°C at atmospheric pressure. However, cyclopentane and water do not mix, which necessitates the use of emulsions or mechanical agitation to promote nucleation.

Figure 7.1 shows the schematic of a custom-built cell made out of PMMA that can be used to study electro-nucleation of cyclopentane (CyP) hydrates. Hydrate formation can be investigated at the water-cyclopentane interface using visualization or via a thermocouple to detect the temperature spike related to hydrate formation. An electric field applied across the cyclopentane-water layer would accumulate charges at the cyclopentane-water interface. It is noted that cyclopentane is electrically insulating,

and therefore the electric field will exist only inside cyclopentane. No electric field exists in water since it is an electrical conductor. This experiment could potentially uncover the influence of an electric field/surface charge on electro-nucleation of CyP hydrates. The challenge with fabricating such a setup would be to hermetically seal the cells containing the cyclopentane-water mixture (since cyclopentane is a volatile fluid) while ensuring that electrodes and thermocouples can be placed in the setup to allow electric fields to be set up across the film interface. The thermocouple would have to be ungrounded to prevent the electric field from influencing the temperature measurements. The cell could be cooled either by placing it inside a chamber (flushed with N_2 gas to avoid condensation on the surfaces) on a cold plate, or inside a humidity controlled environmental chamber.

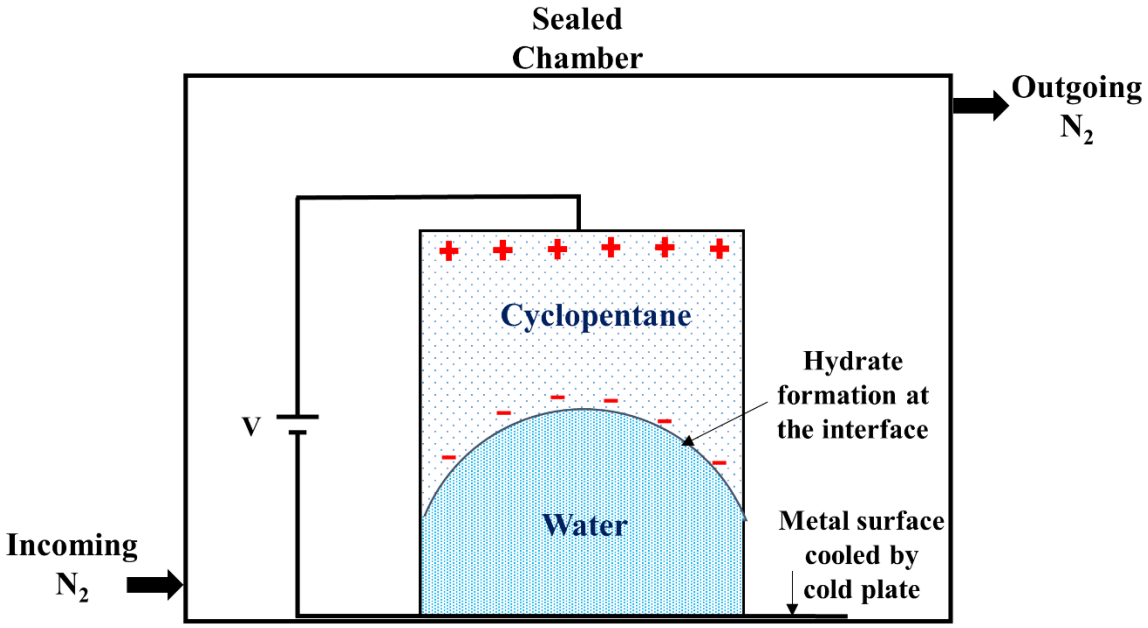

Figure 7.1 Schematic of cell to study electronucleation at a cyclopentane-water interface.

The experimental procedure would involve depositing a thin water film (1.5 ml) and filling the cell with cyclopentane followed by cooling below the hydrate forming

conditions (<7.7 ^{o}C) at atmospheric pressure, following which the electronucleation voltage could be applied. Induction time could be measured using visualization or by inserting a thermocouple in the cell to measure temperature spikes related to the latent heat of hydrate formation. Various types of electric pulses such as DC or an AC field, or other waveforms (sinusoidal, square, triangle) could be applied. This study can uncover the role of electric fields and surface charges on the nucleation kinetics of cyclopentane hydrates.

If the cell containing the cyclopentane-water solution is cooled inside an environmental chamber, the bottom surface could be placed on an acoustic transducer to introduce ultrasonic waves in the solution. This would result in the perturbation and subsequent generation of interfacial waves, increasing the cyclopentane-water interfacial area and possibly enhancing the diffusion of cyclopentane in the water medium, all of which could be conducive to hydrate formation. Such a study could investigate the influence of frequency and amplitude of acoustic disturbances on the nucleation kinetics of cyclopentane hydrate.

7.2.2 Bubble-based promotion of CO_2 hydrate formation

A common factor underlying most of the promoting mechanisms discussed in this dissertation are bubbles, that act as nucleating sites to stimulate nucleation. Bubble-induced hydrate formation via the use of bubble column reactors or gas-inducing impellers has been studied in the past for enhancing the formation of CO_2 and CH_4 hydrates [240]–[243]. Preliminary experiments conducted with CO_2 hydrates, as illustrated in Figure 7.2, did yield promising results, wherein complete conversion of 10 ml water to hydrate was observed within 5-7 minutes. While these were preliminary proof of concept experiments, the gas uptake rate could be quantified as a function of the

inlet gas flow rate and the size of the incoming CO_2 bubbles, which could be controlled with the aid of a sparger tube.

Figure 7.2 Rapid hydrate formation observed in bulk water (left) and test tube (right), induced by bubbling CO_2 through water.

Importantly the influence of precooling CO_2 gas before it enters the system in the form of bubbles can be studied. It is possible that precooling the gas could enable the water-reactor system to be maintained at a higher temperature, that could have energy-saving benefits.

7.2.3 Machine learning + QSPR

This dissertation explored using fundamental thermodynamic features as input variables in the machine learning algorithms to directly couple the phase equilibrium

conditions with the fundamental features directly affecting the physics of the problem. A follow-up study would explore the effect of different molecular features for an inhibitor and quantify its influence on thermodynamic hydrate inhibition. One way to do this would be to resort to a quantitative structure-property relationships (QSPR) strategy, which utilizes the fact that any experimentally measurable property of a surfactant or chemical can be expressed as a function of the molecular structure of the surfactant/chemical. Such QSPR models use different kinds of molecular descriptors to encode numerical characteristics associated with the chemical structure of the molecule [244]–[247]. Several software packages aid in the computation of molecular descriptors for various chemical structures [248]. These can be used as input features to train ML algorithms or regression-based models to predict the hydrate dissociation temperature as a function of these input features, which can then be coupled with variable importance measuring tools such as SHAP. Such an analysis could provide insights into the structural features that contribute significantly towards suppression or promotion of hydrate dissociation temperature, and could be used to tailor the structural properties of hitherto unexplored chemicals to tune thermodynamic hydrate forming conditions.

It is important to note that the performance of ML models is determined by the experimental dataset employed for training the algorithms. Non-uniformities or gaps in the distribution of experimental data over a specific range of values or thermodynamically inconsistent data affect the quality of predictions, as is the case for extreme temperature and pressure in the case of hydrates. In this dissertation, an exhaustive data bank (>1800 data points) was used so that an error or discrepancy in reported experimental data would not significantly bias the model. Future efforts should involve the application of consistent screening criteria to assess the thermodynamic consistency of the experimental data employed [249], [250] to train such algorithms.

7.2.4 Aluminum or active metal-based promotion of CH_4, H_2, and tetraalkylammonium salt hydrates

This dissertation reported the catalyzing effect of Al metal in enhancing nucleation kinetics of CO_2 hydrates. Following the dissolution of CO_2 in water, it is expected that the presence of carbonic acid would break down any native oxide layers on the surface of Al, thereby promoting Al-water contact. This suggests that Al might not be as good a nucleating agent for other hydrates, which might not form acidic solutions in water which would help minimize the oxide layers. This hypothesis could be tested by repeating the experimental procedure as detailed in this dissertation for other gases such as CH_4 and H_2, and for tetraalkylammonium salt-based hydrates that form at atmospheric pressures. Furthermore, the role of other active metals which behave similarly to Al in an aqueous medium should be explored. One such metal is magnesium which behaves similar to aluminum and has been observed to cause a significant reduction in induction time in a recent follow-up study by the present group [251].

7.2.5 Droplet-based measurement of thermodynamic phase equilibria of hydrates in the presence of an electric field

The advantage of using aluminum as nucleation promoting medium in a vessel with optical windows is that it enables measurement of thermodynamic phase equilibria of any promoting/suppressing chemical on CO_2 hydrate formation. A recent study reported a 5.8 times reduction in induction time of CO_2 hydrates with the application of an electric field of 10^4 V/m [252]. Using the setup for thermodynamic phase equilibria extraction as discussed in this dissertation, experimental studies on the shift in p-T curve in the presence of electric fields could shed further light on the thermodynamic promotion/inhibition effect of electric field on CO_2 hydrates.

Appendices

APPENDIX A: SUPPORTING INFORMATION FOR AL-BASED PROMOTION OF CO_2 HYDRATES

Appendix A provides data confirming the stochasticity of the droplet nucleation experiments for CO_2 hydrates that provide every droplet acted as an individual microsystem for hydrate formation and images comparing the morphology of droplets with different CO_2 dissolution times (90 mins vs 24 hours).

A.1 Confirmation of the stochastic nature of nucleation in our experiments

The below figure shows the nucleation order of the droplets on three plates for two experiments (with 40 μL and 20 μL droplets). It is seen that the droplets nucleate randomly, and that a nucleating droplet does not influence its surrounding droplets.

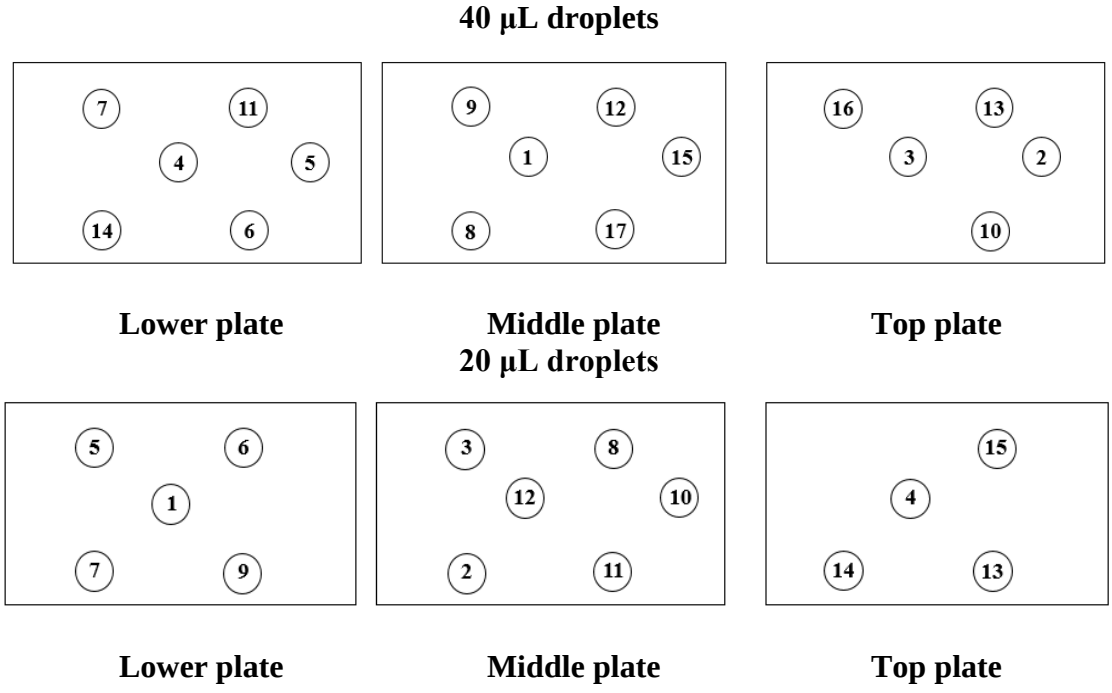

Figure A.1. Nucleation order of the droplets for experiments employing 40 (top) and 20 (bottom) μL droplets

The tables below shows the induction time for 20 and 40 μL droplets in the order in which they nucleated. The droplets show stochastic nucleation (as expected).

Table A.1 Induction time data for 40 μL droplets obtained in a single run

Droplet #	Induction time (mins.)
1	8.05
2	11.92
3	56.73
4	66.32
5	77.02
6	77.87
7	81.75
8	97
9	184.15
10	199.99
11	205.22
12	300.62
13	302.52
14	316.15
15	352.49
16	376.37
17	506.01

Table A.2 Induction time data for 20 μL droplets obtained in a single run

Droplet #	Induction time (mins.)
1	21
2	79
3	83.32
4	99.37
5	205
6	332
7	464.3
8	498.87
9	523
10	524.7
11	565
12	627
13	943.4
14	1062
15	1073

A.2 Histograms showing fraction of droplets nucleating in different time intervals

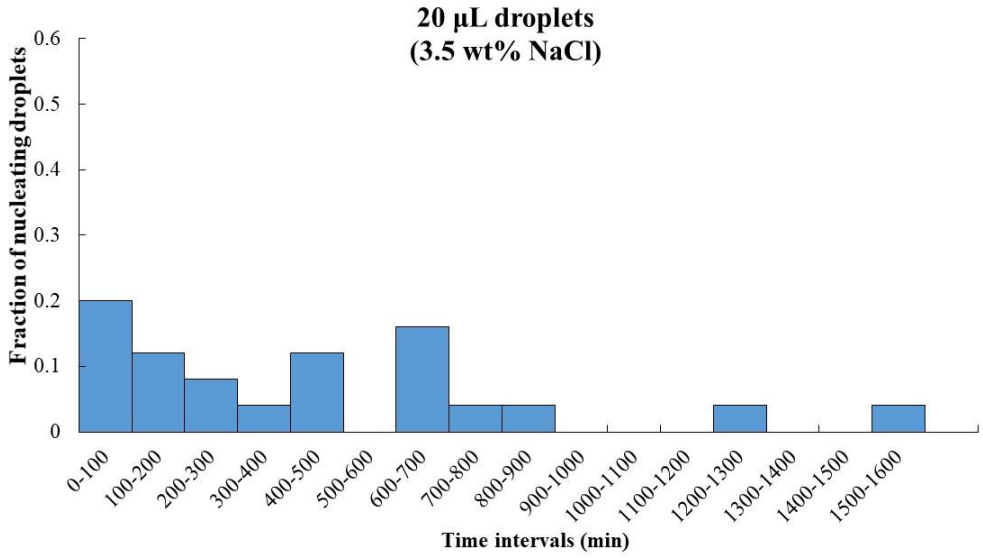

Figure A.2 Fraction of 20 µL droplets nucleating in different time intervals (droplets contain 3.5 wt% NaCl).

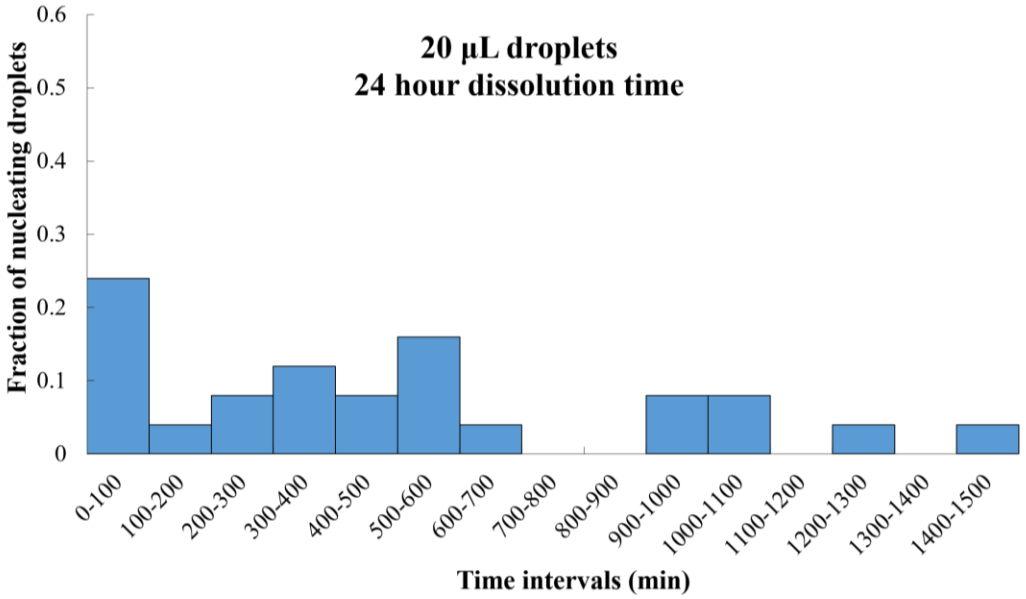

Figure A.3 Fraction of 20 µL droplets nucleating in different time intervals (24-hour CO_2 dissolution time).

A.3 Comparison of droplet morphologies for different dissolution times of CO_2

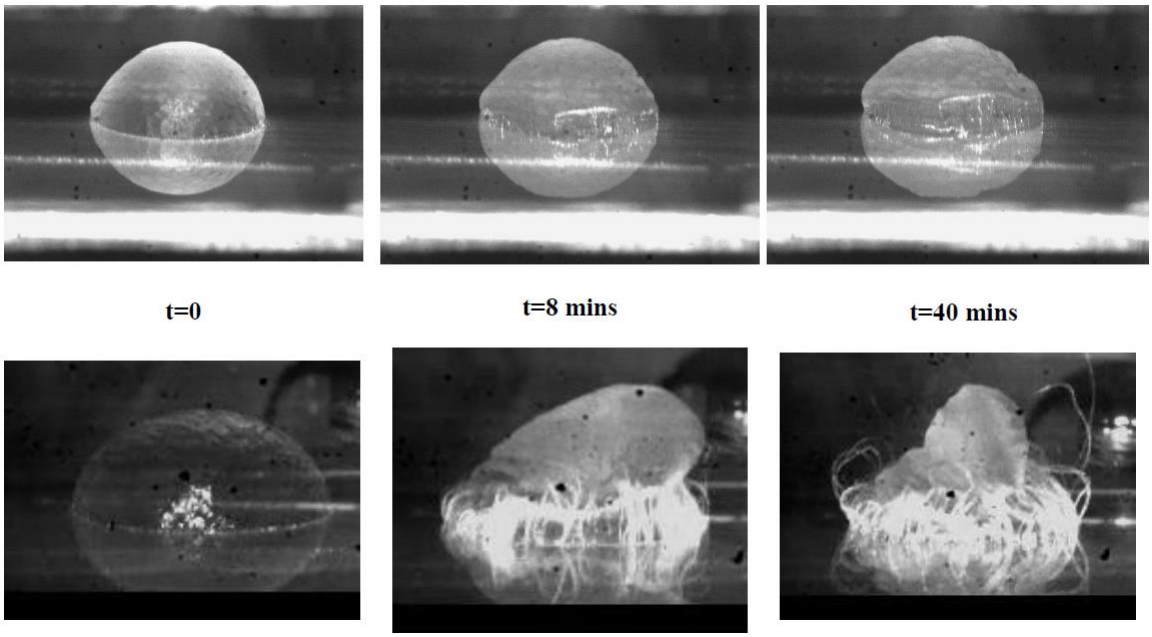

Figure A.4 Droplet morphologies for a CO_2 dissolution time of 90 minutes (top) and 24 hours (bottom) for a droplet volume of 20 μL.

Droplets (20 μL) in the top and bottom rows are exposed to high-pressure CO_2 for 90 minutes and 24 hours respectively. Higher concentrations of dissolved CO_2 in the droplet in the bottom row lead to more vigorous growth characterized by whisker formation.

A.4 Snapshots showing color change in droplets imbued with a colorimetric indicator

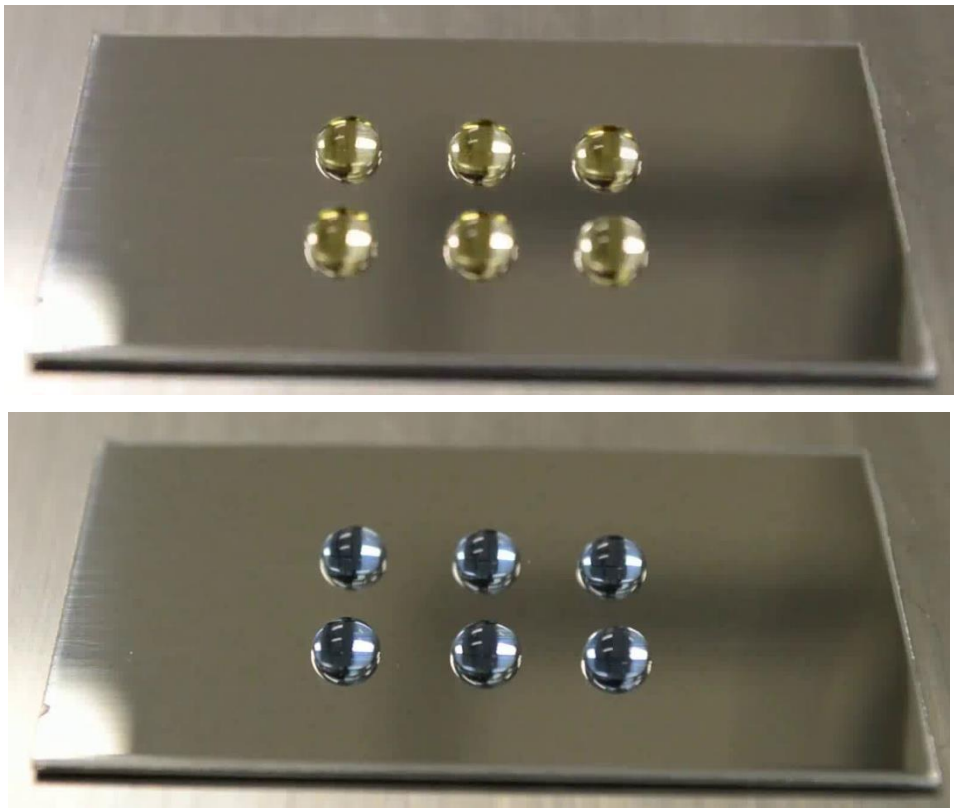

Figure A.5 DI water droplets imbued with pyrocatechol violet indicator placed on the Al substrate (top) turned blue (bottom) indicating the presence of Aluminum ions

APPENDIX B: FUNDAMENTAL INTERFACIAL MECHANISMS UNDERLYING ELECTROFREEZING[5]

A review article detailing studies on promoting ice nucleation via the use of electric fields was published in Elsevier Journal of Advances in Colloid and Interface Science as a part of the Ph.D. research, the abstract for which has been provided below:

Abstract: This article reviews the fundamental interfacial mechanisms underlying electrofreezing (promotion of ice nucleation via the application of an electric field). Electrofreezing has been an active research topic for many decades, with applications in food preservation, cryopreservation, cryogenics and hydrate formation. There is substantial literature detailing experimental and simulations-based studies, which aim to understand the complex mechanisms underlying accelerated ice nucleation in the presence of electric fields and electrical charge. This work provides a critical review of all such studies. It is noted that application-focused studies of electrofreezing are excluded from this review; such studies have been previously reviewed in literature. This review focuses only on fundamental studies, which analyze the physical mechanisms underlying electrofreezing. Topics reviewed include experimental studies on electrofreezing (DC and AC electric fields), pyroelectricity-based control of freezing, molecular dynamics simulations of electrofreezing, and thermodynamics-based explanations of electrofreezing. Overall, it is seen that while electrofreezing can enable disruptive advancements in the control of liquid-to-solid phase change, our current understanding of the underlying mechanisms can be significantly improved through further studies of various interfacial effects coming into play.

[5] The contents of this Appendix have been published in the following journal review article: Acharya, P.V. and Bahadur, V., 2018. Fundamental interfacial mechanisms underlying electrofreezing. Advances in colloid and interface science, 251, pp.26-43.

APPENDIX C: MAGNESIUM-PROMOTED RAPID NUCLEATION OF CARBON DIOXIDE HYDRATES[6]

A follow up study was conducted in Bahadur lab based on the work on Al-promoted nucleation of CO_2 hydrates to explore other active metals that could have similar nucleation-promotion benefits. This resulted in a publication and a patent application and the abstract for the article published in ACS Sustainable Chemistry & Engineering is provided below:

Abstract: Gas hydrates offer solutions in areas like CO_2 sequestration and desalination. However, their formation is severely limited by long induction (wait) times for nucleation, which range from hours to days. Many existing nucleation promotion techniques involve chemical additives, which invite environmental and process-related concerns. Here, we report a simple, passive, and environmentally friendly technique to significantly promote the nucleation of CO_2 hydrates: magnesium (in pure and alloy forms) triggers nucleation almost instantaneously. We report induction times of less than 1 min, which is the fastest induction time reported for any gas hydrate under stagnant conditions. This translates to Mg-promoted nucleation rates being 3000 times higher than the baseline. Statistically meaningful measurements of nucleation kinetics (in milliliter and liter-scale reactors), direct visualization of nucleation, and X-ray photoelectron spectroscopy (XPS)/Fourier-transform infrared spectroscopy (FTIR) analysis uncover several chemistry-related insights associated with Mg-based promotion. Importantly, the three-phase line of magnesium–water–CO_2 gas is key to promotion. Porous oxide layers, generation of H_2 nanobubbles, and chemisorption of CO_2 on Mg surfaces are other factors responsible for accelerated nucleation. Interestingly, Mg alloys exhibit faster

[6] The contents of this appendix have been published in the following journal article: Kar, A., Acharya, P.V., Bhati, A., Mhadeshwar, A., Venkataraman, P., Barckholtz, T.A., Celio, H., Mangolini, F. and Bahadur, V., 2021. Magnesium-Promoted Rapid Nucleation of Carbon Dioxide Hydrates. *ACS Sustainable Chemistry & Engineering*, *9*(33), pp.11137-11146.

nucleation promotion than pure Mg, which is significant in salt water medium. Overall, our work opens up pathways for faster synthesis of hydrates, which is critical to realizing applications.

APPENDIX D: MACHINE LEARNING-BASED PREDICTIONS OF BENEFITS OF HIGH THERMAL CONDUCTIVITY ENCAPSULATION MATERIALS FOR POWER ELECTRONICS PACKAGING [7]

Abstract: Machine learning (ML)-based predictive techniques are used in conjunction with a game-theoretic approach to predict the thermal behavior of a power electronics package and study the relative influence of encapsulation material properties and thermal management techniques in influencing hotspot temperatures. Parametric steady-state and transient thermal simulations are conducted for a commercially available 1.2 kV/444 A Silicon Carbide (SiC) half-bridge module. An extensive databank of 2592 (steady-state) and 1200 (transient) data points generated via numerical simulations is used to train and evaluate the performance of three ML algorithms (random forest, support vector regression and neural network) in modeling the thermal behavior. The parameter space includes the thermal conductivities of the encapsulant, baseplate, heat sink and cooling conditions deployed at the sink and covers a variety of materials and cooling scenarios. Excellent prediction accuracies with R^2 values > 99.5% are obtained for the algorithms. SHAP (Shapley Additive exPlanations) dependence plots are used to quantify the relative impact of device and heat sink parameters on junction temperatures. We observe that while heatsink cooling conditions significantly influence the steady-state junction temperature, their contribution in determining the junction temperature in dynamic mode is diminished. Using ML-SHAP models, we quantify the impact of emerging polymeric nanocomposites (with high conductivities and diffusivities) on hotspot temperature reduction, with the device operating in static and dynamic modes.

[7] The contents of this Appendix have been published in the following journal article: Acharya, P.V., Lokanathan M, Bahadur, V., Hebner, R., Ouroua, A. and Strank, S.2021. Machine learning-based predictions of benefits of high thermal conductivity encapsulation materials for power electronics packaging. *Journal of Electronic Packaging*, 143(4), p.041109.

Overall, this study highlights the attractiveness of ML-based approaches for thermal design, and provides a framework for setting targets for future encapsulation materials.

APPENDIX E: GREEN HYDROGEN-BASED ENERGY STORAGE IN TEXAS FOR DECARBONIZATION OF THE ELECTRIC GRID [8]

Steam methane reforming of natural gas is one of the most widely used techniques for generating hydrogen. However, other techniques such as electrolysis to split up water have also been used to generate hydrogen. This study explores the usage of green hydrogen generated by converting the excess renewable energy generated in the state of Texas and using it as a long-duration energy storage medium.

Abstract: Increasing the penetration of renewables-based power generation such as from wind and solar is key to curbing greenhouse emissions resulting from the use of fossil fuels. As the capacity of solar and wind installations increase, the highly dynamic nature of renewable generation leads to frequent energy curtailment in instances when the total generation exceeds the load. In the present work, data from ERCOT (which manages the primary electric grid in Texas) is analyzed, to study potential storage of excess wind and solar energy via electrolysis-driven conversion to hydrogen (green hydrogen). This stored hydrogen could be converted back to electricity and fed into the grid whenever there is an energy deficit. In this study, a long-duration storage system (based on estimated capacity increases by 2025) is characterized in terms of storage size, rated power and the costs involved in generating H_2 via electrolysis. This analysis reveals the need for long-duration storage in two periods: i) mid-March to June, and ii) mid-October to December. During these periods, the surplus energy generated and stored in the form of green hydrogen would be self-sufficient to provide the deficit energy for instances when generation from renewables cannot meet load requirements. Minimum

[8] The contents of this Appendix have been published in the following conference article: Wikramanayake, E., Acharya, P.V., Kapner, M. and Bahadur, V., 2021, April. Green hydrogen-based energy storage in Texas for decarbonization of the electric grid. In 2021 IEEE Green Technologies Conference (GreenTech) (pp. 409-415). IEEE.

storage capacities of 10,000 & 3500 GWh would be required for these periods to avoid curtailment. Preliminary techno-economic analysis suggests that total electrolyzer capacity of ~ 40 GW would be required to avoid significant curtailment. Any added capital cost beyond this rating would not yield significant returns on investment as hydrogen production would have reached its peak capacity. Furthermore, the cost for producing hydrogen via electrolysis ($2-4) for electrolyzers at such capacity would be competitive with existing steam reforming technologies. Overall, the proposed long-duration storage system can increase the contribution of renewables to the Texas grid by 16%. The analysis and insights obtained from this study can serve as a benchmark and seed future studies in planning and designing long-duration storage systems based on the estimated capacity increase in renewables.

APPENDIX F: MODELING THE INFLUENCE OF MARANGONI FLOWS ON THE LEIDENFROST STATE ON SOLID AND LIQUID SUBSTRATES[9]

Abstract: Boiling heat transfer affects various processes related to energy, water and manufacturing. In the film boiling regime, heat transfer is substantially lower than in the nucleate boiling regime, due to the formation of a vapor layer at the solid-liquid interface (Leidenfrost effect). In this work, analytical modeling of the Leidenfrost state of droplets on solid and liquid substrates has been carried out. A key aspect of this study is the focus on surface tension gradients on the surface of a liquid (Leidenfrost droplet or liquid substrate), which actuate thermo-capillary driven Marangoni flows. The presence of Marangoni flows has non-trivial implications on the resulting thickness of the Leidenfrost vapor layer. This analysis shows that the pumping effect generated in the vapor layer due to Marangoni flows can significantly reduce the Leidenfrost vapor layer thickness.

[9] The contents of this Appendix have been published in the following conference article: Shahriari, A., Acharya, P.V. and Bahadur, V., 2018, June. Modeling the influence of Marangoni flows on the Leidenfrost state on solid and liquid substrates. In International Conference on Nanochannels, Microchannels, and Minichannels (Vol. 51197, p. V001T06A006). American Society of Mechanical Engineers.

APPENDIX G: REVIEW OF NANOCOMPOSITE DIELECTRIC MATERIALS WITH HIGH THERMAL CONDUCTIVITY[10]

Abstract: Dielectric materials with high thermal conductivity can enable disruptive performance enhancement in the areas of electronics packaging, thermal management, energy storage, cabling, and heat sinks. There have been widespread global efforts over the past decade on developing novel nanocomposite dielectric materials. As a baseline, legacy polymers and epoxies used in the above-mentioned applications have very low thermal conductivities ranging from 0.1-0.5 $W \cdot m^{-1} \cdot K^{-1}$. Recent advances have led to commercial availability of polymeric materials with thermal conductivities approaching ~ 10 $W \cdot m^{-1} \cdot K^{-1}$. Importantly, several fundamental studies report novel nanocomposites with thermal conductivities > 50 $W \cdot m^{-1} \cdot K^{-1}$. This article summarizes progress in the development of such materials with a focus on developments that show promise for improved practical dielectrics. This review highlights that high thermal conductivity alone is inadequate to characterize of the suitability of any material for the above applications. Other thermal properties like thermal diffusivity, glass transition temperature and the ratio of the in-plane to out of plane thermal conductivity are important to quantify the thermal performance of novel nanocomposites. Additionally, characterization and understanding of mechanical properties (coefficient of thermal expansion, elastic modulus) and electrical properties (dielectric strength, dielectric permittivity) are critical for holistic multifunctional assessments of these materials. There are other parameters and properties which influence performance, life and manufacturability like viscosity, moisture absorption etc.

[10] The content of this appendix has been published in the following journal review article: Lokanathan, M., Acharya, P.V., Ouroua, A., Strank, S.M., Hebner, R.E. and Bahadur, V., 2021. Review of nanocomposite dielectric materials with high thermal conductivity. *Proceedings of the IEEE*, 109 (8), p. 1364-1397.

This study reviews all of the above aspects of nanocomposite dielectric materials reported in literature. More specifically, we analyse various filler-polymer combinations, and the influence of approaches to incorporate fillers in the polymer on the thermal, mechanical and electrical properties. While the addition of fillers leads to huge enhancements in thermal conductivity, the thermal conductivity is highly anisotropic, with out of plane thermal conductivity lower than in plane thermal conductivity by an order of magnitude. It is seen that most present-day materials are still inadequate for future applications owing to their low glass transition temperatures; specific promising materials are highlighted. While the addition of fillers reduces the coefficient of thermal expansion, further reduction is needed to favourably improve the mechanical performance of these materials. While the electrical insulating properties of these composite materials are adequate, there is very little data reported on other electrical properties. In summary, while there is an understandable focus on enhancing the thermal conductivity, other properties are under-reported and there is insufficient information to support the assessment of most novel materials for practical applications. Overall, this study summarizes the state-of-the-art dielectric nanocomposites and outlines gaps for future research to bridge the gap between basic materials science and applications.

APPENDIX H: ASSESSING THE PERFORMANCE OF ADVANCED COOLING TECHNIQUES ON THERMAL MANAGEMENT OF NEXT-GENERATION POWER ELECTRONICS[11]

Abstract: Rapid miniaturization alongwith increasing heat loads in power electronics devices like insulated-gate bipolar transistors (IGBTs) have necessitated the need for advanced thermal management technologies in the packaging of these devices. This study quantifies the benefits of key advanced thermal management solutions for packaging of power electronics packages. Thermal resistance network modeling is used to estimate the maximum heat flux that can be dissipated by an IGBT package, while maintaining the junction temperature below 125 ^{o}C and 200 ^{o}C for silicon and silicon carbide (wide bandgap material) devices, respectively. While the model is completely analytical, it does address important complexities associated with heat flow in packages via the use of a sub-model to account for thermal spreading. The advanced cooling technologies evaluated in this study include the use of high thermal conductivity polymer heat sinks, double-sided heat sinking of packages, liquid cooling (single and two-phase), jet impingement and spray cooling. Additionally, combinations of these cooling technologies are evaluated as well. The heat dissipation achievable from these technologies is compared with that from an air-cooled copper heat sink (baseline). The results of this study provide insights and a starting point for selecting thermal management technologies (or combinations) based on the heat dissipation requirements of power electronics packages

[11] The content of this Appendix has been published in the following conference article: Acharya, P.V., Bahadur, V., Hebner, R., Ouroua, A. and Strank, S., 2019, October. Assessing the Performance of Advanced Cooling Techniques on Thermal Management of Next-Generation Power Electronics. In International Electronic Packaging Technical Conference and Exhibition (Vol. 59322, p. V001T06A001). American Society of Mechanical Engineers.

APPENDIX I: ESTIMATION OF FUEL QUALITY USING STATISTICAL REGRESSION -BASED ANALYSIS OF LEIDENFROST DROPLETS[12]

Abstract: Accurate measurement of fuel quality is critical for automotive applications as it impacts engine performance and emissions. A number of techniques have been proposed to measure fuel quality including acoustic wave speed sensors, chemometric modeling, near-infrared spectrophotometry, Raman spectroscopy etc. All of these techniques are complex in nature and require expensive equipment. In contrast, a novel, simple and rapid method for estimating fuel quality in field environments has been proposed in this work. This involves measuring the evaporation time of fuel droplets in the Leidenfrost state, and using the results of statistical data analysis conducted on an experimental data bank comprising evaporation time data for similar droplets. The Leidenfrost state refers to a liquid droplet hovering on its own vapor layer on a superheated surface. To showcase this approach, evaporation time was measured for droplets consisting of isopropyl alcohol (IPA) and water blends with varying parameters such as IPA fraction (0-1), droplet volume (20–100 μL) and surface temperature (200–340 °C). The resulting data bank (96 data points) was used to train and evaluate the performance of a polynomial regression (using a semilogarithmic transformation) model in predicting the evaporation time as a function of the above-mentioned parameters. R^2 accuracies of 97.34% (training data), 96.82% (test data), 97.46% (total) and a relative error within ± 0.25% for the entire dataset was obtained using the regression model, which highlights the predictive capabilities of this approach.

[12] The content of this Appendix has been published in the following conference article: Bhati, A., Acharya, P.V., Ezekoye, O.A. and Bahadur, V., 2021, June. Estimation of Fuel Quality Using Statistical Regression-Based Analysis of Leidenfrost Droplets. In Heat Transfer Summer Conference (Vol. 84874, p. V001T08A003). American Society of Mechanical Engineers.

References

[1] "Overview of Greenhouse Gases | US EPA." https://www.epa.gov/ghgemissions/overview-greenhouse-gases (accessed Sep. 11, 2021).

[2] H. J. Schellnhuber, S. Rahmstorf, and R. Winkelmann, "Why the right climate target was agreed in Paris," *Nat. Clim. Chang. 2016 67*, vol. 6, no. 7, pp. 649–653, Jun. 2016, doi: 10.1038/nclimate3013.

[3] J. Zheng, Z. R. Chong, M. F. Qureshi, and P. Linga, "Carbon Dioxide Sequestration via Gas Hydrates: A Potential Pathway toward Decarbonization," *Energy & Fuels*, vol. 34, no. 9, pp. 10529–10546, Sep. 2020, doi: 10.1021/ACS.ENERGYFUELS.0C02309.

[4] E. Dendy Sloan and C. Koh, "Clathrate Hydrates of Natural Gases, Third Edition," vol. 20074156, 2007, doi: 10.1201/9781420008494.

[5] L. Pauling and R. E. Marsh, "The Structure of Chlorine Hydrate," *Proc. Natl. Acad. Sci.*, vol. 38, no. 2, pp. 112–118, Feb. 1952, doi: 10.1073/pnas.38.2.112.

[6] W. F. Claussen, "A second water structure for inert gas hydrates," *The Journal of Chemical Physics*, vol. 19, no. 11. American Institute of PhysicsAIP, pp. 1425–1426, Nov. 22, 1951, doi: 10.1063/1.1748079.

[7] J. A. Ripmeester, J. S. Tse, C. I. Ratcliffe, and B. M. Powell, "A new clathrate hydrate structure," *Nature*, vol. 325, no. 6100, pp. 135–136, 1987, doi: 10.1038/325135a0.

[8] L. Jensen, "Experimental investigation and molecular simulation of gas hydrates.," Technical University of Denmark, 2010.

[9] P. V. Acharya and V. Bahadur, "Fundamental interfacial mechanisms underlying electrofreezing," *Adv. Colloid Interface Sci.*, vol. 251, pp. 26–43, Jan. 2018, doi: 10.1016/j.cis.2017.12.003.

[10] Y. Zhong and R. E. Rogers, "Surfactant effects on gas hydrate formation," *Chem. Eng. Sci.*, vol. 55, no. 19, pp. 4175–4187, Oct. 2000, doi: 10.1016/S0009-2509(00)00072-5.

[11] J. S. Zhang, S. Lee, and J. W. Lee, "Kinetics of methane hydrate formation from SDS solution," *Ind. Eng. Chem. Res.*, vol. 46, no. 19, pp. 6353–6359, Sep. 2007, doi: 10.1021/ie070627r.

[12] H. Ganji, M. Manteghian, K. Sadaghiani zadeh, M. R. Omidkhah, and H. Rahimi Mofrad, “Effect of different surfactants on methane hydrate formation rate, stability and storage capacity,” *Fuel*, vol. 86, no. 3, pp. 434–441, Feb. 2007, doi: 10.1016/j.fuel.2006.07.032.

[13] N. Ando, Y. Kuwabara, and Y. H. Mori, “Surfactant effects on hydrate formation in an unstirred gas/liquid system: An experimental study using methane and micelle-forming surfactants,” *Chem. Eng. Sci.*, vol. 73, pp. 79–85, May 2012, doi: 10.1016/j.ces.2012.01.038.

[14] C. A. Koh, E. D. Sloan, A. K. Sum, and D. T. Wu, “Fundamentals and applications of gas hydrates,” *Annu. Rev. Chem. Biomol. Eng.*, vol. 2, pp. 237–257, 2011.

[15] J.-H. Sa, B. R. Lee, D.-H. Park, K. Han, H. D. Chun, and K.-H. Lee, “Amino Acids as Natural Inhibitors for Hydrate Formation in CO2 Sequestration,” *Environ. Sci. Technol.*, vol. 45, no. 13, pp. 5885–5891, Jul. 2011, doi: 10.1021/ES200552C.

[16] H. R. Pruppacher, “The effects of electric fields on cloud physical processes,” *Zeitschrift für Angew. Math. und Phys. ZAMP 1963 145*, vol. 14, no. 5, pp. 590–599, Sep. 1963, doi: 10.1007/BF01601266.

[17] M. Farzaneh, “Ice accretions on highvoltage conductors and insulators and related phenomena,” *Philos. Trans. R. Soc. London. Ser. A Math. Phys. Eng. Sci.*, vol. 358, no. 1776, pp. 2971–3005, Nov. 2000, doi: 10.1098/RSTA.2000.0692.

[18] V. J. Schaefer and I. Langmuir, *Project cirrus*. 1953.

[19] R. P. Hans, “The effect of an external electric field on the supercooling of water drops,” *J. Geophys. Res.*, vol. 68, no. 15, pp. 4463–4474, Aug. 1963, doi: 10.1029/JZ068I015P04463.

[20] L. B. Loeb, “A tentative explanation of the electrical field effect on the freezing of supercooled water drops,” *J. Geophys. Res.*, vol. 68, no. 15, pp. 4475–4476, Aug. 1963, doi: 10.1029/JZ068I015P04475.

[21] M. A. Abbas and J. Latham, “The Electrofreezing of Supercooled Water Drops,” *J. Meteorol. Soc. Japan. Ser. II*, vol. 47, no. 2, pp. 65–74, 1969, doi: 10.2151/JMSJ1965.47.2_65.

[22] L. R. Koenig, “Drop Freezing Through Drop Breakup,” *J. Atmos. Sci.*, vol. 22, no. 4, pp. 448–451, Jul. 1965, doi: 10.1175/1520-0469(1965)022<0448:DFTDB>2.0.CO;2.

[23] M. H. Smith, R. F. Griffiths, and J. Latham, “The freezing of raindrops falling through strong electric fields,” *Q. J. R. Meteorol. Soc.*, vol. 97, no. 414, pp. 495–505, Oct. 1971, doi: 10.1002/QJ.49709741409.

[24] H. R. Pruppacher, “Electrofreezing of supercooled water,” *pure Appl. Geophys. 1973 1041*, vol. 104, no. 1, pp. 623–634, Dec. 1973, doi: 10.1007/BF00875907.

[25] L. F. Evans, “The role of the adsorbed layer in ice nucleation,” 1970.

[26] X. Xia and M. L. Berkowitz, “Electric-Field Induced Restructuring of Water at a Platinum-Water Interface: A Molecular Dynamics Computer Simulation,” *Phys. Rev. Lett.*, vol. 74, no. 16, p. 3193, Apr. 1995, doi: 10.1103/PhysRevLett.74.3193.

[27] J. Y. Yan and G. N. Patey, “Heterogeneous Ice Nucleation Induced by Electric Fields,” *J. Phys. Chem. Lett.*, vol. 2, no. 20, pp. 2555–2559, Oct. 2011, doi: 10.1021/JZ201113M.

[28] X. X. Zhang, M. Chen, and M. Fu, “Icing of water on polyethylene surfaces,” *Appl. Surf. Sci.*, vol. 313, pp. 771–776, Sep. 2014, doi: 10.1016/J.APSUSC.2014.06.070.

[29] I. C. Yeh and M. L. Berkowitz, “Structure and dynamics of water at water|Pt interface as seen by molecular dynamics computer simulation,” *J. Electroanal. Chem.*, vol. 450, no. 2, pp. 313–325, Jun. 1998, doi: 10.1016/S0022-0728(97)00654-2.

[30] W. Rau, “Eiskeimbildung durch dielektrische Polarisation,” *Zeitschrift für Naturforsch. A*, vol. 6, no. 11, pp. 649–657, Nov. 1951, doi: 10.1515/ZNA-1951-1115.

[31] R. W. Salt, “Effect of electrostatic field on freezing of supercooled water and insects,” *Science (80-.).*, vol. 133, no. 3451, pp. 458–459, 1961, doi: 10.1126/SCIENCE.133.3451.458.

[32] T. G. Gabarashvili and N. V Gliki, “Origination of the ice phase in supercooled water under the influence of electrically charged crystals. Izvestiya Acad. Sci: USSR,” *Atmos. Ocean. Phys.*, vol. 3, pp. 324–327, 1967.

[33] G. A. Dawson and G. R. Cardell, “Electrofreezing of supercooled waterdrops,” *J. Geophys. Res.*, vol. 78, no. 36, pp. 8864–8866, Dec. 1973, doi: 10.1029/JC078I036P08864.

[34] J. B. Doolittle and G. Vali, “Heterogeneous freezing nucleation in electric fields,”

J. Atmos. Sci., vol. 32, no. 2, pp. 375–379, 1975.

[35] T. Shichiri and T. Nagata, "Effect of electric currents on the nucleation of ice crystals in the melt," *J. Cryst. Growth*, vol. 54, no. 2, pp. 207–210, Aug. 1981, doi: 10.1016/0022-0248(81)90461-9.

[36] S. Sivanesan and R. Gobinathan, "Ice nucleation of AgI — CuBr nucleants in the presence of electric field," *Mater. Chem. Phys.*, vol. 27, no. 4, pp. 385–392, Apr. 1991, doi: 10.1016/0254-0584(91)90135-H.

[37] T. Shichiri and Y. Araki, "Nucleation mechanism of ice crystals under electrical effect," *J. Cryst. Growth*, vol. 78, no. 3, pp. 502–508, Dec. 1986, doi: 10.1016/0022-0248(86)90152-1.

[38] H. R. Pruppacher and J. D. Klett, *Microphysics of Clouds and Precipitation: Reprinted 1980*. Springer Science & Business Media, 2012.

[39] M. Gavish, J.-L. Wang, M. Eisenstein, M. Lahav, and L. Leiserowitz, "The role of crystal polarity in α-amino acid crystals for induced nucleation of ice," *Science (80-.).*, vol. 256, no. 5058, pp. 815–818, 1992.

[40] I. Braslavsky and S. G. Lipson, "Electrofreezing effect and nucleation of ice crystals in free growth experiments," *Appl. Phys. Lett.*, vol. 72, no. 2, p. 264, Jun. 1998, doi: 10.1063/1.120705.

[41] T. Hozumi, A. Saito, S. Okawa, and K. Watanabe, "Effects of electrode materials on freezing of supercooled water in electric freeze control," *Int. J. Refrig.*, vol. 26, no. 5, pp. 537–542, Aug. 2003, doi: 10.1016/S0140-7007(03)00008-2.

[42] T. Hozumi, A. Saito, S. Okawa, and Y. Eshita, "Effects of shapes of electrodes on freezing of supercooled water in electric freeze control," *Int. J. Refrig.*, vol. 28, no. 3, pp. 389–395, May 2005, doi: 10.1016/J.IJREFRIG.2004.08.009.

[43] E.-M. Choi, Y.-H. Yoon, S. Lee, and H. Kang, "Freezing Transition of Interfacial Water at Room Temperature under Electric Fields," *Phys. Rev. Lett.*, vol. 95, no. 8, p. 085701, Aug. 2005, doi: 10.1103/PhysRevLett.95.085701.

[44] H. A. Kotodziej, G. Parry Jones, and Mansel Davies, "High field dielectric measurements in water," *J. Chem. Soc. Faraday Trans. 2 Mol. Chem. Phys.*, vol. 71, no. 0, pp. 269–274, Jan. 1975, doi: 10.1039/F29757100269.

[45] C. Song and P. Wang, "High electric field effects on gigahertz dielectric properties of water measured with microwave microfluidic devices," *Rev. Sci. Instrum.*, vol.

81, no. 5, p. 054702, May 2010, doi: 10.1063/1.3405975.

[46] L. D. Landau, J. S. Bell, M. J. Kearsley, L. P. Pitaevskii, E. M. Lifshitz, and J. B. Sykes, *Electrodynamics of continuous media*, vol. 8. elsevier, 2013.

[47] C. A. Stan, S. K. Y. Tang, K. J. M. Bishop, and G. M. Whitesides, "Externally Applied Electric Fields up to 1.6 × 105 V/m Do Not Affect the Homogeneous Nucleation of Ice in Supercooled Water," *J. Phys. Chem. B*, vol. 115, no. 5, pp. 1089–1097, Feb. 2010, doi: 10.1021/JP110437X.

[48] F. Mugele and J. C. Baret, "Electrowetting: From basics to applications," *Journal of Physics Condensed Matter*, vol. 17, no. 28. IOP Publishing, p. R705, Jul. 20, 2005, doi: 10.1088/0953-8984/17/28/R01.

[49] NakajimaAkira *et al.*, "Effect of Electrification Conditions on the Freezing of Supercooled Water Droplets on a Hydrophobic Coating," *http://dx.doi.org/10.1246/cl.2007.1020*, vol. 36, no. 8, pp. 1020–1021, Jul. 2007, doi: 10.1246/CL.2007.1020.

[50] D. Rzesanke, J. Nadolny, D. Duft, R. Müller, A. Kiselev, and T. Leisner, "On the role of surface charges for homogeneous freezing of supercooled water microdroplets," *Phys. Chem. Chem. Phys.*, vol. 14, no. 26, pp. 9359–9363, Jun. 2012, doi: 10.1039/C2CP23653B.

[51] F. Yang, R. A. Shaw, C. W. Gurganus, S. K. Chong, and Y. K. Yap, "Ice nucleation at the contact line triggered by transient electrowetting fields," *Appl. Phys. Lett.*, vol. 107, no. 26, p. 264101, Dec. 2015, doi: 10.1063/1.4938749.

[52] K. Carpenter and V. Bahadur, "Electrofreezing of Water Droplets under Electrowetting Fields," *Langmuir*, vol. 31, no. 7, pp. 2243–2248, Feb. 2015, doi: 10.1021/la504792n.

[53] T. Shichiri and T. Nagata, "Effect of electric currents on the nucleation of ice crystals in the melt," *J. Cryst. Growth*, vol. 54, no. 2, pp. 207–210, Aug. 1981, doi: 10.1016/0022-0248(81)90461-9.

[54] K. Carpenter and V. Bahadur, "Electronucleation for Rapid and Controlled Formation of Hydrates," *J. Phys. Chem. Lett.*, vol. 7, no. 13, pp. 2465–2469, Jul. 2016, doi: 10.1021/acs.jpclett.6b01166.

[55] P. Linga, R. Kumar, and P. Englezos, "Gas hydrate formation from hydrogen/carbon dioxide and nitrogen/carbon dioxide gas mixtures," *Chem. Eng. Sci.*, 2007, doi: 10.1016/j.ces.2007.04.033.

[56] S. Li, S. Fan, J. Wang, X. Lang, and D. Liang, “CO2 capture from binary mixture via forming hydrate with the help of tetra-n-butyl ammonium bromide,” *J. Nat. Gas Chem.*, vol. 18, no. 1, pp. 15–20, Mar. 2009, doi: 10.1016/S1003-9953(08)60085-7.

[57] P. Skovborg, H. J. Ng, P. Rasmussen, and U. Mohn, “Measurement of induction times for the formation of methane and ethane gas hydrates,” *Chem. Eng. Sci.*, vol. 48, no. 3, pp. 445–453, Feb. 1993, doi: 10.1016/0009-2509(93)80299-6.

[58] W. Hao, J. Wang, S. Fan, and W. Hao, “Study on methane hydration process in a semi-continuous stirred tank reactor,” *Energy Convers. Manag.*, vol. 48, no. 3, pp. 954–960, Mar. 2007, doi: 10.1016/J.ENCONMAN.2006.08.007.

[59] S. Dai, J. Y. Lee, and J. C. Santamarina, “Hydrate nucleation in quiescent and dynamic conditions,” *Fluid Phase Equilib.*, vol. 378, pp. 107–112, Sep. 2014, doi: 10.1016/j.fluid.2014.07.006.

[60] L. Jensen, K. Thomsen, and N. von Solms, “Propane hydrate nucleation: Experimental investigation and correlation,” *Chem. Eng. Sci.*, vol. 63, no. 12, pp. 3069–3080, Jun. 2008, doi: 10.1016/J.CES.2008.03.006.

[61] *,† Ryo Ohmura, Shigetoyo Kashiwazaki, Saburo Shiota, and Hideyuki Tsuji, and Y. H. Mori, “Structure-I and Structure-H Hydrate Formation Using Water Spraying,” *Energy and Fuels*, vol. 16, no. 5, pp. 1141–1147, Sep. 2002, doi: 10.1021/EF0200727.

[62] K. Fukumoto, J. Tobe, R. Ohmura, and Y. H. Mori, “Hydrate formation using water spraying in a hydrophobic gas: a preliminary study,” *Am. Inst. Chem. Eng. AIChE J.*, vol. 47, no. 8, p. 1899, 2001.

[63] C. F. da S. Lirio, F. L. P. Pessoa, and A. M. C. Uller, “Storage capacity of carbon dioxide hydrates in the presence of sodium dodecyl sulfate (SDS) and tetrahydrofuran (THF),” *Chem. Eng. Sci.*, 2013, doi: 10.1016/j.ces.2012.10.022.

[64] M. Rahmati-Abkenar, M. Manteghian, and H. Pahlavanzadeh, “Experimental and theoretical investigation of methane hydrate induction time in the presence of triangular silver nanoparticles,” *Chem. Eng. Res. Des.*, vol. 120, pp. 325–332, Apr. 2017, doi: 10.1016/j.cherd.2017.02.023.

[65] S. Arjang, M. Manteghian, and A. Mohammadi, “Effect of synthesized silver nanoparticles in promoting methane hydrate formation at 4.7MPa and 5.7MPa,” *Chem. Eng. Res. Des.*, vol. 91, no. 6, pp. 1050–1054, Jun. 2013, doi: 10.1016/j.cherd.2012.12.001.

[66] H. Najibi, M. Mirzaee Shayegan, and H. Heidary, “Experimental investigation of methane hydrate formation in the presence of copper oxide nanoparticles and SDS,” *J. Nat. Gas Sci. Eng.*, vol. 23, pp. 315–323, Mar. 2015, doi: 10.1016/j.jngse.2015.02.009.

[67] M. Rahmati-Abkenar, M. Manteghian, and H. Pahlavanzadeh, “Nucleation of ethane hydrate in water containing silver nanoparticles,” *Mater. Des.*, vol. 126, pp. 190–196, Jul. 2017, doi: 10.1016/j.matdes.2017.04.051.

[68] A. Mohammadi, M. Manteghian, A. Haghtalab, A. H. Mohammadi, and M. Rahmati-Abkenar, “Kinetic study of carbon dioxide hydrate formation in presence of silver nanoparticles and SDS,” *Chem. Eng. J.*, 2014, doi: 10.1016/j.cej.2013.09.026.

[69] L. Yang, S. Fan, Y. Wang, X. Lang, and D. Xie, “Accelerated formation of methane hydrate in aluminum foam,” *Ind. Eng. Chem. Res.*, vol. 50, no. 20, pp. 11563–11569, Oct. 2011, doi: 10.1021/ie200825e.

[70] S. Fan, L. Yang, X. Lang, Y. Wang, and D. Xie, “Kinetics and thermal analysis of methane hydrate formation in aluminum foam,” *Chem. Eng. Sci.*, vol. 82, pp. 185–193, Sep. 2012, doi: 10.1016/j.ces.2012.07.040.

[71] X. Liu, L. Tian, D. Chen, and G. Wu, “Accelerated formation of methane hydrates in the porous SiC foam ceramic packed reactor,” *Fuel*, vol. 257, p. 115858, Dec. 2019, doi: 10.1016/j.fuel.2019.115858.

[72] Y. T. Seo, I. L. Moudrakovski, J. A. Ripmeester, J. W. Lee, and H. Lee, “Efficient recovery of CO2from flue gas by clathrate hydrate formation in porous silica gels,” *Environ. Sci. Technol.*, 2005, doi: 10.1021/es049269z.

[73] A. Adeyemo, R. Kumar, P. Linga, J. Ripmeester, and P. Englezos, “Capture of carbon dioxide from flue or fuel gas mixtures by clathrate crystallization in a silica gel column,” *Int. J. Greenh. Gas Control*, vol. 4, no. 3, pp. 478–485, May 2010, doi: 10.1016/j.ijggc.2009.11.011.

[74] X. Sun and K. K. Mohanty, “Kinetic simulation of methane hydrate formation and dissociation in porous media,” *Chem. Eng. Sci.*, vol. 61, no. 11, pp. 3476–3495, Jun. 2006, doi: 10.1016/j.ces.2005.12.017.

[75] Y. T. Seo, I. L. Moudrakovski, J. A. Ripmeester, J. W. Lee, and H. Lee, “Efficient recovery of CO2 from flue gas by clathrate hydrate formation in porous silica gels,” *Environ. Sci. Technol.*, vol. 39, no. 7, pp. 2315–2319, Apr. 2005, doi: 10.1021/es049269z.

[76] Y. P. Handa and D. Y. Stupin, “Thermodynamic properties and dissociation characteristics of methane and propane hydrates in 70-. ANG.-radius silica gel pores,” *J. Phys. Chem.*, vol. 96, no. 21, pp. 8599–8603, 1992.

[77] S. P. Kang and J. W. Lee, “Kinetic behaviors of CO2 hydrates in porous media and effect of kinetic promoter on the formation kinetics,” *Chem. Eng. Sci.*, vol. 65, no. 5, pp. 1840–1845, Mar. 2010, doi: 10.1016/J.CES.2009.11.027.

[78] T. Uchida, T. Ebinuma, S. Takeya, J. Nagao, and H. Narita, “Effects of pore sizes on dissociation temperatures and pressures of methane, carbon dioxide, and propane hydrates in porous media,” *J. Phys. Chem. B*, 2002, doi: 10.1021/jp012823w.

[79] M. Yang, Y. Song, L. Jiang, W. Liu, B. Dou, and W. Jing, “Effects of operating mode and pressure on hydrate-based desalination and CO2 capture in porous media,” *Appl. Energy*, vol. 135, pp. 504–511, Dec. 2014, doi: 10.1016/J.APENERGY.2014.08.095.

[80] W. Liu, S. Wang, M. Yang, Y. Song, S. Wang, and J. Zhao, “Investigation of the induction time for THF hydrate formation in porous media,” *J. Nat. Gas Sci. Eng.*, vol. 24, pp. 357–364, May 2015, doi: 10.1016/J.JNGSE.2015.03.030.

[81] Z. Liu, Z. Pan, Z. Zhang, P. Liu, L. Shang, and B. Li, “Effect of Porous Media and Sodium Dodecyl Sulphate Complex System on Methane Hydrate Formation,” *Energy & Fuels*, vol. 32, no. 5, pp. 5736–5749, May 2018, doi: 10.1021/ACS.ENERGYFUELS.8B00041.

[82] S. D. Zhou, Y. S. Yu, M. M. Zhao, S. L. Wang, and G. Z. Zhang, “Effect of graphite nanoparticles on promoting CO2 hydrate formation,” 2014, doi: 10.1021/ef5000886.

[83] S. Zhou, K. Jiang, Y. Zhao, Y. Chi, S. Wang, and G. Zhang, “Experimental Investigation of CO2 Hydrate Formation in the Water Containing Graphite Nanoparticles and Tetra-n-butyl Ammonium Bromide,” *J. Chem. Eng. Data*, vol. 63, no. 2, pp. 389–394, Feb. 2018, doi: 10.1021/ACS.JCED.7B00785.

[84] A. Kumar, T. Sakpal, P. Linga, and R. Kumar, “Enhanced carbon dioxide hydrate formation kinetics in a fixed bed reactor filled with metallic packing,” *Chem. Eng. Sci.*, vol. 122, pp. 78–85, Jan. 2015, doi: 10.1016/J.CES.2014.09.019.

[85] L. Shi, L. Yi, X. Shen, W. Wu, and D. Liang, “The effect of tetrabutylphosphonium bromide on the formation process of CO2 hydrates,” *J. Mol. Liq.*, vol. 229, pp. 98–105, Mar. 2017, doi: 10.1016/J.MOLLIQ.2016.12.038.

[86] C. B. Bavoh, B. Lal, H. Osei, K. M. Sabil, and H. Mukhtar, “A review on the role of amino acids in gas hydrate inhibition, CO2 capture and sequestration, and natural gas storage,” *J. Nat. Gas Sci. Eng.*, vol. 64, pp. 52–71, Apr. 2019, doi: 10.1016/J.JNGSE.2019.01.020.

[87] J.-H. Sa *et al.*, “Inhibition of methane and natural gas hydrate formation by altering the structure of water with amino acids,” *Sci. Reports 2016 61*, vol. 6, no. 1, pp. 1–9, Aug. 2016, doi: 10.1038/srep31582.

[88] C. B. Bavoh, B. Partoon, B. Lal, and L. Kok Keong, “Methane hydrate-liquid-vapour-equilibrium phase condition measurements in the presence of natural amino acids,” *J. Nat. Gas Sci. Eng.*, vol. 37, pp. 425–434, Jan. 2017, doi: 10.1016/J.JNGSE.2016.11.061.

[89] C. B. Bavoh, B. Partoon, B. Lal, G. Gonfa, S. Foo Khor, and A. M. Sharif, “Inhibition effect of amino acids on carbon dioxide hydrate,” *Chem. Eng. Sci.*, vol. 171, pp. 331–339, Nov. 2017, doi: 10.1016/J.CES.2017.05.046.

[90] M. Aresta, A. Dibenedetto, and E. Quaranta, “Reaction mechanisms in carbon dioxide conversion,” 2016.

[91] J. R. DuQuesnay, M. C. Diaz Posada, and J. G. Beltran, “Novel gas hydrate reactor design: 3-in-1 assessment of phase equilibria, morphology and kinetics,” *Fluid Phase Equilib.*, vol. 413, pp. 148–157, Apr. 2016, doi: 10.1016/J.FLUID.2015.11.006.

[92] L. U. Udegbunam, J. R. DuQuesnay, L. Osorio, V. K. Walker, and J. G. Beltran, “Phase equilibria, kinetics and morphology of methane hydrate inhibited by antifreeze proteins: application of a novel 3-in-1 method,” *J. Chem. Thermodyn.*, vol. 117, pp. 155–163, Feb. 2018, doi: 10.1016/J.JCT.2017.08.015.

[93] D. B. Carson and D. L. Katz, “Natural gas hydrates,” in *Transactions of the AIME,146(01)*, 1942, pp. 150–158.

[94] D. L. Katz, “Prediction of Conditions for Hydrate Formation in Natural Gases,” *Trans. AIME*, vol. 160, no. 01, pp. 140–149, Dec. 1945, doi: 10.2118/945140-g.

[95] J. Loh, R. N. Maddox, and J. H. Erbar, “NEW HYDRATE-FORMATION DATA REVEAL DIFFERENCES,” *OIL GAS J.*, vol. 81, no. 20, pp. 96–98, 1983.

[96] E. D. SLOAN, “Phase equilibria of natural gas hydrates.” pp. 163–169, 1984.

[97] B. K. Berge, “Hydrate Predictions on a Microcomputer,” Apr. 1986, doi:

10.2118/15306-MS.

[98] R. Kobayashi, K. Y. Song, and E. D. Sloan, “Phase Behavior of Water/Hydrocarbon Systems,” in *Petroleum Engineering Handbook*, 1987.

[99] A. Bahadori and H. B. Vuthaluru, “A novel correlation for estimation of hydrate forming condition of natural gases,” *J. Nat. Gas Chem.*, vol. 18, no. 4, pp. 453–457, Dec. 2009, doi: 10.1016/S1003-9953(08)60143-7.

[100] M. M. Ghiasi, “Initial estimation of hydrate formation temperature of sweet natural gases based on new empirical correlation,” *J. Nat. Gas Chem.*, vol. 21, no. 5, pp. 508–512, Sep. 2012, doi: 10.1016/S1003-9953(11)60398-8.

[101] G. D. Holder, S. P. Zetts, and N. Pradhan, “Phase Behavior in Systems Containing Clathrate Hydrates: A Review,” *Rev. Chem. Eng.*, vol. 5, no. 1–4, 1988.

[102] J. H. van der Waals and J. C. Platteeuw, “Clathrate Solutions,” John Wiley & Sons, Ltd, 2007, pp. 1–57.

[103] W. R. Parrish and J. M. Prausnitz, “Dissociation Pressures of Gas Hydrates Formed by Gas Mixtures,” *Ind. Eng. Chem. Process Des. Dev.*, vol. 11, no. 1, pp. 26–35, Jan. 1972, doi: 10.1021/i260041a006.

[104] J. Javanmardi, M. Moshfeghian, and R. N. Maddox, “Simple method for predicting gas-hydrate-forming conditions in aqueous mixed-electrolyte solutions,” *Energy and Fuels*, vol. 12, no. 2, pp. 219–222, 1998, doi: 10.1021/ef9701652.

[105] J. Javanmardi, M. Moshfeghian, and R. N. Maddox, “An accurate model for prediction of gas hydrate formation conditions in mixtures of aqueous electrolyte solutions and alcohol,” *Can. J. Chem. Eng.*, vol. 79, no. 3, pp. 367–373, Jun. 2001, doi: 10.1002/cjce.5450790309.

[106] D. Shabani, M.M., Rashtchian, C. Ghotbi, V. Taghikhani, and G. KHAYAT, “PREDICTION OF HYDRATE FORMATION FOR THE SYSTEMS CONTAINING SINGLE AND MIXED ELECTROLYTE SOLUTIONS,” *Iran. J. Chem. Chem. Eng.*, vol. 26, no. 1, pp. 35–45, 2007.

[107] H. Tavasoli, F. Feyzi, M. R. Dehghani, and F. Alavi, “Prediction of gas hydrate formation condition in the presence of thermodynamic inhibitors with the Elliott–Suresh–Donohue Equation of State,” *J. Pet. Sci. Eng.*, vol. 77, no. 1, pp. 93–103, Apr. 2011, doi: 10.1016/j.petrol.2011.02.002.

[108] P. F. Ferrari, A. Z. Guembaroski, M. A. Marcelino Neto, R. E. M. Morales, and A.

K. Sum, “Experimental measurements and modelling of carbon dioxide hydrate phase equilibrium with and without ethanol,” *Fluid Phase Equilib.*, vol. 413, pp. 176–183, Apr. 2016, doi: 10.1016/j.fluid.2015.10.008.

[109] H. Delavar and A. Haghtalab, “Thermodynamic modeling of gas hydrate formation conditions in the presence of organic inhibitors, salts and their mixtures using UNIQUAC model,” *Fluid Phase Equilib.*, vol. 394, pp. 101–117, May 2015, doi: 10.1016/j.fluid.2015.03.008.

[110] T. H. Sirino, M. A. Marcelino Neto, D. Bertoldi, R. E. M. Morales, and A. K. Sum, “Multiphase flash calculations for gas hydrates systems,” *Fluid Phase Equilib.*, vol. 475, pp. 45–63, Nov. 2018, doi: 10.1016/j.fluid.2018.07.029.

[111] H. Najibi, A. Chapoy, H. Haghighi, and B. Tohidi, “Experimental determination and prediction of methane hydrate stability in alcohols and electrolyte solutions,” *Fluid Phase Equilib.*, vol. 275, no. 2, pp. 127–131, Jan. 2009, doi: 10.1016/j.fluid.2008.09.020.

[112] M. A. Mahabadian, A. Chapoy, R. Burgass, and B. Tohidi, “Development of a multiphase flash in presence of hydrates: Experimental measurements and validation with the CPA equation of state,” *Fluid Phase Equilib.*, vol. 414, pp. 117–132, Apr. 2016, doi: 10.1016/j.fluid.2016.01.009.

[113] S. Shahnazar and N. Hasan, “Gas hydrate formation condition: Review on experimental and modeling approaches,” *Fluid Phase Equilib.*, vol. 379, pp. 72–85, Oct. 2014, doi: 10.1016/j.fluid.2014.07.012.

[114] I. A. Basheer and M. Hajmeer, “Artificial neural networks: Fundamentals, computing, design, and application,” *J. Microbiol. Methods*, vol. 43, no. 1, pp. 3–31, Dec. 2000, doi: 10.1016/S0167-7012(00)00201-3.

[115] M. Paliwal and U. A. Kumar, “Neural networks and statistical techniques: A review of applications,” *Expert Systems with Applications*, vol. 36, no. 1. Pergamon, pp. 2–17, Jan. 01, 2009, doi: 10.1016/j.eswa.2007.10.005.

[116] K. P. Ferentinos, “Biological engineering applications of feedforward neural networks designed and parameterized by genetic algorithms,” *Neural Networks*, vol. 18, no. 7, pp. 934–950, Sep. 2005, doi: 10.1016/j.neunet.2005.03.010.

[117] A. A. Elgibaly and A. M. Elkamel, “A new correlation for predicting hydrate formation conditions for various gas mixtures and inhibitors,” *Fluid Phase Equilib.*, vol. 152, no. 1, pp. 23–42, Oct. 1998, doi: 10.1016/S0378-3812(98)00368-9.

[118] A. Elgibaly and A. Elkamel, “Optimal hydrate inhibition policies with the aid of neural networks,” *Energy and Fuels*, vol. 13, no. 1, pp. 105–113, 1999, doi: 10.1021/ef980129i.

[119] G. Zahedi, Z. Karami, and H. Yaghoobi, “Prediction of hydrate formation temperature by both statistical models and artificial neural network approaches,” *Energy Convers. Manag.*, vol. 50, no. 8, pp. 2052–2059, Aug. 2009, doi: 10.1016/j.enconman.2009.04.005.

[120] A. Chapoy, A. H. Mohammadi, and D. Richon, “Predicting the Hydrate Stability Zones of Natural Gases Using Artificial Neural Networks,” *Oil Gas Sci. Technol. - Rev. l’IFP*, vol. 62, no. 5, pp. 701–706, Sep. 2007, doi: 10.2516/ogst:2007048.

[121] M. Ghavipour, M. Ghavipour, M. Chitsazan, S. H. Najibi, and S. S. Ghidary, “Experimental study of natural gas hydrates and a novel use of neural network to predict hydrate formation conditions,” *Chem. Eng. Res. Des.*, vol. 91, no. 2, pp. 264–273, Feb. 2013, doi: 10.1016/j.cherd.2012.08.010.

[122] Y. Song, H. Zhou, P. Wang, and M. Yang, “Prediction of clathrate hydrate phase equilibria using gradient boosted regression trees and deep neural networks,” *J. Chem. Thermodyn.*, vol. 135, pp. 86–96, Aug. 2019, doi: 10.1016/j.jct.2019.03.030.

[123] H. Yarveicy and M. M. Ghiasi, “Modeling of gas hydrate phase equilibria: Extremely randomized trees and LSSVM approaches,” *J. Mol. Liq.*, vol. 243, pp. 533–541, Oct. 2017, doi: 10.1016/j.molliq.2017.08.053.

[124] M. Mesbah, E. Soroush, and M. Rezakazemi, “Development of a least squares support vector machine model for prediction of natural gas hydrate formation temperature,” *Chinese J. Chem. Eng.*, vol. 25, no. 9, pp. 1238–1248, Sep. 2017, doi: 10.1016/j.cjche.2016.09.007.

[125] M. M. Ghiasi, H. Yarveicy, M. Arabloo, A. H. Mohammadi, and R. M. Behbahani, “Modeling of stability conditions of natural gas clathrate hydrates using least squares support vector machine approach,” *J. Mol. Liq.*, vol. 223, pp. 1081–1092, Nov. 2016, doi: 10.1016/j.molliq.2016.09.009.

[126] A. H. Mohammadi and D. Richon, “Determination of gas hydrate safety margin using specific gravity data of salt or organic inhibitor aqueous solution,” *Ind. Eng. Chem. Res.*, vol. 46, no. 11, pp. 3852–3857, May 2007, doi: 10.1021/ie060908j.

[127] A. H. Mohammadi, J. F. Martínez-López, and D. Richon, “Determination of hydrate stability zone using electrical conductivity data of salt aqueous solution,”

Fluid Phase Equilib., vol. 253, no. 1, pp. 36–41, Apr. 2007, doi: 10.1016/j.fluid.2007.01.006.

[128] P. W. Wilson, D. Lester, and A. D. J. Haymet, "Heterogeneous nucleation of clathrates from supercooled tetrahydrofuran (THF)/water mixtures, and the effect of an added catalyst," *Chem. Eng. Sci.*, vol. 60, no. 11, pp. 2937–2941, Jun. 2005, doi: 10.1016/j.ces.2004.12.047.

[129] J. S. Zhang, C. Lo, P. Somasundaran, S. Lu, A. Couzis, and J. W. Lee, "Adsorption of Sodium Dodecyl Sulfate at THF Hydrate/Liquid Interface," *J. Phys. Chem. C*, vol. 112, no. 32, pp. 12381–12385, Aug. 2008, doi: 10.1021/JP801963C.

[130] P. W. Wilson and A. D. J. Haymet, "Hydrate formation and re-formation in nucleating THF/water mixtures show no evidence to support a 'memory' effect," *Chem. Eng. J.*, vol. 161, no. 1–2, pp. 146–150, Jul. 2010, doi: 10.1016/J.CEJ.2010.04.047.

[131] E. Tombari, S. Presto, G. Salvetti, and G. P. Johari, "Heat capacity of tetrahydrofuran clathrate hydrate and of its components, and the clathrate formation from supercooled melt," *J. Chem. Phys.*, vol. 124, no. 15, p. 154507, Apr. 2006, doi: 10.1063/1.2188944.

[132] S. Bauerecker, P. Ulbig, V. Buch, L. Vrbka, and P. Jungwirth, "Monitoring Ice Nucleation in Pure and Salty Water via High-Speed Imaging and Computer Simulations," *J. Phys. Chem. C*, vol. 112, no. 20, pp. 7631–7636, May 2008, doi: 10.1021/jp711507f.

[133] A. Alizadeh *et al.*, "Dynamics of Ice Nucleation on Water Repellent Surfaces," *Langmuir*, vol. 28, no. 6, pp. 3180–3186, Feb. 2012, doi: 10.1021/la2045256.

[134] T. Hozumi, A. Saito, S. Okawa, and K. Watanabe, "Effects of electrode materials on freezing of supercooled water in electric freeze control," *Int. J. Refrig.*, vol. 26, no. 5, pp. 537–542, Aug. 2003, doi: 10.1016/S0140-7007(03)00008-2.

[135] M. B. Hay and S. C. B. Myneni, "Geometric and Electronic Structure of the Aqueous $Al(H_2O)_6^{3+}$ Complex," *J. Phys. Chem. A*, vol. 112, no. 42, pp. 10595–10603, Oct. 2008, doi: 10.1021/jp802675v.

[136] M. B. Hay and S. C. B. Myneni, "X-ray Absorption Spectroscopy of Aqueous Aluminum-Organic Complexes," *J. Phys. Chem. A*, vol. 114, no. 20, pp. 6138–6148, May 2010, doi: 10.1021/JP909656Q.

[137] W. W. Rudolph, Roger Mason, and C. C. Pye, “Aluminium(III) hydration in aqueous solution. A Raman spectroscopic investigation and an ab initio molecular orbital study of aluminium(III) water clusters,” *Phys. Chem. Chem. Phys.*, vol. 2, no. 22, pp. 5030–5040, Jan. 2000, doi: 10.1039/B003764H.

[138] I. Narin, M. Tuzen, and M. Soylak, “Aluminium determination in environmental samples by graphite furnace atomic absorption spectrometry after solid phase extraction on Amberlite XAD-1180/pyrocatechol violet chelating resin,” *Talanta*, vol. 63, no. 2, pp. 411–418, May 2004, doi: 10.1016/J.TALANTA.2003.11.005.

[139] I. Narin, M. Soylak, L. Elçi, and M. Doğan, “Determination of trace metal ions by AAS in natural water samples after preconcentration of pyrocatechol violet complexes on an activated carbon column,” *Talanta*, vol. 52, no. 6, pp. 1041–1046, Sep. 2000, doi: 10.1016/S0039-9140(00)00468-9.

[140] P. K. David Reay, Ryan McGlen, *Heat Pipes Theory, Design and Applications*. Elsevier Science, 2013.

[141] P. Servio and P. Englezos, “Morphology of methane and carbon dioxide hydrates formed from water droplets,” *AIChE J.*, vol. 49, no. 1, pp. 269–276, 2003, doi: 10.1002/aic.690490125.

[142] J. D. Lee, R. Susilo, and P. Englezos, “Methane–ethane and methane–propane hydrate formation and decomposition on water droplets,” *Chem. Eng. Sci.*, vol. 60, no. 15, pp. 4203–4212, Aug. 2005, doi: 10.1016/J.CES.2005.03.003.

[143] H. Ueno, H. Akiba, S. Akatsu, and R. Ohmura, “Crystal growth of clathrate hydrates formed with methane + carbon dioxide mixed gas at the gas/liquid interface and in liquid water,” *New J. Chem.*, vol. 39, no. 11, pp. 8254–8262, Oct. 2015, doi: 10.1039/C5NJ01080B.

[144] K. Saito, M. Kishimoto, R. Tanaka, and R. Ohmura, “Crystal Growth of Clathrate Hydrate at the Interface between Hydrocarbon Gas Mixture and Liquid Water,” *Cryst. Growth Des.*, vol. 11, no. 1, pp. 295–301, Jan. 2011, doi: 10.1021/cg101310z.

[145] P. Servio and P. Englezos, “Morphology study of structure H hydrate formation from water droplets,” *Cryst. Growth Des.*, vol. 3, no. 1, pp. 61–66, 2003, doi: 10.1021/cg020044e.

[146] K. Jeong *et al.*, “Hydrate nucleation and growth on water droplets acoustically-levitated in high-pressure natural gas,” *Phys. Chem. Chem. Phys.*, vol. 21, pp. 21685–21688, 2019, doi: 10.1039/C9CP04403E.

[147] I. L. Moudrakovski, G. E. McLaurin, C. I. Ratcliffe, and J. A. Ripmeester, "Methane and carbon dioxide hydrate formation in water droplets: Spatially resolved measurements from magnetic resonance microimaging," *J. Phys. Chem. B*, 2004, doi: 10.1021/jp0473220.

[148] M. Lokanathan, P. V. Acharya, A. Ouroua, S. M. Strank, R. E. Hebner, and V. Bahadur, "Review of Nanocomposite Dielectric Materials With High Thermal Conductivity," *Proc. IEEE*, pp. 1–34, 2021, doi: 10.1109/JPROC.2021.3085836.

[149] N. Maeda, "Nucleation of Gas Hydrates," in *Nucleation of Gas Hydrates*, Springer International Publishing, 2020, pp. 111–148.

[150] E. L. Cussler, Edward Lansing Cussler, *Diffusion: mass transfer in fluid systems*, 2nd ed. Cambridge university press, 2009.

[151] P. M. Rodger, T. R. Forester, and W. Smith, "Simulations of the methane hydrate/methane gas interface near hydrate forming conditions conditions," *Fluid Phase Equilib.*, vol. 116, no. 1–2, pp. 326–332, Mar. 1996, doi: 10.1016/0378-3812(95)02903-6.

[152] M. Khurana, Z. Yin, and P. Linga, "A review of clathrate hydrate nucleation," *ACS Sustain. Chem. Eng.*, vol. 5, no. 12, pp. 11176–11203, 2017, doi: 10.1021/acssuschemeng.7b03238.

[153] H. Ueno, H. Akiba, S. Akatsu, and R. Ohmura, "Crystal growth of clathrate hydrates formed with methane + carbon dioxide mixed gas at the gas/liquid interface and in liquid water," *New J. Chem.*, vol. 39, no. 11, pp. 8254–8262, Oct. 2015, doi: 10.1039/C5NJ01080B.

[154] A. Shahriari, P. V. Acharya, K. Carpenter, and V. Bahadur, "Metal-Foam-Based Ultrafast Electronucleation of Hydrates at Low Voltages," *Langmuir*, vol. 33, no. 23, pp. 5652–5656, Jun. 2017, doi: 10.1021/acs.langmuir.7b00913.

[155] M. S. Hunter and P. Fowle, "Natural and Thermally Formed Oxide Films on Aluminum," *J. Electrochem. Soc.*, vol. 103, no. 9, pp. 482–485, 1956, doi: 10.1149/1.2430389.

[156] K. Kashiwagi, T. Hattori, Y. Samejima, N. Kobayashi, and S. Nakabayashi, "Hydrogen Nanobubbles at Roughness-Regulated Surfaces: Why Does the Standard Hydrogen Electrode Need a Platinized Platinum Electrode?," *J. Phys. Chem. C*, vol. 123, no. 12, pp. 7416–7424, Mar. 2019, doi: 10.1021/acs.jpcc.8b11648.

[157] J. Kyte and R. F. Doolittle, “A simple method for displaying the hydropathic character of a protein,” *J. Mol. Biol.*, vol. 157, no. 1, pp. 105–132, May 1982, doi: 10.1016/0022-2836(82)90515-0.

[158] P. V. Acharya, A. Kar, A. Shahriari, A. Bhati, A. Mhadeshwar, and V. Bahadur, “Aluminum-Based Promotion of Nucleation of Carbon Dioxide Hydrates,” *J. Phys. Chem. Lett.*, vol. 11, no. 4, pp. 1477–1482, Feb. 2020, doi: 10.1021/ACS.JPCLETT.9B03485.

[159] T. J. Carver, M. G. B. Drew, and P. M. Rodger, “Molecular dynamics calculations of N-methylpyrrolidone in liquid water,” *Phys. Chem. Chem. Phys.*, vol. 1, no. 8, pp. 1807–1816, 1999.

[160] D. Laage, G. Stirnemann, F. Sterpone, R. Rey, and J. T. Hynes, “Reorientation and Allied Dynamics in Water and Aqueous Solutions,” *http://dx.doi.org/10.1146/annurev.physchem.012809.103503*, vol. 62, pp. 395–416, Mar. 2011, doi: 10.1146/ANNUREV.PHYSCHEM.012809.103503.

[161] A. Pertsemlidis, A. M. Saxena, A. K. Soper, T. Head-Gordon, and R. M. Glaeser, “Direct evidence for modified solvent structure within the hydration shell of a hydrophobic amino acid,” *Proc. Natl. Acad. Sci.*, vol. 93, no. 20, pp. 10769–10774, 1996.

[162] J.-H. Sa, G.-H. Kwak, B. R. Lee, D.-H. Park, K. Han, and K.-H. Lee, “Hydrophobic amino acids as a new class of kinetic inhibitors for gas hydrate formation,” *Sci. Rep.*, vol. 3, no. 1, pp. 1–7, 2013.

[163] C. B. Bavoh, B. Lal, O. Nashed, M. S. Khan, L. K. Keong, and M. A. Bustam, “COSMO-RS: An ionic liquid prescreening tool for gas hydrate mitigation,” *Chinese J. Chem. Eng.*, vol. 24, no. 11, pp. 1619–1624, Nov. 2016, doi: 10.1016/J.CJCHE.2016.07.014.

[164] P. Naeiji, M. Mottahedin, and F. Varaminian, “Separation of methane–ethane gas mixtures via gas hydrate formation,” *Sep. Purif. Technol.*, vol. 123, pp. 139–144, Feb. 2014, doi: 10.1016/J.SEPPUR.2013.12.028.

[165] J.-H. Sa, G.-H. Kwak, K. Han, D. Ahn, and K.-H. Lee, “Gas hydrate inhibition by perturbation of liquid water structure,” *Sci. Reports 2015 51*, vol. 5, no. 1, pp. 1–9, Jun. 2015, doi: 10.1038/SREP11526.

[166] S. S. Fan and T. M. Guo, “Hydrate formation of CO2-rich binary and quaternary gas mixtures in aqueous sodium chloride solutions,” *J. Chem. Eng. Data*, 1999, doi: 10.1021/je990011b.

[167] P. D. Dholabhai, N. Kalogerakis, and P. R. Bishnoi, “Equilibrium Conditions for Carbon Dioxide Hydrate Formation in Aqueous Electrolyte Solutions,” *J. Chem. Eng. Data*, vol. 38, no. 4, pp. 650–654, 1993, doi: 10.1021/je00012a045.

[168] E. D. Sloan, “A changing hydrate paradigm—from apprehension to avoidance to risk management,” *Fluid Phase Equilib.*, vol. 228–229, pp. 67–74, Feb. 2005, doi: 10.1016/J.FLUID.2004.08.009.

[169] S. M. Lundberg, G. G. Erion, and S.-I. Lee, “Consistent individualized feature attribution for tree ensembles,” *arXiv Prepr. arXiv1802.03888*, 2018.

[170] W. Zeng, A. Davoodi, and R. O. Topaloglu, “Explainable DRC Hotspot Prediction with Random Forest and SHAP Tree Explainer,” in *2020 Design, Automation & Test in Europe Conference & Exhibition (DATE)*, Mar. 2020, pp. 1151–1156, doi: 10.23919/DATE48585.2020.9116488.

[171] X. Zhao, Z. Qiu, Z. Zhang, and Y. Zhang, “Relationship between the gas hydrate suppression temperature and water activity in the presence of thermodynamic hydrate inhibitor,” *Fuel*, vol. 264, p. 116776, Mar. 2019, doi: 10.1016/j.fuel.2019.116776.

[172] J. Javanmardi, M. Moshfeghian, and R. N. Maddox, “An accurate model for prediction of gas hydrate formation conditions in mixtures of aqueous electrolyte solutions and alcohol,” *Can. J. Chem. Eng.*, vol. 79, no. 3, pp. 367–373, Jun. 2001, doi: 10.1002/cjce.5450790309.

[173] L. Breiman, “Random forests,” *Mach. Learn.*, vol. 45, no. 1, pp. 5–32, Oct. 2001, doi: 10.1023/A:1010933404324.

[174] P. Geurts, D. Ernst, and L. Wehenkel, “Extremely randomized trees,” *Mach. Learn.*, vol. 63, no. 1, pp. 3–42, Apr. 2006, doi: 10.1007/s10994-006-6226-1.

[175] T. Chen and C. Guestrin, “XGBoost: A Scalable Tree Boosting System,” in *Proceedings of the 22nd ACM SIGKDD International Conference on Knowledge Discovery and Data Mining*, Aug. 2016, pp. 785–794, doi: 10.1145/2939672.2939785.

[176] L. Breiman, “Bagging predictors,” *Mach. Learn.*, vol. 24, no. 2, pp. 123–140, 1996, doi: 10.1007/bf00058655.

[177] T. K. Ho, “The random subspace method for constructing decision forests,” *IEEE Trans. Pattern Anal. Mach. Intell.*, vol. 20, no. 8, pp. 832–844, 1998, doi: 10.1109/34.709601.

[178] N. Dholabhai, P.D., Kalogerakis and P. R. Bishnoi, “Equilibrium conditions for carbon dioxide hydrate formation in aqueous electrolyte solutions,” *J. Chem. Eng. Data*, vol. 38, no. 4, pp. 650–654, 1993.

[179] P. Englezos and Y. T. Ngan, “Incipient equilibrium data for propane hydrate formation in aqueous solutions of sodium chloride, potassium chloride and calcium chloride.,” *J. Chem. Eng. Data*, vol. 38, no. 2, pp. 250–253, 1993.

[180] P. D. Dholabhai and P. R. Bishnoi, “Hydrate equilibrium conditions in aqueous electrolyte solutions: mixtures of methane and carbon dioxide,” *J. Chem. Eng. Data*, vol. 39, no. 1, pp. 191–194, 1994.

[181] D. H. Mei, J. Liao, J. T. Yang, and T. M. Guo, “Experimental and modeling studies on the hydrate formation of a methane + nitrogen gas mixture in the presence of aqueous electrolyte solutions,” *Ind. Eng. Chem. Res.*, vol. 35, no. 11, pp. 4342–4347, 1996, doi: 10.1021/ie9601662.

[182] S. P. Kang, M. K. Chun, and H. Lee, “Phase equilibria of methane and carbon dioxide hydrates in the aqueous MgCl2 solutions,” *Fluid Phase Equilib.*, vol. 147, no. 1–2, pp. 229–238, Jun. 1998, doi: 10.1016/s0378-3812(98)00233-7.

[183] T. Maekawa, “Equilibrium conditions for gas hydrates of methane and ethane mixtures in pure water and sodium chloride solution.,” *Geochem. J.*, vol. 35, no. 1, pp. 59–66, Feb. 2001, doi: 10.2343/geochemj.35.59.

[184] M. D. Jager and E. D. Sloan, “The effect of pressure on methane hydration in pure water and sodium chloride solutions,” *Fluid Phase Equilib.*, vol. 185, no. 1–2, pp. 89–99, Jul. 2001, doi: 10.1016/S0378-3812(01)00459-9.

[185] M. Kharrat and D. Dalmazzone, “Experimental determination of stability conditions of methane hydrate in aqueous calcium chloride solutions using high pressure differential scanning calorimetry,” *J. Chem. Thermodyn.*, vol. 35, no. 9, pp. 1489–1505, Sep. 2003, doi: 10.1016/S0021-9614(03)00121-6.

[186] Z. Atik, C. Windmeier, and L. R. Oellrich, “Experimental gas hydrate dissociation pressures for pure methane in aqueous solutions of MgCl2 and CaCl2 and for a (methane + ethane) gas mixture in an aqueous solution of (NaCl + MgCl2),” *J. Chem. Eng. Data*, vol. 51, no. 5, pp. 1862–1867, Sep. 2006, doi: 10.1021/je060225a.

[187] A. H. Mohammadi, W. Afzal, and D. Richon, “Gas hydrates of methane, ethane, propane, and carbon dioxide in the presence of single NaCl, KCl, and CaCl2 aqueous solutions: Experimental measurements and predictions of dissociation

conditions," *J. Chem. Thermodyn.*, vol. 40, no. 12, pp. 1693–1697, Dec. 2008, doi: 10.1016/j.jct.2008.06.015.

[188] H. Haghighi, A. Chapoy, and B. Tohidi, "Methane and Water Phase Equilibria in the Presence of Single and Mixed Electrolyte Solutions Using the Cubic-Plus-Association Equation of State," *Oil Gas Sci. Technol. - Rev. l'IFP*, vol. 64, no. 2, pp. 141–154, Mar. 2009, doi: 10.2516/ogst:2008043.

[189] J. L. De Roo, C. J. Peters, R. N. Lichtenthaler, and G. A. M. Diepen, "Occurrence of methane hydrate in saturated and unsaturated solutions of sodium chloride and water in dependence of temperature and pressure," *AIChE J.*, vol. 29, no. 4, pp. 651–657, Jul. 1983, doi: 10.1002/aic.690290420.

[190] T. Maekawa, S. Itoh, S. Sakata, S. Igari, and N. Imai, "Pressure and temperature conditions for methane hydrate dissociation in sodium chloride solutions.," *Geochem. J.*, vol. 29, no. 5, pp. 325–329, Oct. 1995, doi: 10.2343/geochemj.29.325.

[191] P. D. Dholabhai, P. Englezos, N. Kalogerakis, and P. R. Bishnoi, "Equilibrium conditions for methane hydrate formation in aqueous mixed electrolyte solutions," *Can. J. Chem. Eng.*, vol. 69, no. 3, pp. 800–805, Jun. 1991, doi: 10.1002/cjce.5450690324.

[192] R. Nakane, E. Gima, R. Ohmura, I. Senaha, and K. Yasuda, "Phase equilibrium condition measurements in carbon dioxide hydrate forming system coexisting with sodium chloride aqueous solutions," *J. Chem. Thermodyn.*, vol. 130, pp. 192–197, Jan. 2019, doi: 10.1016/j.jct.2018.10.008.

[193] B. Tohidi, R. W. Burgass, A. Danesh, and A. C. Todd, "Hydrate Inhibition Effect of Produced Water: Part 1—Ethane and Propane Simple Gas Hydrates," Apr. 1993, doi: 10.2118/26701-MS.

[194] G. D. Holder and G. C. Grigoriou, "Hydrate dissociation pressures of (methane + ethane + water) existence of a locus of minimum pressures," *J. Chem. Thermodyn.*, vol. 12, no. 11, pp. 1093–1104, Nov. 1980, doi: 10.1016/0021-9614(80)90166-4.

[195] S. G. Paranjpe, S. L. Patil, V. A. Kamath, and S. P. Godbole, "Hydrate equilibria for binary and ternary mixtures of methane, propane, isobutane, and n-butane. Effect of salinity," *SPE Reserv. Eng. (Society Pet. Eng.*, vol. 4, no. 4, pp. 446-454 16871, Nov. 1989, doi: 10.2118/16871-pa.

[196] S. Adisasmito, R. J. Frank, and E. D. Sloan, "Hydrates of Carbon Dioxide and Methane Mixtures," *J. Chem. Eng. Data*, vol. 36, no. 1, pp. 68–71, Jan. 1991, doi:

10.1021/je00001a020.

[197] S. Adisasmito and E. D. Sloan Jr, “Hydrates of hydrocarbon gases containing carbon dioxide,” *J. Chem. Eng. Data*, vol. 37, no. 3, pp. 343–349, 1992.

[198] J. Nixdorf and L. R. Oellrich, “Experimental determination of hydrate equilibrium conditions for pure gases, binary and ternary mixtures and natural gases,” *Fluid Phase Equilib.*, vol. 139, no. 1–2, pp. 325–333, Dec. 1997, doi: 10.1016/s0378-3812(97)00141-6.

[199] H.-J. Ng and D. B. Robinson, “The role ofn-butane in hydrate formation,” *AIChE J.*, vol. 22, no. 4, pp. 656–661, Jul. 1976, doi: 10.1002/aic.690220404.

[200] G. D. Holder and J. H. Hand, “Multiple-phase equilibria in hydrates from methane, ethane, propane and water mixtures,” *AIChE J.*, vol. 28, no. 3, pp. 440–447, May 1982, doi: 10.1002/aic.690280312.

[201] J. Jhaveri and D. B. Robinson, “Hydrates in the methane-nitrogen system,” *Can. J. Chem. Eng.*, vol. 43, no. 2, pp. 75–78, Apr. 1965, doi: 10.1002/cjce.5450430207.

[202] B. J. Wu, D. B. Robinson, and H. J. Ng, “Three- and four-phase hydrate forming conditions in methane + isobutane + water,” *J. Chem. Thermodyn.*, vol. 8, no. 5, pp. 461–469, May 1976, doi: 10.1016/0021-9614(76)90067-7.

[203] W. Deaton and E. Frost, *Gas hydrates and their relation to the operation of natural-gas pipe lines*. American Gas Association, 1949.

[204] V. K. Verma, “Gas hydrates from liquid hydrocarbon-water systems,” University of Michigan, 1974.

[205] C. H. Unruh and D. L. Katz, “Gas Hydrates of Carbon Dioxide-Methane Mixtures,” *J. Pet. Technol.*, vol. 1, no. 04, pp. 83–86, Apr. 1949, doi: 10.2118/949983-g.

[206] K. Ohgaki, K. Takano, H. Sangawa, T. Matsubara, and S. Nakano, “Methane exploitation by carbon dioxide from gas hydrates. Phase equilibria for CO2-CH4 mixed hydrate system.,” *J. Chem. Eng. JAPAN*, vol. 29, no. 3, pp. 478–483, 1996, doi: 10.1252/jcej.29.478.

[207] S. S. Fan and T. M. Guo, “Hydrate formation of CO2-rich binary and quaternary gas mixtures in aqueous sodium chloride solutions,” *J. Chem. Eng. Data*, vol. 44, no. 4, pp. 829–832, Jul. 1999, doi: 10.1021/je990011b.

[208] Y. T. Seo, H. Lee, and J. H. Yoon, “Hydrate phase equilibria of the carbon dioxide, methane, and water system,” *J. Chem. Eng. Data*, vol. 46, no. 2, pp. 381–384, Mar. 2001, doi: 10.1021/je000237a.

[209] H. J. Ng, J. P. Petrunia, and D. B. Robinson, “Experimental measurement and prediction of hydrate forming conditions in the nitrogen-propane-water system,” *Fluid Phase Equilib.*, vol. 1, no. 4, pp. 283–291, Jan. 1977, doi: 10.1016/0378-3812(77)80011-3.

[210] K. S. Pitzer, “Electrolytes. From Dilute Solutions to Fused Salts,” *J. Am. Chem. Soc.*, vol. 102, no. 9, pp. 2902–2906, 1980, doi: 10.1021/ja00529a006.

[211] A. Haghtalab, A. Shojaeian, and S. H. Mazloumi, “Nonelectrolyte NRTL-NRF model to study thermodynamics of strong and weak electrolyte solutions,” *J. Chem. Thermodyn.*, vol. 43, no. 3, pp. 354–363, Mar. 2011, doi: 10.1016/j.jct.2010.10.004.

[212] S. Li, Y. Li, J. Wang, K. Ge, and L. Yang, “Prediction of Gas Hydrate Formation Conditions in the Presence of Electrolytes Using an N-NRTL-NRF Activity Coefficient Model,” *Ind. Eng. Chem. Res.*, vol. 59, no. 13, pp. 6269–6278, Apr. 2020, doi: 10.1021/acs.iecr.9b06411.

[213] K. S. Pitzer and J. M. Simonson, “Thermodynamics of multicomponent, miscible, ionic systems: Theory and equations,” *J. Phys. Chem.*, vol. 90, no. 13, pp. 3005–3009, 1986, doi: 10.1021/j100404a042.

[214] M. Margules, *About the composition of the saturated vapor mixtures*, University. .

[215] A. Pedregosa, F. Varoquaux, G. Gramfort *et al.*, “Scikit-learn: Machine Learning in {P}ython,” *J. Mach. Learn. Res.*, vol. 12, pp. 2825–2830, 2011.

[216] G. James, D. Witten, T. Hastie, and R. Tibshirani, *An introduction to statistical learning*. New York: Springer, 2013.

[217] “Project and Landfill Data by State | US EPA.” https://www.epa.gov/lmop/project-and-landfill-data-state (accessed Sep. 07, 2021).

[218] A. Tran, A. Aguirre, M. Crose, H. Durand, and P. D. Christofides, “Temperature balancing in steam methane reforming furnace via an integrated CFD/data-based optimization approach,” *Comput. Chem. Eng.*, vol. 104, pp. 185–200, Sep. 2017, doi: 10.1016/J.COMPCHEMENG.2017.04.013.

[219] J. Wang, N. Watanabe, A. Okamoto, K. Nakamura, and T. Komai, “Enhanced

hydrogen production with carbon storage by olivine alteration in CO2-rich hydrothermal environments," *J. CO2 Util.*, vol. 30, pp. 205–213, Mar. 2019, doi: 10.1016/J.JCOU.2019.02.008.

[220] H. Lee, B. Lee, M. Byun, and H. Lim, "Comparative techno-economic analysis for steam methane reforming in a sorption-enhanced membrane reactor: Simultaneous H2 production and CO2 capture," *Chem. Eng. Res. Des.*, vol. 171, pp. 383–394, 2021.

[221] A. Mohammadi and A. Jodat, "Investigation of the kinetics of TBAB + carbon dioxide semiclathrate hydrate in presence of tween 80 as a cold storage material," *J. Mol. Liq.*, vol. 293, p. 111433, Nov. 2019, doi: 10.1016/J.MOLLIQ.2019.111433.

[222] A. Bahadori, "Gas Compressors," in *Natural Gas Processing*, Elsevier, 2014, pp. 223–273.

[223] N. H. Duc, F. Chauvy, and J. M. Herri, "CO2 capture by hydrate crystallization – A potential solution for gas emission of steelmaking industry," *Energy Convers. Manag.*, vol. 48, no. 4, pp. 1313–1322, Apr. 2007, doi: 10.1016/J.ENCONMAN.2006.09.024.

[224] Z. W. Ma, P. Zhang, H. S. Bao, and S. Deng, "Review of fundamental properties of CO2hydrates and CO2capture and separation using hydration method," *Renew. Sustain. Energy Rev.*, vol. 53, pp. 1273–1302, 2016, doi: 10.1016/j.rser.2015.09.076.

[225] J. M. Douglas, *Conceptual design of chemical processes*, vol. 1110. McGraw-Hill New York, 1988.

[226] W. L. Luyben, "Estimating refrigeration costs at cryogenic temperatures," *Comput. Chem. Eng.*, vol. 103, pp. 144–150, Aug. 2017, doi: 10.1016/J.COMPCHEMENG.2017.03.013.

[227] A. Oxera, "Discount rates for low-carbon and renewable generation technologies," *Report. Oxera Consult. LLP*, vol. 747, 2011.

[228] E. D. Wikramanayake, O. Ozkan, and V. Bahadur, "Landfill gas-powered atmospheric water harvesting for oilfield operations in the United States," *Energy*, vol. 138, pp. 647–658, Nov. 2017, doi: 10.1016/J.ENERGY.2017.07.062.

[229] "Chapter 1: landfill gas energy basics," in *LFG energy project development handbook*, .

[230] “Wholesale U.S. electricity prices were generally lower and less volatile in 2020 than 2019 - Today in Energy - U.S. Energy Information Administration (EIA).” https://www.eia.gov/todayinenergy/detail.php?id=46396 (accessed Oct. 09, 2021).

[231] P. Lamers *et al.*, “Techno-economic analysis of decentralized biomass processing depots,” *Bioresour. Technol.*, vol. 194, pp. 205–213, Oct. 2015, doi: 10.1016/J.BIORTECH.2015.07.009.

[232] “Climate Change Indicators: U.S. Greenhouse Gas Emissions | US EPA.” https://www.epa.gov/climate-indicators/climate-change-indicators-us-greenhouse-gas-emissions (accessed Sep. 22, 2021).

[233] “Frequently Asked Questions (FAQs) - U.S. Energy Information Administration (EIA).” https://www.eia.gov/tools/faqs/faq.php?id=97&t=3 (accessed Oct. 11, 2021).

[234] H. Dagdougui, R. Sacile, C. Bersani, and A. Ouammi, “Chapter 2 - Hydrogen Production and Current Technologies,” H. Dagdougui, R. Sacile, C. Bersani, and A. B. T.-H. I. for E. A. Ouammi, Eds. Academic Press, 2018, pp. 7–21.

[235] “Utilities: Water & Sewer | Houston.org.” https://www.houston.org/houston-data/utilities-water-sewer (accessed Sep. 22, 2021).

[236] “Texas Profile.” https://www.eia.gov/state/print.php?sid=TX (accessed Sep. 25, 2021).

[237] W. Lin, A. Delahaye, and L. Fournaison, “Phase equilibrium and dissociation enthalpy for semi-clathrate hydrate of CO2 + TBAB,” *Fluid Phase Equilib.*, vol. 264, no. 1–2, pp. 220–227, Mar. 2008, doi: 10.1016/J.FLUID.2007.11.020.

[238] N. Ye and P. Zhang, “Equilibrium Data and Morphology of Tetra-n-butyl Ammonium Bromide Semiclathrate Hydrate with Carbon Dioxide,” *J. Chem. Eng. Data*, vol. 57, no. 5, pp. 1557–1562, May 2012, doi: 10.1021/JE3001443.

[239] P. Zhang, N. Ye, H. Zhu, and X. Xiao, “Hydrate Equilibrium Conditions of Tetra-n-butylphosphonium Bromide + Carbon Dioxide and the Crystal Morphologies,” *J. Chem. Eng. Data*, vol. 58, no. 6, pp. 1781–1786, Jun. 2013, doi: 10.1021/JE400179T.

[240] P. Linga, R. Kumar, J. D. Lee, J. Ripmeester, and P. Englezos, “A new apparatus to enhance the rate of gas hydrate formation: Application to capture of carbon dioxide,” *Int. J. Greenh. Gas Control*, vol. 4, no. 4, pp. 630–637, Jul. 2010, doi: 10.1016/j.ijggc.2009.12.014.

[241] Y. T. Luo, J. H. Zhu, S. S. Fan, and G. J. Chen, "Study on the kinetics of hydrate formation in a bubble column," *Chem. Eng. Sci.*, vol. 62, no. 4, pp. 1000–1009, Feb. 2007, doi: 10.1016/j.ces.2006.11.004.

[242] L.-G. Tang, X.-S. Li, Z.-P. Feng, Y.-L. Lin, and S.-S. Fan, "Natural Gas Hydrate Formation in an Ejector Loop Reactor: Preliminary Study," *Ind. Eng. Chem. Res.*, vol. 45, no. 23, pp. 7934–7940, Nov. 2006, doi: 10.1021/ie0609259.

[243] J. Du, H. Li, and L. Wang, "Cooperative effect of surfactant addition and gas-inducing agitation on methane hydrate formation rate," *Fuel*, vol. 230, pp. 134–137, Oct. 2018, doi: 10.1016/J.FUEL.2018.05.035.

[244] A. Eslamimanesh, F. Gharagheizi, A. H. Mohammadi, and D. Richon, "Phase Equilibrium Modeling of Structure H Clathrate Hydrates of Methane + Water 'Insoluble' Hydrocarbon Promoter Using QSPR Molecular Approach," *J. Chem. Eng. Data*, vol. 56, no. 10, pp. 3775–3793, Oct. 2011, doi: 10.1021/JE200444F.

[245] F. Gharagheizi and M. Sattari, "Prediction of Triple-Point Temperature of Pure Components Using their Chemical Structures," *Ind. Eng. Chem. Res.*, vol. 49, no. 2, pp. 929–932, Jan. 2009, doi: 10.1021/IE901029M.

[246] F. Gharagheizi, A. Eslamimanesh, A. H. Mohammadi, and D. Richon, "QSPR approach for determination of parachor of non-electrolyte organic compounds," *Chem. Eng. Sci.*, vol. 66, no. 13, pp. 2959–2967, Jul. 2011, doi: 10.1016/J.CES.2011.03.039.

[247] F. Gharagheizi and M. Sattari, "Estimation of molecular diffusivity of pure chemicals in water: a quantitative structure–property relationship study," *http://dx.doi.org.ezproxy.lib.utexas.edu/10.1080/10629360902949534*, vol. 20, no. 3–4, pp. 267–285, 2010, doi: 10.1080/10629360902949534.

[248] R. Todeschini and V. Consonni, *Molecular descriptors for chemoinformatics. 1. Alphabetical listing*. Wiley-VCH, 2009.

[249] P. Ilani-Kashkouli, S. Babaee, F. Gharagheizi, H. Hashemi, A. H. Mohammadi, and D. Ramjugernath, "An assessment test for phase equilibrium data of water soluble and insoluble clathrate hydrate formers," *Fluid Phase Equilib.*, vol. 360, pp. 68–76, Dec. 2013, doi: 10.1016/j.fluid.2013.08.016.

[250] J. H. Sa, Y. Hu, and A. K. Sum, "Assessing thermodynamic consistency of gas hydrates phase equilibrium data for inhibited systems," *Fluid Phase Equilib.*, vol. 473, pp. 294–299, Oct. 2018, doi: 10.1016/j.fluid.2018.06.012.

[251] A. Kar *et al.*, “Magnesium-Promoted Rapid Nucleation of Carbon Dioxide Hydrates,” *ACS Sustain. Chem. Eng.*, vol. 9, no. 33, pp. 11137–11146, Aug. 2021, doi: 10.1021/acssuschemeng.1c03041.

[252] T. Park and T.-H. Kwon, “Effect of Electric Field on Gas Hydrate Nucleation Kinetics: Evidence for the Enhanced Kinetics of Hydrate Nucleation by Negatively Charged Clay Surfaces,” *Environ. Sci. Technol.*, vol. 52, no. 5, pp. 3267–3274, Mar. 2018, doi: 10.1021/acs.est.7b05477.